IRON–DOPED ZINC SELENIDE: SPECTROSCOPY AND LASER DEVELOPMENT

DISSERTATION

Jonathan W. Evans, Air Force Civilian, USA

AFIT-ENP-DS-14-M-01

DEPARTMENT OF THE AIR FORCE
AIR UNIVERSITY

AIR FORCE INSTITUTE OF TECHNOLOGY

Wright-Patterson Air Force Base, Ohio

IRON–DOPED ZINC SELENIDE: SPECTROSCOPY AND LASER

DEVELOPMENT

DISSERTATION

Presented to the Faculty

Graduate School of Engineering and Management

Air Force Institute of Technology

Air University

Air Education and Training Command

in Partial Fulfillment of the Requirements for the

Degree of Doctor of Philosophy

Jonathan W. Evans, BS, MS

Air Force Civilian, USA

March 2014

AFIT-ENP-DS-14-M-01

IRON–DOPED ZINC SELENIDE: SPECTROSCOPY AND LASER DEVELOPMENT

Jonathan W. Evans, BS, MS
Air Force Civilian, USA

Approved:

//signed//

_____   _____
Nancy C. Giles, Ph.D.   Date
Committee Chair

//signed//

_____   _____
Patrick A. Berry, Ph.D.   Date
Committee Member

//signed//

_____   _____
Kenneth L. Schepler, Ph.D.   Date
Committee Member

//signed//

_____   _____
Glen P. Perram, Ph.D.   Date
Committee Member

//signed//

_____   _____
John F. Raquet, Ph.D.   Date
Committee Member

Accepted:

_____   _____
Adedeji B. Badiru, Ph.D.   Date
Dean, Graduate School of Engineering and Management

AFIT-ENP-DS-14-M-01

Abstract

We examine the quantum mechanics of optically active ions in crystals. Insight is developed which qualitatively explains the shape of the optical absorption and emission spectra of Fe^{2+} ions in II-VI materials. In addition to a discussion of the relevant theory, this work explores experimental techniques for absorption spectroscopy, laser-induced fluorescence spectroscopy, and upper-state lifetime measurements in detail. The data collected from these experiments are interpreted in the context of the theories developed herein. The theory and data are used to develop a simple model of the temperature dependence of the upper-state lifetime of Fe^{2+} ions in ZnSe.

We report the demonstration of high-power continuous wave laser oscillation from Fe^{2+} ions in zinc selenide in detail. Broadband wavelength tuning of an Fe:ZnSe laser is demonstrated using spectrally selective intracavity optics. Additionally,several resonator configurations were briefly tested with the significant result that > 1 W power was achieved near $4100\ nm$.

We report the use of pulsewidth modulation techniques to deliver short, high-peak-power pulses from an Fe:ZnSe laser. The first passively Q-switched Fe:ZnSe laser was successfully demonstrated with average power $> 600\ mW$ and with pulse widths $< 60\ ns$. Additionally, the first modelocked Fe:ZnSe laser was successfully demonstrated with average power of $\sim 200\ mW$.

Pro gloriam Dei et testimonium Christi

Acknowledgements

I would also like to thank my closest friends and family for their love and support. Special thanks to my parents for their emotional support. Most importantly, I thank my beloved wife for her unconditional support and unfailing commitment. Her support of this work has been subtle, yet selfless. She has labored with me through this long effort and her contribution to the success of this work cannot be underestimated.

Thank you,

<div align="right">Jonathan W. Evans</div>

Table of Contents

List of Figures

List of Tables

List of Abbreviations

Abbreviation   Page

I. Introduction

1.1 Motivation and Problem Statement

Many opto-electronic technologies of interest to the military, scientific, and medical communities operate in the middle infrared (mid-IR) wavelength region of the electromagnetic spectrum. Applications such as optical communication, remote chemical sensing, infrared countermeasures (IRCM), laser-illuminated imaging, emission spectroscopy, tissue ablation and others operate within the atmospheric transmission window from $3-5\ \mu m$. Despite growing demand for such technologies and expanding research interest in the $3-5\ \mu m$ waveband, there is a lack of suitable existing sources of mid-IR laser radiation. Thus, there is considerable need for development of robust solid-state mid-IR laser sources with tunable output in this waveband.

Laser architectures based on transition metals (TM) doped into II–VI crystals hosts have the potential to fill this capability gap. II–VI compounds, consisting of a group II metal and a group VI chalcogen, have excellent optical transmission in the middle and long-wave infrared (LW-IR) regions. Moreover, transition metal dopants assume a divalent ionization state when substituted for the Group II metal. The divalent state of the TM ion gives rise to a desirable energy level scheme for mid-IR lasing.

Efficient pulsed and continuous-wave (CW) lasers have been demonstrated in the $3-5\ \mu m$ waveband using iron-doped zinc selenide (Fe:ZnSe) as the laser gain medium. However, Fe:ZnSe requires cryogenic temperatures to sustain CW oscillation [1]. Prior to the current work, the state of the art in CW Fe:ZnSe lasers exhibited a maximum output power of less than $200\ mW$. Furthermore, prior to this work, all pulsed Fe:ZnSe lasers have been operated in the quasi-continuous-wave (QCW) gain-switched regime (see [2, 3, 4, 5]). Lasers operating in this regime can exhibit high values of

peak optical power, but typically have low values of average power.

Consequently, the motivation behind this work is threefold: First, to characterize the temperature-dependent optical properties of Fe^{2+} ions in ZnSe. Second, to scale the output power of a CW Fe:ZnSe laser beyond 1 W. Third, to demonstrate high-average power pulsed laser techniques such as Q-switching or modelocking.

1.2   Historical Background

Technological progress in Fe:ZnSe lasers is likely to proceed along a similar path to that taken by Cr:ZnSe lasers. The electronic configuration of neutral iron is $[Ar]\,4s^2 3d^6$. The six d-electrons are more tightly bound to the core of the iron atom than the s-electrons and the most stable electronic configuration of Fe^{2+} is $[Ar]\,4s^0 3d^6$. Thus, the spectroscopic properties of Fe:ZnSe are similar to Cr:ZnSe because d^6 electronic configuration of an Fe^{2+} ion is complimentary to the d^4 configuration of a Cr^{2+} ion. The complimentary configuration gives Fe:ZnSe a broad fluorescence band from 3500 to 5000 nm similar to the 2000 to 3000 nm band of Cr:ZnSe. Development of Fe:ZnSe technologies promises to deliver robust mid-IR laser sources similar and complimentary to those already demonstrated with Cr:ZnSe.

Mid-IR laser oscillation from Cr^{2+} ions has been demonstrated using a number of host materials such as zinc selenide [6], cadmium manganese telluride [7], and cadmium selenide [8]. In particular, chromium-doped zinc selenide (Cr:ZnSe) lasers have been shown to be very capable in the $2 - 3\ \mu m$ waveband. Specifically, Cr:ZnSe lasers have been demonstrated in gain-switched [9], actively Q-switched [10], modelocked [11, 12], and CW [8] regimes at room temperature. Both pulsed and CW platforms have been continuously tuned across the whole gain bandwidth of Cr:ZnSe using dispersive tuning elements [9, 13, 14]. Lasers using Cr:ZnSe as a gain medium have been reported with output power levels exceeding 12 W CW [15] and with av-

erage output power of up to 18.5 W in the gain-switched regime [16]. Cr:ZnSe lasers have been demonstrated in advanced configurations including, but not limited to, single-longitudinal-mode (SLM) [17], injection seeded gain switching (ISGS) [18], as well as master-oscillator power-amplifier (MOPA) architectures [19].

Despite many similarities, Fe:ZnSe and Cr:ZnSe differ in a few key ways. The energy of the first excited state (relative to the ground state) is lower for Fe:ZnSe than for Cr:ZnSe. Consequently, the spectral maximum of laser-induced fluorescence (LIF) from Cr:ZnSe occurs near 2450 nm (at room temperature) while the LIF from Fe:ZnSe peaks near 3850 nm (for $T \approx 80\ K$). As a consequence of this lower relative energy, the ratios of the energy of the upper state of the Fe^{2+} ion to the phonon energies of the ZnSe host are smaller than they are for Cr^{2+} ions in ZnSe. The reduced ratios of the upper state energy relative to the energies of the host phonons contribute to a greater degree of non-radiative quenching (NRQ) of fluorescence in Fe:ZnSe when compared to Cr:ZnSe. Cr^{2+} ions in ZnSe exhibit their maximum radiative lifetime of $\sim 8\ \mu s$ near 300 K [9]. In contrast, Fe^{2+} ions in ZnSe exhibit their maximum radiative lifetime at 77 K, where the upper state lifetime of Fe^{2+} ions in ZnSe has been reported to be 100 μs in single crystal material [20] and 60 μs in polycrystalline material [21]. As a result of NRQ, the upper state lifetime of Fe^{2+} ions in ZnSe is reduced to 370 ns at room temperature [22]. NRQ causes a reduction in the upper-state lifetime as well as a decrease in the radiative-efficiency of the laser transition. Thus, Cr:ZnSe can easily be induced to CW lasing at room temperature, but Fe:ZnSe must be cooled to exhibit efficient CW lasing.

Fe:ZnSe lasers have not yet achieved the technological maturity of Cr:ZnSe lasers. For instance, despite its relatively high radiative lifetime, Q-switched operation of an Fe:ZnSe laser had not been published prior to this work. Similarly, neither modelocked operation nor selective spectral tuning of a CW Fe:ZnSe laser had been demonstrated

3

prior to this work. To date, room-temperature CW laser oscillation of Fe^{2+} ions has not been demonstrated.

This lag in development is due, in part, to the requirement of cryogenic operation, as well as a lack of characterization tools in the $3000 - 5000 \ nm$ waveband. Furthermore, few pump lasers emit directly in the $2700 - 3700 \ nm$ absorption band of Fe:ZnSe at $77 \ K$ (see Figure 16 in Section 3.1). Those that are available have low maximum output power when compared to pump sources for Cr:ZnSe. For example, the CW thulium-fiber lasers commonly used to pump CW Cr:ZnSe lasers are commercially available with $> 100 \ W$ output power at $1908 \ nm$. On the other hand, the maximum power commercially available from CW lasers emitting within the absorption band of Fe:ZnSe is $1.5 \ W$ from the *Sheaumann MIR-PAC* Er:YAG laser with output at $2937 \ nm$.

Furthermore, fused silica optics absorb at the wavelengths used to pump Fe:ZnSe, so more expensive substrates are required to fabricate suitable optics. Thin film coatings used in the mid-IR waveband tend to absorb water, which readily absorbs radiation from these pump lasers. The absorption leads to rapid heating, which causes damage to the coated surfaces of mid-IR optics. Cameras and detectors capable of responding to mid-IR radiation are orders-of-magnitude more expensive than visible and near-IR cameras and detectors. Thus the barrier for entry into Fe:ZnSe laser research is considerable.

Despite the deleterious effects of NRQ, several researchers have demonstrated gain-switched laser oscillation from Fe:ZnSe. Adams et al. published the first demonstration of laser oscillation from single-crystal Fe:ZnSe in December 1999 [20]. The laser operated gain-switched with at $100 \ Hz$ pulse repetition frequency (PRF). They demonstrated that the output wavelength varied from $3980 \ nm$ to $4540 \ nm$ as they changed the temperature of the Fe:ZnSe crystal from $15 \ K$ to $180 \ K$. The maxi-

mum output energy per pulse was 12 μJ at 130 K. The pulse duration was 48 μs, corresponding to a peak power of 250 mW and an average power of 1.2 mW.

Akimov et al. improved on Adams' design by using Brewster-cut single crystal Fe:ZnSe at approximately 77 K [4]. They obtained a maximum output pulse energy of 130 mJ at 4040 nm. They also demonstrated direct tuning of the laser wavelength from 3770 nm to 4400 nm using an intracavity CaF_2 prism.

Kernal et al. followed in 2005 with a tunable gain-switched Fe:ZnSe laser operating at room temperature [5]. The output energy was estimated to be approximately 1 μJ. The output wavelength of the laser was tuned from 3900 nm to almost 4800 nm using a blazed grating in the Littrow configuration. Notably, this is the first appearance in the literature of laser oscillation from diffusion-doped poly-crystalline Fe:ZnSe.

In 2008, Voronov et al. published the demonstration of the first CW laser using Fe:ZnSe as the gain medium [1]. They obtained 160 mW of CW output near 4050 nm using single-crystal Fe:ZnSe at approximately $77K$. The figure was later published as 0.2 W [23].

Notably, Voronov et al. demonstrated the most energetic Fe:ZnSe laser to date. They extracted 187 mJ pulses from a laser using single-crystal Fe:ZnSe at 85 K as the gain medium [3]. Also notably, Myoung et al. demonstrated the most energetic room-temperature Fe:ZnSe laser to date. They extracted 3.6 mJ pulses from poly-crystalline Fe:ZnSe at room temperature [21]. Finally, Doroshenko et al. demonstrated the broadest tuning of a pulsed Fe:ZnSe laser to date. They achieved output from 3800 nm to 5000 nm. Table 1 shows the progression of lasers based on Fe^{2+} ions in solid-state hosts.

Table 1. A brief publishing history of Fe:ZnSe laser literature.

Year	Author	Crystal Type	Output Format	Energy/Power	Wavelength (nm)	Temperature (K)
1999	Adams [2]	SC ZnSe	GS (48 μs)	8 μJ	3980–4540	14–180
1999	Adams [20]	SC ZnSe	GS (48 μs)	12 μJ	3980–4540	19–170
2004	Akimov [4]	SC ZnSe	GS (300 μs)	130 mJ	3770–4400	77
2005	Voronov [3]	SC ZnSe	GS	187 mJ	4000–4170	85–255
2005	Kernal [5]	PC ZnSe	GS	1 μJ	3900–4800	300
2006	Akimov [24]	SC ZnSe	GS	370 μJ	3950–5050	300
2006	Gallian [25]	PC ZnSe	GS	—	4450	300
2008	Il'ichev [26]	PC ZnSe	Superluminescence	~ 1 mJ	4600–4700	300
2008	Voronov [1]	SC ZnSe	CW	160 mW	4040–4080	77
2009	Doroshenko [27]	SC ZnSe	GS	580 μJ	4100–4700	300
2010	Jelinkova [28]	SC ZnSe	GS	1.2 mJ	3900–4700	300
2010	Kozlovsky [23]	SC ZnSe	CW	0.2 W	4100	80
		SC CdSe	GS	2.1 mJ	4600–5900	300
2011	Doroshenko [29]	SC ZnSe	GS (200 ns)	1.3 mJ	3800–5000	300
		SC ZnSe	GS (200 ns)	1.2 mJ	3900–4700	300
2011	Myoung [30]	PC ZnSe	GS (20 ns)	3.6 mJ	4370	300
2011	Kozlovsky [31]	SC ZnS	GS (40 ns)	3.4 mJ	3490–4650	300

1.3 Approach

Advances in the field of photonics in general (and strategic investment by the Mid-IR Laser Sources group in particular) have brought many of the milestone laser demonstrations of Cr:ZnSe within reach for Fe:ZnSe. Research has proceeded along three simultaneous thrusts:

1. Optical spectroscopy of Fe:ZnSe.

2. Power scaling of CW Fe:ZnSe lasers.

3. Demonstration of Fe:ZnSe lasers in novel pulsed-output architectures.

1.3.1 Optical Spectroscopy

As mentioned in Section 1.2, NRQ prohibits CW lasing of Fe:ZnSe at room temperature. Thus, historically, CW Fe:ZnSe lasers have been operated at cryogenic temperatures [1], which adds undesirable complexity to the laser resonator design. Consequently, it is desirable to increase the maximum operating temperature of Fe:ZnSe lasers such that CW operation becomes possible near room temperature.

Detailed studies of the temperature-dependent behavior of CW Fe:ZnSe lasers have not been performed. Indeed, the maximum operating temperature of a CW Fe:ZnSe laser has not been determined. It is not known whether such a limit is intrinsic to the material, or if Fe:ZnSe can be engineered to increase this limit. Consequently, we have pursued low-temperature spectroscopic characterization of Fe:ZnSe to ascertain whether such engineering might be possible.

In this work, we perform spectrally-resolved measurements of the absorption, fluorescence, and upper-state lifetime of Fe:ZnSe at temperatures ranging from 5 to 300 K. The results are interpreted in the context of relevant physical theories. From this data, we develop models of the optical behavior of Fe:ZnSe at low temperatures and we identify mechanisms by which the maximum operating temperature of CW Fe^{2+} lasers might be increased.

1.3.2 CW Power Scaling

As described in Section 1.2, Voronov et al. demonstrated the first CW Fe:ZnSe laser in 2008. They pumped a single-crystal sample of Fe:ZnSe with 0.6 W from a CW Cr:CdSe laser emitting at 2970 nm. The concentration of Fe^{2+} ions in the ZnSe crystal was estimated to be 2.2×10^{18} cm^{-3}, which is orders of magnitude lower than a typical rare-earth doped laser gain medium. The low concentration of absorbers resulted in a absorption efficiency of 56%, and thus only 340 mW of pump power was absorbed. The output wavelength of the laser at maximum power was $\sim$ 4080 nm, and thus the quantum limit of extracted power for this interaction was

$$P_{limit} = \frac{2970\ nm}{4080\ nm} \cdot 340\ mW = 249\ mW. \qquad (1.3.1)$$

The absorbed power threshold of lasing was 56 mW and thus the maximum expected output would have been 207 mW. They achieved a maximum output power

of 160 mW, or about 77% of the theoretical maximum value.

In contrast, poly-crystalline ZnSe diffusion doped to an estimated concentration of 8.6×10^{18} cm^{-3} is available from the *IPG Photonics*. Such crystals have been measured to have an absorption coefficient of $\alpha = 1.6$ cm^{-1} at $\lambda = 2937$ nm. For an 8 mm sample, this correlates to roughly 72% absorption. Additionally, diode-pumped solid-state (DPSS) Er:YAG laser modules emitting at 2937 nm with 1.5 W of CW output power are now available [32]. Using beam combination techniques, two such lasers can be combined to achieve 3 W of pump power. Thus, assuming the 50 mW lasing threshold of Voronov, the theoretical maximum of output power is

$$P_{limit} = \frac{2937 \ nm}{4080 \ nm} \cdot 72\% \cdot (3 \ W - 50 \ mW) = 1.53 \ W. \qquad (1.3.2)$$

Thus, assuming no roll-off of output power, it should be possible to achieve $\sim 1.5 \ W$ of output power. This, would be nearly a factor of ten increase in the output power compared to Voronov's initial work.

1.3.3   Novel Pulse Modulation and Tuning Schemes

As described in Section 1.2, Cr:ZnSe has been used extensively as the gain medium for a variety of laser architectures. The literature detail the demonstration of lasers with a variety of pulse formats, including CW, gain-switched, Q-switched, and mode-locked lasers. Furthermore, dispersive tuning techniques have been demonstrated for pulsed and CW Cr:ZnSe lasers. As of the date of this manuscript, Q-switching and modelocking of Fe:ZnSe have not been published in the literature. Furthermore, dispersive tuning of CW Fe:ZnSe lasing has not been published either.

Pulse-modulation and wavelength-tuning techniques generally come at the cost of introducing additional losses to the laser resonator. Thus, these techniques are assisted greatly by operating with high intracavity intensities. Thus, the availability

of more pump power and improved absorption efficiency promises the realization of such techniques.

1.4 Dissertation Organization

The remainder of the dissertation document will be organized with a chapter for theoretical considerations, chapters dedicated to each thrust enumerated in Section 1.3, and a chapter to summarize the work. That is, a chapter each for:

1. Physical Theory of Fe:ZnSe

2. Spectroscopy of Fe:ZnSe

3. Continuous-Wave Fe:ZnSe Lasers

4. Pulsed Fe:ZnSe Lasers

5. Summary and Conclusions

II. Theory of Fe^{2+} Ions in ZnSe

In this chapter, we examine the quantum mechanics of optically active ions in crystals. Insight is developed which qualitatively explains the shape of the optical absorption and emission spectra of Fe^{2+} ions in II–VI materials. Several coupled effects which play a role in determining the energy level structure of the optically active electrons in these materials are considered. The complexities of the mathematical methods required to derive that structure are discussed. This discussion is included because, in the opinion of the author, those interested in laser sources based on Fe^{2+} ions in II–VI materials lack a single resource which concisely explains the origin of unfamiliar notation and nomenclature which appears in the literature.

In addition to a discussion of the relevant theory, this chapter explores experimental techniques for absorption spectroscopy, laser-induced fluorescence spectroscopy, and upper-state lifetime measurements in detail. The data collected from these experiments are interpreted in the context of the theories developed herein. The theory and data are used to develop a simple model of the temperature dependence of the upper-state lifetime of Fe^{2+} ions in ZnSe. Experimental results are compared to and contrasted with results published in the relevant literature.

2.1 The Electronic Hamiltonian for the 3d^6 Configuration

The electronic configuration of a neutral iron atom is $[Ar]\,4s^2 3d^6$. When integrated into II–VI host materials, the iron atom assumes a doubly-ionized configuration. One expects its doubly-ionized configuration to be $[Ar]\,4s^2 3d^4$. However, the six d-electrons are more tightly bound to the core of the iron atom than the s-electrons are and the most stable electronic configuration of Fe^{2+} is $[Ar]\,4s^0 3d^6$. This configuration largely determines the optical behavior of the ion.

The allowed values of energy of the optically active electrons of the Fe^{2+} ion can be found by identifying the Hamiltonian of the system and solving the Schrödinger equation. Traditionally, the Born–Oppenheimer approximation (BOA) is invoked to simplify the solution. The BOA states that the wavefunctions of electrons acted on by multiple forces can be can be treated as separable into a component due to each force if the effects of the forces on the energy of the electron are substantially different in magnitude. Thus the Hamiltonian of the electron is also considered separable and can be written as the sum of the constituent effects. Thus, the solution can be found in distinct steps treating each smaller effect as an additional small perturbation to the solution of the system when that effect is neglected. In general, each additional effect can be seen to induce an additional splitting of the energy levels and thus add features to the emission and absorption spectra of the Fe^{2+} ion.

The Hamiltonian of the Fe^{2+} ion can be written

$$\hat{H} = \hat{H}_0 + \hat{H}_{CF} + \hat{H}_{SO} + \hat{H}_{JT} \qquad (2.1.1)$$

where $\hat{H}_0$ is the *central potential* or *free-ion* Hamiltonian, $\hat{H}_{CF}$ is the static crystal field term, $\hat{H}_{SO}$ is the spin–orbit coupling term, and $\hat{H}_{JT}$ is the Jahn–Teller term. In the following sections we will address each of these effects individually and integrate them with discussion of the absorption and emission spectra of Fe:ZnSe.

2.2 Spectroscopic Term Symbols for the 3d^6 Configuration

In this section we consider just the simple case of a single electron with a Hamiltonian

$$\hat{H} = \hat{H}_0 = \hat{H}_{KE} + \hat{H}_{NA} + \hat{H}_{ee}. \qquad (2.2.1)$$

We will quickly gloss over a great deal of quantum theory and simply state that $\hat{H}_0$ includes the kinetic energy of the free particle $\hat{H}_{KE}$, a term $\hat{H}_{NA}$ to describe the attraction of the electron to the atomic nucleus, and a term $\hat{H}_{ee}$ to describe the electron-electron Coulomb repulsion. These terms combine to form a simple model of an electron bound to an atomic core. The eigenstates of the electronic Hamiltonian can be labeled by three quantum numbers n, l, and m. It can be shown that we actually require four quantum numbers to adequately describe the movement of a particle with intrinsic angular momentum (spin) within the central potential. Thus, the wavefunctions of the electron are often labeled $|nlm_lm_s\rangle$. Thus the Schrödinger equation can be written

$$\hat{H}_0 \left|nlm_lm_s\right\rangle = E_0 \left|nlm_lm_s\right\rangle. \tag{2.2.2}$$

Here, n is called the *principal quantum number* and describes which shell the electron occupies. l is called the *angular quantum number* and describes which subshell the electron occupies; l gives the magnitude of the orbital angular momentum $L^2 = \hbar^2 l\left(l+1\right)$ of the electron. m_l is called the *magnetic quantum number* and describes which orbital within a subshell the electron occupies; m_l gives the magnitude of the projection of the electron's angular momentum $L_z = m_l\hbar$ onto the arbitrarily chosen z-axis. Finally, m_s is called the *spin quantum number* and describes the projection of the spin angular momentum $S_z = m_s\hbar$ onto the z-axis. By convention $n = 1, 2, 3, \ldots$ and $l = s, p, d, f, g, h, \ldots$ where $s \rightarrow 0$, $p \rightarrow 1$, and so on.

Recall that the electronic configuration of Fe^{2+} is $3d^6$. This commonly used notation takes the form nl^w, where w is the number of electrons occupying the lth subshell. Clearly, for Fe^{2+} ions, $n = 3$ and $l = 2$. It should be noted that n and l do not play an active role in deriving the term symbols, only in describing the electron configuration. Thus, we are able to use a contracted notation $|nlm_lm_s\rangle \rightarrow |m_lm_s\rangle$.

The Pauli exclusion principle states that two electrons cannot occupy the same state and must thus have a unique set of quantum numbers. Thus, each electron in the Fe^{2+} ion must be labeled by a unique ordered pair (m_l, m_s) corresponding to orbital and spin angular momentum respectively. The allowed combinations of orbital and spin angular momentum determine the spectroscopic term symbols.

Let us note the equivalence of electrons and their vacancies and recognize that the configuration $3d^6$ is equivalent to $3d^4$. The spectroscopic term symbols are the same in both cases. The terms symbols derived here are applicable to Fe^{2+} as well as Cr^{2+}, Co^{3+}, and Mn^{3+}. Note that these term symbols label similar states in each of these ions, but that the energies of such states are not the same.

There are five d-orbitals, labeled by $m_l = -2, -1, 0, 1 - 2$, and 2. An electron may occupy each orbital in the spin-up or spin-down sense as labeled by $m_s = 1/2$ or $m_s = -1/2$ respectively. Thus, there are $\binom{10}{6}$, or 210, possible ways that six electrons can occupy the $3d$ subshell. Without enumerating each state, we simply show a few possible states in Table 2. Each state can be labeled by a total orbital momentum $M_l = \sum m_l$ and a total spin angular momentum $M_s = \sum m_s$ as shown.

Table 2. Some possible states of configuration d^6.

$m_l =$	-2	-1	0	1	2	M_l	M_s
			↑↓	↑↓	↑↓	6	0
	↑↓	↑	↑	↓	↑	-2	1
	↑↓	↑↓	↓	↓		-5	-1
	⋮	⋮	⋮	⋮	⋮	⋮	⋮

If we count the occurrences of each ordered pair (M_l, M_s) we can assemble the table of Slater determinants (see Table 3). Note that the sum of the entries in this table is 210. Thus, every possible state of the d^6 configuration is considered when assembling the table. The term symbols can be collected by finding the greatest common blocks of size $m \times n$ with all elements equal to one, which is then subtracted

Table 3. The table of Slater determinants for configuration d^6.

| | | M_s |
		-4	-2	0	2	4
M_l	6	0	0	1	0	0
	5	0	1	2	1	0
	4	0	2	5	2	0
	3	0	4	8	4	0
	2	1	6	12	6	1
	1	1	8	14	8	1
	0	1	8	16	8	1
	-1	1	8	14	8	1
	-2	1	6	12	6	1
	-3	0	4	8	4	0
	-4	0	2	5	2	0
	-5	0	1	2	1	0
	-6	0	0	1	0	0

from the table. In this case, for example, a single block of size 13×1 can be subtracted, then another of size 11×3, another of size 11×1, and so on. The height of such a block is $m = 2L + 1$ and is labeled $L = S, P, D, F, G, H, I, \ldots$ according to spectroscopic convention. Likewise, the width of such a block is $n = 2S + 1$. The corresponding term symbol is then labeled ^{2s+1}L. Thus, Table 3 can be factored into the terms ^1I, ^3H, ^3G, $2 \times (^1G)$, $2 \times (^3F)$, ^1F, ^5D, ^3D, $2 \times (^1D)$, $2 \times (^3P)$, and $2 \times (^1S)$.

Hund's rules specify the order of these states with respect to energy. The first rule states that the terms with the greatest degeneracy are the lowest in energy. Within the context of the first rule, the second rule states that terms with the greatest angular momentum are the lowest in energy. Thus the terms can be ranked in energy from highest to lowest: ^1S, ^1D, ^1F, ^1G, ^1I, ^3P, ^3D, ^3F, ^3G, ^3H, and ^5D. Thus we see that the ^5D term corresponds to the ground energy level.

We assume that $E_{^3H} - E_{^5D} \gg k_bT$ for low temperatures. Thus, the higher energy terms do not contain a significant fraction of the electron population at equilibrium. Thus, we conclude that all optical absorption is due to interactions with electrons in the ground state. Furthermore, we note that we are primarily concerned with optical

transitions in the mid-IR. Transitions from the ^3H state to the ^5D ground state would emit photons too energetic to have wavelengths in the mid-IR, so we neglect them.

If we neglect all transitions between higher energy states and the ground state, then one might wonder how we expect to see any fluorescence at all. We will show that additional terms in the Hamiltonian, specifically the crystal field term, split the ground level into multiple energy levels and we will concern ourselves with optical transitions between energy levels belonging to the ^5D term.

2.3   The Crystal Field Term

Let us consider the specific case of a transition metal ion in zinc selenide in the absence of spin–orbit coupling. Here we consider only the zincblende crystal configuration and neglect the wurtzite manifestation of ZnSe. The Hamiltonian of the Fe^{2+} ion is extended to include its crystalline environment. The effects of symmetry are developed and notation is introduced which represents crystal-field split states of Fe^{2+} ions in ZnSe.

2.3.1   The Hamiltonian of the Fe–Se System

When iron is integrated into ZnSe, iron atoms displace a small fraction of the zinc atoms. The iron and zinc cations loose two electrons and the selenium anions acquire them. Thus, an Fe^{2+} ion shares ionic bonds with its selenium neighbors. For simplicity, we consider only the interaction of the Fe^{2+} ion with these nearest neighbors within the crystal. From the zincblende structure seen in Figure 1, it is clear that an iron ion is tetrahedrally coordinated by selenium atoms. The d-electrons of the iron anion then experience a Coulombic interaction with the selenium ions.
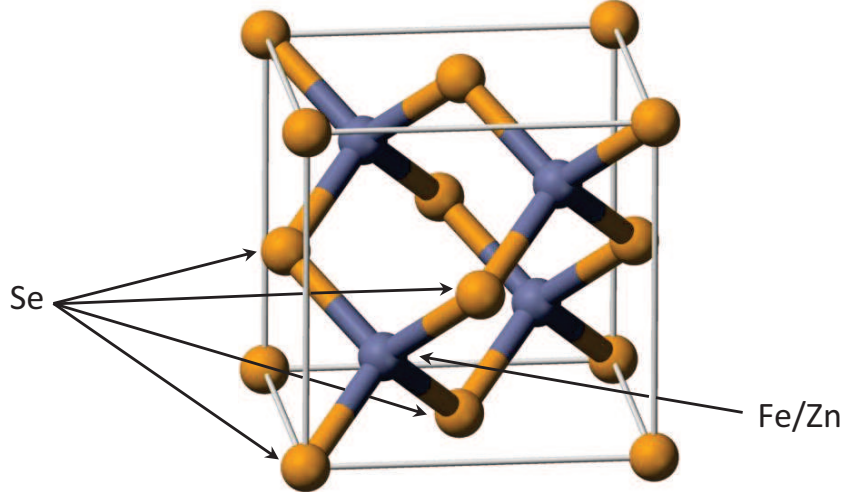
Figure 1. The zincblende unit cell and tetrahedrally coordinated Fe/Zn. Modified from Wikimedia Commons [33].

Thus, the Hamiltonian of the system becomes

$$\hat{H} = \hat{H}_0 + \hat{H}_{CF}, \tag{2.3.1}$$

where $\hat{H}_{CF}$ represents a sum over all of the Coulomb forces on a single d-electron. Now, if we suppose that the selenium ions are fixed in regular, repeated, nonmoving positions, we see that Hamiltonian of the system would not be changed if we exchanged the location of two (or more) of the selenium ions. In the following section, we derive the spectroscopic term symbols associated with the crystal field splitting of the ^5D energy term by detailed consideration of group operations which exchange the positions of several selenium ions, but which leave the Hamiltonian unchanged.

2.3.2 The Symmetry of Point Groups

Consider the tetrahedral configuration shown in Figure 2(a). Note that the cube is just for reference, the ions form the four vertices of a tetrahedron. Note also that there are five classes of transformations that, if we consider the ions to be

(a) The canonical configuration.

(b) E - The identity transformation.

(c) $8C_3$ - Corner-centered rotation.

(d) $3C_2$ - Face-centered rotation.

(e) $6S_4$ - Improper rotation.

(f) $6\sigma_d$ - Diagonal plane reflection.
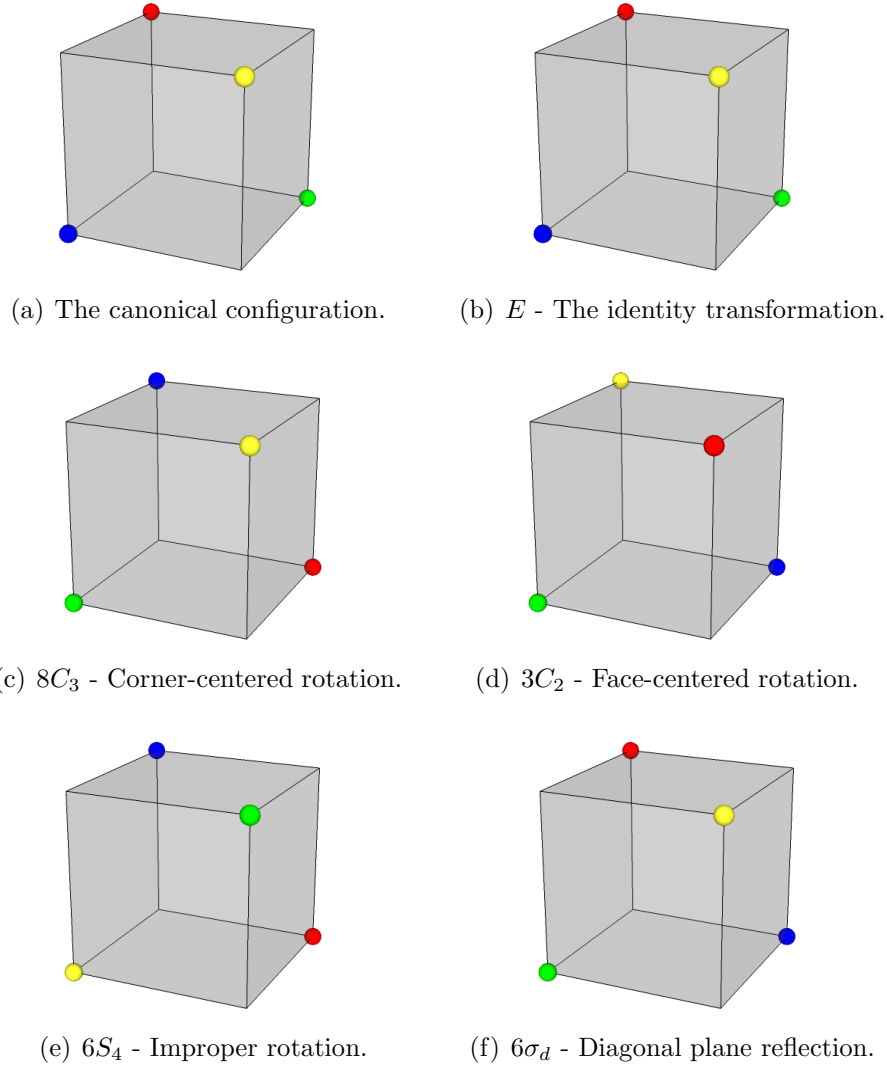
Figure 2. The various eigen-transformations of a tetrahedral point group.

indistinguishable, will leave the figure to appear unchanged (see Figure 2) [34]. The first class E contains only the identity transformation $\hat{E}$ which leaves each ion in its original position. The second class $8C_3$ is the set of eight rotations about the vertices of the cube. The axis of rotation is drawn from one vertex of the cube to the opposite vertex and a rotation of $120°$ permutes the position of three ions. The permutation is unique through all eight vertices of the cube.[1] The third class $3C_2$

---

[1]Point group transformations correspond to operators $\hat{g}$ which belong to classes $°c_g g$, where $°c_g$ is the number of unique transformations in that class. $\hat{g}$ is labeled $\hat{E}$ for the identity transformation,

17

is the set of three rotations of 180° about the face-centered axes of the cube which uniquely permute the positions of two pairs of ions simultaneously. The fourth class $6S_4$ is the set of six *improper* rotations. This class of transformation is equivalent to the subsequent application of a rotation of 90° about the face-centered axis of the cube and a reflection in the plane orthogonal to the axis of rotation. The fifth class $6\sigma_d$ is the set of six diagonal reflections which uniquely permute the position of two ions on the same face. Together, these five classes of transformation form the T_d point group, which contains every possible permutation of the positions of the ions in the tetrahedral configuration.

Now, since the ions are indistinguishable, the permutation of their positions does not change the Hamiltonian. Thus, the Hamiltonian commutes with all the group operators of the T_d point group. Thus, we can construct an equivalent eigenbasis of position whose kets are labeled by the group operators. Here we skip over the some physical and mathematical justifications of this approach and move directly to representing these transformations as matrices.

2.3.3 Representation Theory

Table 4 shows the group multiplication table of the T_d point group. This table concisely shows the equivalence of every combination of two transformations within the group. For example, the subsequent application of a face-centered rotation $\hat{C}_{2,n}$ of 180° and a reflection $\hat{\sigma}_{d,m}$ about a diagonal plane of the cube is equivalent to some other diagonal reflection $(\hat{\sigma}_{d,1}\hat{C}_{2,1} \equiv \hat{\sigma}_{d,2})$ or an improper rotation $(\hat{\sigma}_{d,3}\hat{C}_{2,1} \equiv \hat{S}_{4,3})$.

We can represent the ith group operator $\hat{g}_i$ as a matrix $\mathcal{D}\left(\hat{g}_i\right)$ with elements $\delta_{\hat{g}_i T_d(r,c)}$

$\hat{C}_n$ for pure rotations (n is the angle $\theta = 360°/n$ of the rotation), $\hat{\sigma}_h$ for *horizontal* reflections (for which the reflection plane is perpendicular to a given reference axis), $\hat{\sigma}_v$ for *vertical* plane reflections (for which the reflection plane contains the reference axis), and $\hat{\sigma}_d$ for *diagonal* plane reflections (for which the reflection plane contains the reference axis and bisects the angle between two $\hat{C}_2$ axes perpendicular to the given reference axis), and $\hat{S}$ for *improper* rotations which are the unique combinations of $\hat{C}_4$ and $\hat{\sigma}_h$.

Table 4. The group multiplication table of the tetrahedral point group $\mathbf{T_d}$. Note that the order of operations is $\hat{g}_{\text{row}}$ first and then $\hat{g}_{\text{column}}$ such that $(\hat{g}_{\text{column}}\hat{g}_{\text{row}} \equiv \hat{g}_{\text{entry}})$

	$\hat{E}$	$\hat{C}_{3,1}$	$\hat{C}_{3,2}$	$\hat{C}_{3,3}$	$\hat{C}_{3,4}$	$\hat{C}_{3,5}$	$\hat{C}_{3,6}$	$\hat{C}_{3,7}$	$\hat{C}_{3,8}$	$\hat{C}_{2,1}$	$\hat{C}_{2,2}$	$\hat{C}_{2,3}$	$\hat{S}_{4,1}$	$\hat{S}_{4,2}$	$\hat{S}_{4,3}$	$\hat{S}_{4,4}$	$\hat{S}_{4,5}$	$\hat{S}_{4,6}$	$\hat{\sigma}_{d,1}$	$\hat{\sigma}_{d,2}$	$\hat{\sigma}_{d,3}$	$\hat{\sigma}_{d,4}$	$\hat{\sigma}_{d,5}$	$\hat{\sigma}_{d,6}$
$\hat{E}$	E	$C_{3,1}$	$C_{3,2}$	$C_{3,3}$	$C_{3,4}$	$C_{3,5}$	$C_{3,6}$	$C_{3,7}$	$C_{3,8}$	$C_{2,1}$	$C_{2,2}$	$C_{2,3}$	$S_{4,1}$	$S_{4,2}$	$S_{4,3}$	$S_{4,4}$	$S_{4,5}$	$S_{4,6}$	$\sigma_{d,1}$	$\sigma_{d,2}$	$\sigma_{d,3}$	$\sigma_{d,4}$	$\sigma_{d,5}$	$\sigma_{d,6}$
$\hat{C}_{3,1}$	$C_{3,1}$	$C_{3,7}$	$C_{2,3}$	$C_{3,2}$	$C_{2,1}$	$C_{2,2}$	$C_{3,5}$	E	$C_{3,4}$	$C_{3,8}$	$C_{3,6}$	$C_{3,3}$	$S_{4,4}$	$\sigma_{d,3}$	$S_{4,6}$	$\sigma_{d,5}$	$S_{4,2}$	$\sigma_{d,2}$	$\sigma_{d,4}$	$S_{4,3}$	$S_{4,5}$	$\sigma_{d,6}$	$S_{4,1}$	$\sigma_{d,1}$
$\hat{C}_{3,2}$	$C_{3,2}$	$C_{2,1}$	$C_{3,8}$	$C_{2,2}$	$C_{3,3}$	$C_{2,3}$	$C_{3,1}$	$C_{3,6}$	E	$C_{3,5}$	$C_{3,4}$	$C_{3,7}$	$S_{4,6}$	$\sigma_{d,1}$	$S_{4,2}$	$\sigma_{d,3}$	$\sigma_{d,5}$	$S_{4,1}$	$\sigma_{d,2}$	$\sigma_{d,4}$	$S_{4,3}$	$\sigma_{d,6}$	$S_{4,4}$	$S_{4,5}$
$\hat{C}_{3,3}$	$C_{3,3}$	$C_{3,4}$	$C_{2,1}$	$C_{3,5}$	$C_{2,3}$	E	$C_{3,2}$	$C_{2,2}$	$C_{3,7}$	$C_{3,6}$	$C_{3,8}$	$C_{3,1}$	$S_{4,3}$	$\sigma_{d,4}$	$\sigma_{d,6}$	$S_{4,5}$	$\sigma_{d,2}$	$S_{4,2}$	$\sigma_{d,3}$	$S_{4,4}$	$\sigma_{d,5}$	$S_{4,6}$	$\sigma_{d,1}$	$S_{4,1}$
$\hat{C}_{3,4}$	$C_{3,4}$	$C_{2,2}$	$C_{3,5}$	$C_{2,1}$	$C_{3,6}$	$C_{3,8}$	E	$C_{3,3}$	$C_{2,3}$	$C_{3,7}$	$C_{3,2}$	$C_{3,5}$	$\sigma_{d,6}$	$S_{4,4}$	$\sigma_{d,4}$	$S_{4,6}$	$\sigma_{d,2}$	$S_{4,4}$	$\sigma_{d,5}$	$S_{4,5}$	$\sigma_{d,3}$	$S_{4,1}$	$\sigma_{d,1}$	$S_{4,2}$
$\hat{C}_{3,5}$	$C_{3,5}$	$C_{2,3}$	$C_{3,6}$	E	$C_{3,1}$	$C_{3,3}$	$C_{2,1}$	$C_{3,8}$	$C_{2,2}$	$C_{3,2}$	$C_{3,7}$	$C_{3,4}$	$\sigma_{d,6}$	$S_{4,6}$	$S_{4,1}$	$\sigma_{d,2}$	$S_{4,4}$	$\sigma_{d,4}$	$\sigma_{d,5}$	$S_{4,5}$	$\sigma_{d,1}$	$S_{4,2}$	$\sigma_{d,3}$	$S_{4,3}$
$\hat{C}_{3,6}$	$C_{3,6}$	$C_{3,2}$	$C_{2,2}$	$C_{3,7}$	E	$C_{2,3}$	$C_{3,4}$	$C_{2,1}$	$C_{3,5}$	$C_{3,3}$	$C_{3,1}$	$C_{3,8}$	$\sigma_{d,4}$	$S_{4,4}$	$\sigma_{d,5}$	$S_{4,6}$	$S_{4,1}$	$\sigma_{d,1}$	$\sigma_{d,3}$	$S_{4,2}$	$\sigma_{d,6}$	$S_{4,5}$	$\sigma_{d,2}$	$S_{4,3}$
$\hat{C}_{3,7}$	$C_{3,7}$	E	$C_{3,3}$	$C_{2,3}$	$C_{3,8}$	$C_{3,6}$	$C_{2,2}$	$C_{3,1}$	$C_{2,1}$	$C_{3,4}$	$C_{3,5}$	$C_{3,2}$	$\sigma_{d,5}$	$S_{4,5}$	$\sigma_{d,2}$	$S_{4,1}$	$\sigma_{d,3}$	$S_{4,3}$	$\sigma_{d,6}$	$S_{4,6}$	$\sigma_{d,4}$	$S_{4,2}$	$\sigma_{d,1}$	$S_{4,4}$
$\hat{C}_{3,8}$	$C_{3,8}$	$C_{3,5}$	E	$C_{3,4}$	$C_{2,2}$	$C_{2,1}$	$C_{3,7}$	$C_{2,3}$	$C_{3,2}$	$C_{3,1}$	$C_{3,3}$	$C_{3,6}$	$\sigma_{d,3}$	$S_{4,4}$	$S_{4,5}$	$\sigma_{d,6}$	$\sigma_{d,1}$	$S_{4,1}$	$\sigma_{d,4}$	$S_{4,6}$	$\sigma_{d,5}$	$\sigma_{d,2}$	$S_{4,3}$	$S_{4,2}$
$\hat{C}_{2,1}$	$C_{2,1}$	$C_{3,6}$	$C_{3,7}$	$C_{3,8}$	$C_{3,5}$	$C_{3,4}$	$C_{3,1}$	$C_{3,2}$	$C_{3,3}$	E	$C_{2,3}$	$C_{2,2}$	$S_{4,2}$	$S_{4,1}$	$\sigma_{d,1}$	$\sigma_{d,2}$	$\sigma_{d,3}$	$\sigma_{d,4}$	$S_{4,3}$	$S_{4,4}$	$\sigma_{d,5}$	$\sigma_{d,6}$	$S_{4,5}$	$S_{4,6}$
$\hat{C}_{2,2}$	$C_{2,2}$	$C_{3,3}$	$C_{3,5}$	$C_{3,1}$	$C_{3,7}$	$C_{3,2}$	$C_{3,8}$	$C_{3,4}$	$C_{3,6}$	$C_{2,3}$	E	$C_{2,1}$	$\sigma_{d,1}$	$\sigma_{d,2}$	$S_{4,4}$	$S_{4,3}$	$S_{4,5}$	$\sigma_{d,6}$	$S_{4,1}$	$S_{4,2}$	$\sigma_{d,4}$	$\sigma_{d,3}$	$S_{4,5}$	$S_{4,6}$
$\hat{C}_{2,3}$	$C_{2,3}$	$C_{3,8}$	$C_{3,4}$	$C_{3,6}$	$C_{3,2}$	$C_{3,7}$	$C_{3,3}$	$C_{3,5}$	$C_{3,1}$	$C_{2,2}$	$C_{2,1}$	E	$\sigma_{d,4}$	$\sigma_{d,3}$	$S_{4,6}$	$S_{4,5}$	$S_{4,2}$	$S_{4,1}$	$\sigma_{d,5}$	$\sigma_{d,6}$	$S_{4,3}$	$S_{4,4}$	$\sigma_{d,1}$	$\sigma_{d,2}$
$\hat{S}_{4,1}$	$S_{4,1}$	$S_{4,6}$	$S_{4,3}$	$S_{4,5}$	$S_{4,4}$	$\sigma_{d,4}$	$\sigma_{d,5}$	$\sigma_{d,3}$	$\sigma_{d,6}$	$S_{4,2}$	$\sigma_{d,2}$	$\sigma_{d,1}$	$C_{2,1}$	E	$C_{3,7}$	$C_{3,5}$	$C_{3,8}$	$C_{3,6}$	$C_{2,2}$	$C_{2,3}$	$C_{3,2}$	$C_{3,4}$	$C_{3,1}$	$C_{3,3}$
$\hat{S}_{4,2}$	$S_{4,2}$	$\sigma_{d,5}$	$\sigma_{d,3}$	$\sigma_{d,6}$	$S_{4,4}$	$\sigma_{d,1}$	$\sigma_{d,4}$	$\sigma_{d,2}$	$S_{4,1}$	$S_{4,5}$	$C_{2,2}$	$C_{2,3}$	$C_{3,5}$	$C_{3,7}$	$C_{3,1}$	E	$C_{3,2}$	$C_{3,4}$	$C_{3,3}$	$C_{3,6}$	$C_{2,1}$	$C_{3,8}$	$C_{3,6}$	$C_{3,2}$
$\hat{S}_{4,3}$	$S_{4,3}$	$S_{4,2}$	$\sigma_{d,6}$	$\sigma_{d,2}$	$S_{4,5}$	$S_{4,6}$	$\sigma_{d,1}$	$\sigma_{d,5}$	$S_{4,1}$	$\sigma_{d,4}$	$S_{4,4}$	$\sigma_{d,3}$	$C_{3,6}$	$C_{3,3}$	$C_{2,2}$	E	$C_{3,7}$	$C_{3,2}$	$C_{3,8}$	$C_{3,1}$	$C_{2,1}$	$C_{2,3}$	$C_{3,4}$	$C_{3,5}$
$\hat{S}_{4,4}$	$S_{4,4}$	$\sigma_{d,2}$	$S_{4,6}$	$S_{4,2}$	$\sigma_{d,5}$	$\sigma_{d,6}$	$S_{4,1}$	$S_{4,5}$	$\sigma_{d,1}$	$\sigma_{d,3}$	$S_{4,3}$	$\sigma_{d,4}$	$C_{3,8}$	$C_{3,1}$	E	$C_{2,2}$	$C_{3,4}$	$C_{3,5}$	$C_{3,6}$	$C_{3,3}$	$C_{2,3}$	$C_{2,1}$	$C_{3,7}$	$C_{3,2}$
$\hat{S}_{4,5}$	$S_{4,5}$	$S_{4,4}$	$S_{4,2}$	$\sigma_{d,4}$	$\sigma_{d,1}$	$S_{4,3}$	$\sigma_{d,2}$	$\sigma_{d,3}$	$\sigma_{d,6}$	$S_{4,6}$	$C_{3,5}$	$C_{3,2}$	$C_{3,6}$	$C_{3,1}$	E	$C_{2,3}$	$C_{3,5}$	$C_{3,1}$	$C_{3,6}$	$C_{2,2}$	$C_{2,1}$	$C_{3,7}$	$C_{3,3}$	$C_{3,4}$
$\hat{S}_{4,6}$	$S_{4,6}$	$\sigma_{d,3}$	$\sigma_{d,1}$	$S_{4,3}$	$S_{4,2}$	$\sigma_{d,2}$	$\sigma_{d,4}$	$S_{4,1}$	$S_{4,4}$	$\sigma_{d,6}$	$\sigma_{d,5}$	$S_{4,5}$	$C_{3,5}$	$C_{3,2}$	$C_{3,6}$	$C_{3,1}$	E	$C_{2,3}$	$C_{3,7}$	$C_{3,8}$	$C_{3,3}$	$C_{2,1}$	$C_{3,4}$	$C_{2,2}$
$\hat{\sigma}_{d,1}$	$\sigma_{d,1}$	$\sigma_{d,6}$	$S_{4,4}$	$S_{4,4}$	$\sigma_{d,5}$	$S_{4,3}$	$\sigma_{d,2}$	$S_{4,5}$	$\sigma_{d,4}$	$S_{4,1}$	$S_{4,4}$	$S_{4,1}$	$C_{2,2}$	$C_{2,3}$	$C_{3,4}$	$C_{3,3}$	$C_{3,5}$	$C_{3,6}$	$C_{3,8}$	E	$C_{2,1}$	$C_{3,2}$	$C_{3,3}$	$C_{3,1}$
$\hat{\sigma}_{d,2}$	$\sigma_{d,2}$	$S_{4,5}$	$\sigma_{d,4}$	$S_{4,6}$	$\sigma_{d,3}$	$S_{4,3}$	$\sigma_{d,6}$	$S_{4,4}$	$\sigma_{d,5}$	$S_{4,1}$	$S_{4,2}$	$C_{2,2}$	$C_{2,3}$	$C_{3,5}$	$C_{3,7}$	$C_{3,1}$	$C_{3,3}$	E	$C_{3,4}$	$C_{3,2}$	$C_{3,8}$	$C_{2,1}$	$C_{3,5}$	$C_{3,6}$
$\hat{\sigma}_{d,3}$	$\sigma_{d,3}$	$S_{4,1}$	$S_{4,5}$	$\sigma_{d,1}$	$\sigma_{d,6}$	$\sigma_{d,4}$	$S_{4,6}$	$\sigma_{d,2}$	$\sigma_{d,3}$	$S_{4,4}$	$S_{4,3}$	$C_{3,1}$	$C_{3,8}$	$C_{2,3}$	$C_{3,7}$	$C_{3,3}$	$C_{3,6}$	$C_{2,2}$	E	$C_{3,4}$	$C_{3,2}$	$C_{3,5}$	$C_{3,4}$	$C_{2,3}$
$\hat{\sigma}_{d,4}$	$\sigma_{d,4}$	$\sigma_{d,1}$	$\sigma_{d,5}$	$S_{4,1}$	$S_{4,6}$	$S_{4,5}$	$\sigma_{d,2}$	$\sigma_{d,6}$	$\sigma_{d,2}$	$S_{4,3}$	$\sigma_{d,3}$	$S_{4,4}$	$C_{3,3}$	$C_{3,6}$	$C_{2,1}$	$C_{3,8}$	$C_{2,2}$	E	$C_{3,2}$	$C_{3,7}$	$C_{3,3}$	$C_{3,6}$	$C_{3,2}$	$C_{3,7}$
$\hat{\sigma}_{d,5}$	$\sigma_{d,5}$	$S_{4,3}$	$\sigma_{d,2}$	$\sigma_{d,3}$	$S_{4,1}$	$\sigma_{d,1}$	$S_{4,4}$	$S_{4,2}$	$\sigma_{d,4}$	$S_{4,5}$	$S_{4,6}$	$\sigma_{d,6}$	$C_{3,4}$	$C_{3,7}$	$C_{3,1}$	$C_{3,6}$	$C_{2,1}$	$C_{2,2}$	$C_{3,5}$	$C_{3,2}$	$C_{3,3}$	$C_{3,8}$	E	$C_{2,3}$
$\hat{\sigma}_{d,6}$	$\sigma_{d,6}$	$\sigma_{d,4}$	$S_{4,1}$	$S_{4,4}$	$\sigma_{d,2}$	$S_{4,2}$	$\sigma_{d,3}$	$\sigma_{d,1}$	$S_{4,3}$	$S_{4,6}$	$S_{4,5}$	$\sigma_{d,5}$	$C_{2,2}$	$C_{3,5}$	$C_{3,8}$	$C_{3,3}$	$C_{2,2}$	$C_{2,1}$	$C_{3,7}$	$C_{3,4}$	$C_{3,6}$	$C_{3,1}$	$C_{2,3}$	E

and basis vectors $|E\rangle$, $|C_{3,1}\rangle$, ..., $|\sigma_{d,6}\rangle$. The set of these matrices is called the *regular representation* Γ^g of each of the group. Recall that the group operators commute with the crystal-field Hamiltonian. Thus, the matrices of the regular representation will commute with a matrix representing the Hamiltonian in the same basis. Thus, we seek a unitary matrix transformation P such that $P^{\mathsf{T}}\mathcal{D}(g)P$ is a diagonal matrix. The columns of P would then be eigenvectors of the Hamiltonian and the eigenvalues (the allowed energies of the electronic states) could be easily tabulated from the matrix representation of the Hamiltonian. However, we quickly realize from Table 4 that $\hat{g}_n\hat{g}_m \not\equiv \hat{g}_m\hat{g}_n$ and so *no transformation exists which can simultaneously diagonalize all twenty-four matrices!*

There does exist, however, a transformation which block diagonalizes all twenty-four matrices into the same maximally-compact form. The set of these matrices is called the *irreducible representation* of the group. The irreducible representation α^g of a group operator $\hat{g}$ will always contain the same number of distinct submatrices as there are classes in the symmetry group [35]. In the case of T_d, each irreducible matrix contains five distinct blocks because there are five classes of transformation which permute the points of the tetrahedral configuration as seen in Figure 2. The

blocks within each matrix are labeled A_1, A_2, E, T_1, and T_2. The label A denotes 1×1 submatrices, E is used to denote a 2×2 submatrix (which is twice repeated), and T is used to denote 3×3 submatrices (which are repeated three times).

We see then that such a transformation represents a change in basis from the basis vectors $|E\rangle$, $|C_{3,1}\rangle$, ..., $|\sigma_{d,6}\rangle$ of the regular representation to the new set of basis vectors $|A_1\rangle$, $|A_2\rangle$, $|^{(1)}E_{11}\rangle$, $|^{(1)}E_{21}\rangle$, ..., $|^{(3)}T_{2,33}\rangle$ of the irreducible representation. It is not necessary to present the twenty-four 24×24 matrices of the regular representation or the twenty-four 24×24 matrices of the irreducible representation. It is also unnecessary to present the unitary matrix which transforms between these representations because the group character table of T_d (Table 5) contains all the information about the transformation that is needed to convert between representations. The derivation of this table is not presented here, but is discussed in Harter [35] and Tsukerblat [36]. The entries of this table are the characters $\chi_g^\alpha = \text{Trace}\left(\mathcal{D}^\alpha\left(g\right)\right)$ of a given class g of transformation in the irreducible representation α. This table will be used to determine the types of wavefunctions associated with the crystal field splitting of the ^5D ground level of the Fe^{2+} ion in a tetrahedrally coordinated environment.

Table 5. The character table of the $\mathbf{T_d}$ point group.

T_d	E	$8C_3$	$3C_2$	$6S_4$	$6\sigma_d$
A_1	1	1	1	1	1
A_2	1	1	1	−1	−1
E	2	−1	2	0	0
T_1	3	0	−1	1	−1
T_2	3	0	−1	−1	1

Now, since A_1, A_2, E, T_1, and T_2 are indeed diagonal elements of the irreducible representation of the T_d point group, and because the system Hamiltonian is unchanged by the operations belonging to the group, we see that these symbols are useful as labels for the eigenstates of the crystal-field Hamiltonian. It is tempting

to jump from the observation that there are five such labels to the conclusion that the crystal field will split the ground level of the Fe^{2+} ion into five non-degenerate sublevels. This conclusion is especially tempting in light of the observation that the ground states belong to a D orbital, which are well known to have five suborbitals. However, the existence of five unique submatrices in the irreducible matrix representation of the group operators of T_d does not automatically imply the existence of five corresponding sublevels or that such sublevels would be non-degenerate. We will show in the following sections that the crystal field splits the ground level into two non-degenerate sublevels by considering the role of coupled angular momenta within the Fe–Se system.

2.3.4 Orbital Angular Momentum

We attempt now to show that the total orbital angular momentum of the system also plays a role in determining the energy level splitting of the ^5D ground level of the Fe^{2+} ion. We have shown that T_d contains several sets of rotations which leave the Hamiltonian of the system unchanged. Now consider that, in the free ion case, a rotation of the ion through *any* angle about some *arbitrary* axis leaves the Hamiltonian unchanged. Transformations of this type exhibit continuous symmetry (as opposed to the discrete symmetry of the T_d group). Objects which exhibit this kind of symmetry belong to the O_3 symmetry group.

Clearly, the regular representation of the O_3 symmetry group is an infinitely large set of matrices. The discrete angular displacements associated with operations belonging to T_d symmetry group provide a way to sample the matrix representation of O_3 in a meaningful way and derive a helpful relationship between the two symmetry groups. Recall that angular momentum is the generator of rotation, so the operator for rotation through some angle θ about some axis is $\exp{(il\theta/\hbar)}$. Recall also that

$l |l, m_l\rangle = m_l \hbar |l, m_l\rangle$, so $\exp(il\theta/\hbar) \rightarrow \exp(im_l\theta)$. Now, m_l takes on values from $-l$ to l in integer steps, so the matrix representation $\mathcal{D}^l$ of this rotation is written

$$\mathcal{D}^l(\theta) \rightarrow \begin{bmatrix} e^{-il\theta} & 0 & 0 & \dots & 0 \\ 0 & e^{-i(l-1)\theta} & 0 & \dots & 0 \\ \vdots & \vdots & \vdots & \ddots & \vdots \\ 0 & 0 & 0 & \dots & e^{il\theta} \end{bmatrix}. \tag{2.3.2}$$

The character $\chi^l(\theta)$ of the transformation is simply the trace of this matrix, which simplifies to Harter's Equation 5.6.4:

$$\chi^l(\theta) = \text{Trace}\left(\mathcal{D}^l(\theta)\right) = \frac{\sin\left(\left(l + \frac{1}{2}\right)\theta\right)}{\sin\theta/2}. \tag{2.3.3}$$

From this equation, we can generate Table 6, the traces of $\mathcal{D}^l(\theta)$.

Table 6. The trace table of the T$_d$ point group.

$^\circ c_g g$	$1E$	$8C_3$	$3C_2$	$6S_4$	$8\sigma_d$
θ	$0°$	$120°$	$180°$	$90°$	$180°$
$\chi^0(\theta)$	1	1	1	1	1
$\chi^1(\theta)$	2	0	-1	1	-1
$\chi^2(\theta)$	3	-1	1	-1	1
$\chi^3(\theta)$	7	1	-1	-1	-1
$\vdots$	$\vdots$	$\vdots$	$\vdots$	$\vdots$	$\vdots$

Without proof, the frequencies f^α of an irreducible representation $\mathcal{D}^\alpha$ of T_d in a given irreducible representation $\mathcal{D}^l$ of O_3 can be found from Harter's Equation 5.6.1

$$f^\alpha = \frac{1}{G^\circ} \sum_{\text{classes } c_g} \chi_g^{\alpha \star \circ} c_g \text{Trace}\left(\mathcal{D}^l(\theta)\right), \tag{2.3.4}$$

where l corresponds to the angular quantum number of an electron of the free ion, G° is the number of operators in the symmetry group (for T_d, $G^\circ = 24$), χ_g^α is the

22

entry of the character table of T_d (Table 5) indexed by α and g,[2] and $^\circ c_g$ is the order of the class of the transformation. We can use Equation 2.3.4 combined with Table 5 and Table 6 to generate Table 7, the correlation table of T_d.

Table 7. The correlation table of the $\mathbf{T_d}$ point group.

	f^{A_1}	f^{A_2}	f^E	f^{T_1}	f^{T_2}
$l = 0$	1	0	0	0	0
1	0	0	0	1	0
2	0	0	1	0	1
3	0	1	0	0	1
$\vdots$	$\vdots$	$\vdots$	$\vdots$	$\vdots$	$\vdots$

Now we make a final logical leap. We have proceeded to this point by assigning to certain allowed states of the d^6 electron configuration the quantum numbers L and S. This approach implicitly ascribes to a state with total orbital angular momentum L and total spin S the properties of a single electron with orbital angular momentum l and spin s. Thus we treat the ensemble of electrons as a single quasi-particle. Thus from Table 7, we see that, under the influence of the crystal field, the energy-degenerate state manifold corresponding to $L = 2$ will split into two manifolds. Specifically, the ^5D term splits into the ^5E and $^5T_2$ terms with distinct energies. Note that the superscript indicates that each of the crystal fields terms is also an $S = 2$ term.

Physically, the E and T_2 classes of wavefunctions can be distinguished from each other in the manner shown in Figure 3. Note that the electron clouds of E states point to the center of the faces of the cubic cell while the electron clouds of T states point to its edges. This difference is the fundamental reason that the E states and T_2 states of the Fe^{2+} ion are not energy degenerate in a ZnSe crystal.

Now, the crystal field basis is not the only basis we can use to describe these

---

[2]Note that α labels the classes of transformation of the T_d point group and g corresponds to a specific value of θ which labels the classes of transformation of the O_h group.

T_2

(a) $\phi_{t_2\xi}$ (b) $\phi_{t_2\zeta}$ (c) $\phi_{t_2\eta}$

E

(d) ϕ_{eu} (e) ϕ_{ev}
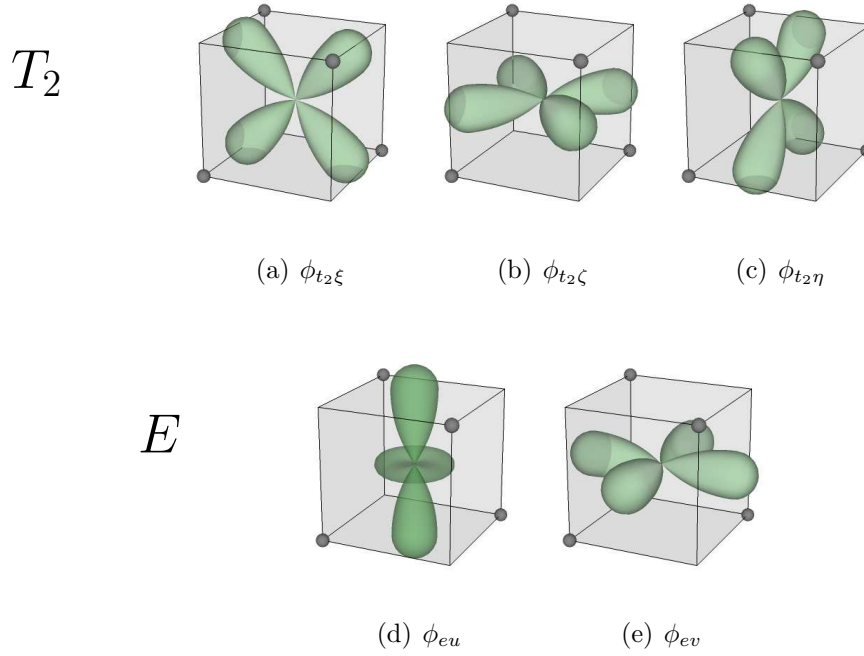
Figure 3. Wavefunctions for the L = 2 states of the d^6 configuration in a tetrahedrally coordinated environment. The origin of the state labels is discussed in Subsection 2.3.5.

states. We now manipulate the hydrogenic wave functions to calculate the magnitude of the crystal field splitting. If we consider the behavior of an $L = 2$ quasi-particle to be well described by the wavefunction of a single $l = 2$ electron, we can label its eigen-states as $|3d_{m_l}\rangle$. Thus, our basis set can be transformed from the irreducible basis $\{|A_1\rangle, |A_2\rangle, |E\rangle, |T_1\rangle, |T_2\rangle\}$ to the angular momentum basis $\{|3d_{-2}\rangle, |3d_{-1}\rangle, |3d_0\rangle, |3d_1\rangle, |3d_2\rangle\}$. For the interested reader, Sugano et al. [37] discuss this transformation in detail, but we move past this material to the calculation of the crystal field energy.

2.3.5 Eigen-Energies of the Crystal Field

The wavefunctions $\phi_{\Gamma\gamma}$ for the E and T_2 levels can be recast in terms of hydrogenic wavefunctions. Here $\Gamma \in \{a_1, a, e, t_1, t_2\}$ labels the irreducible representation (often referred to as an *irrep*) and γ labels a particular row of the irrep. We use lower case

labels to remind ourselves that, strictly speaking, these are single-electron wavefunctions, though we have extend them to describe multi-electron quasi-particles. The set of labels for γ is different for each Γ. Here we label the two rows of the E irrep as u and v and we label the three rows of the T_2 irrep as ξ, η and ζ. These wavefunctions are illustrated in Figure 3 and have the form

$$
\begin{aligned}
\phi_{t_2\xi} &= i\frac{|3d_{-1}\rangle+|3d_1\rangle}{\sqrt{2}} \\
\phi_{t_2\eta} &= \frac{|3d_{-1}\rangle-|3d_1\rangle}{\sqrt{2}} \\
\phi_{t_2\zeta} &= i\frac{|3d_{-2}\rangle-|3d_2\rangle}{\sqrt{2}} \\
\phi_{ev} &= \frac{|3d_{-2}\rangle+|3d_2\rangle}{\sqrt{2}} \\
\phi_{eu} &= |3d_0\rangle
\end{aligned}
\qquad (2.3.5)
$$

Following the approach of Henderson and Imbusch [34] we note that, if the Born–Oppenheimer approximation holds, we can calculate

$$
\Delta E_{m_l m_{l'}} = \left\langle 3d_{m_l}\left|\hat{H}\right|3d_{m_{l'}}\right\rangle \approx \left\langle 3d_{m_l}\left|\hat{H}_0\right|3d_{m_{l'}}\right\rangle + \left\langle 3d_{m_l}\left|\hat{H}_{CF}\right|3d_{m_{l'}}\right\rangle. \quad (2.3.6)
$$

For example,

$$
\left\langle 3d_0\left|\hat{H}\right|3d_0\right\rangle = -\frac{6}{21}\frac{1}{4\pi\epsilon_0}\frac{7Ze^2}{2a^5}\left\langle r^4\right\rangle_{3d} = -6Dq, \qquad (2.3.7)
$$

where

$$
D = \frac{1}{4\pi\epsilon_0}\frac{35\sqrt{3}Ze^2}{a^5}, \qquad (2.3.8)
$$

and

$$
q = \frac{2}{105}\left\langle r^4\right\rangle_{3d}, \qquad (2.3.9)
$$

and where Ze is the charge of the nearest neighbor ions, a is the distance between the central ion and its nearest neighbors, and $\langle r^4 \rangle_{3d}$ is an overlap integral of the electronic wavefunctions. Note that the quantities D and q always appear as a product, thus we express the energy matrix in terms of the parameter Dq:

$$ E = \begin{bmatrix} -Dq & 0 & 0 & 0 & -5Dq \\ 0 & 4Dq & 0 & 0 & 0 \\ 0 & 0 & -6Dq & 0 & 0 \\ 0 & 0 & 0 & 4Dq & 0 \\ -5Dq & 0 & 0 & 0 & -Dq \end{bmatrix} \qquad (2.3.10) $$

We note the sum of each column is either $-6Dq$ or $4Dq$. As expected, the eigenvalues of each wavefunction are degenerate in Γ:

$$ E_{^5E} = E_e = -6Dq \qquad (2.3.11) $$

$$ E_{^5T_2} = E_{t_2} = 4Dq \qquad (2.3.12) $$

The crystal field splitting of the ^5D term is then $\Delta = E_{^5T_2} - E_{^5E} = 10Dq$.

Note that Δ is the energy separation between eigen-energies of the crystal-field Hamiltonian. We have considered, so far, terms in this Hamiltonian from the kinetic energy of the electrons, the attraction of the electrons to the nucleus, electrostatic repulsion of the electrons for each other, and a coulombic perturbation from neighboring ions. Note that the mutual electrostatic repulsion of d electrons varies from element to element. This electrostatic repulsion is described by the Racah parameters A, B and C [38]. Tanabe and Sugano have shown that, for the transition metals, A does not affect the energy difference between crystal field split levels [37]. They also measured values of B and C for several doubly and triply ionized $3d$ transition

26

metals and observed that $\gamma = C/B$ is nearly constant through the transition metal series. Thus, they parameterize the effect of crystal field splitting in terms of Dq and B so that different elements would not require separate diagrams. Figure 4 shows the Tanabe–Sugano diagram of crystal field splitting for the d^6 electron configuration. For the free Fe^{2+} ion, Tanabe and Sugano report $B = 917\ cm^{-1}$. Spectroscopically, we know that $10Dq \approx 2900\ cm^{-1}$ for Fe:ZnSe. Thus, $Dq/B \approx 0.3$, which corresponds to the left (high-spin) side of Figure 4, where the E level is still the ground level.

Figure 4. The Tanabe–Sugano diagram for the 3d^6 electron configuration in a tetrahedral crystal field. Equivalently, this diagram also applies to the 3d^4 electron configuration in an octahedral crystal field. Modified from Henderson and Imbusch Figure 3.22 [34].

27

2.3.6 Summary

In summary, from considerations of crystal symmetry and angular momentum, we have identified five eigen-functions for the $L = 2$ states of the Fe^{2+} ion, which we have labeled $\phi_{t_2\xi}$, $\phi_{t_2\eta}$, $\phi_{t_2\zeta}$, ϕ_{eu}, and ϕ_{ev}. We have determined that the crystal field of the ZnSe host splits the energy levels corresponding to these wavefunctions into two levels, T_2 and E, which have different values of energy separated by $10Dq$. The $\left|\phi_{\Gamma_\gamma}\right\rangle$ wavefunctions are each five-fold energy-degenerate with respect to spin and thus the E and T_2 state manifolds contain $2 \cdot 5$ and $3 \cdot 5$ energy-degenerate states respectively.

The insightful reader will immediately recognize that the correlation between symmetry breaking and energy splitting implies that additional distortions of the crystal which break the symmetry of the crystal field will lift these degeneracies. That topic was explored in rigorous detail by Low and Weger [39]. We will see, however, that even in the absence of such distortions there are other interactions which perturb the crystal field Hamiltonian and lift these degeneracies. In the next section, we consider coupling between the spin of the $3d^6$ electrons and orbital angular momentum of the core of the Fe^{2+} ion and its effect on the energy structure of the system.

2.4 Spin–Orbit Coupling

Now, we must consider the coupling of spin angular momenta of each electronic state to the angular momenta of the core of the active ion in the presence of the crystal field. Many optical spectroscopy textbooks contain the familiar solution to the Schrödinger equation in the absence of the crystal field. However, that solution does not apply because the ^5D term contains non-degenerate crystal-field terms. The Hamiltonian becomes

$$\hat{H} = \hat{H}_0 + \hat{H}_{CF} + \hat{H}_{SO}, \tag{2.4.1}$$

where $\hat{H}_{SO} = \eta \hat{L} \cdot \hat{S}$ is the spin–orbit perturbation. Low and Weger performed the first perturbation theory calculations of the eigenvalues of this system [39]. Their calculations are for the d^6 electron configuration in a *cubic* (octahedral) crystal field. The solution can be adapted to tetrahedral symmetry by substitution of the equation from page 77 of Henderson and Imbsuch [34]:

$$Dq_{T_d} = -\frac{9}{4}Dq_{O_h} \qquad (2.4.2)$$

They predict that the T_2 level will split into three sublevels Γ_1, Γ_2, and Γ_3 under the influence of the first order spin–orbit interaction (in this way, the T_2 behaves like an ordinary ^3D term). Those levels are again split by the second order interaction. The Γ_1 level splits into three sublevels Γ_1, Γ_4, and Γ_5. The Γ_2 level splits into two levels Γ_3 and Γ_4. The Γ_3 level is transformed into another single level Γ_5. The sublevels Γ_1, Γ_4, Γ_5, Γ_3, Γ_4 and Γ_5 have degeneracies 3, 3, 1, 3, 2, and 3 respectively. Low and Weger predict that the E level is not split by the first order interaction, but is split by the second order interaction into five sublevels Γ_2, Γ_5, Γ_3, Γ_4, and Γ_1 with degeneracies 1, 3, 2, 3, and 1 respectively.

Low and Weger assumed that the spin–orbit interaction did not mix terms from the E and T_2 states. Later, Villeret et al. introduced a small correction to the solutions of Low and Weger to account for this mixing. They give the eigenvalues of the Γ_n

sublevels of T_2 as

$$E_{\Gamma_1} = \Delta - 2\lambda + 24\frac{\lambda^2}{\Delta}\left(1 - 2\sigma - 20\sigma^2\right)$$

$$E_{\Gamma_4'} = \Delta - 2\lambda + 12\frac{\lambda^2}{\Delta}\left(1 - 20\sigma^2\right)$$

$$E_{\Gamma_5'} = \Delta - 2\lambda + \frac{12}{5}\frac{\lambda^2}{\Delta}\left(1 - \frac{32}{25}\sigma - \frac{4442}{625}\sigma^2\right)$$

$$E_{\Gamma_3} = \Delta + \lambda + 12\frac{\lambda^2}{\Delta}\left(1 + \sigma - 11\sigma^2\right) \tag{2.4.3}$$

$$E_{\Gamma_4} = \Delta + \lambda + 6\frac{\lambda^2}{\Delta}\left(1 - 3\sigma - 5\sigma^2\right)$$

$$E_{\Gamma_5} = \Delta + 3\lambda + \frac{18}{5}\frac{\lambda^2}{\Delta}\left(1 + \frac{63}{25}\sigma + \frac{4003}{625}\sigma^2\right),$$

and the γ_n sublevels of E as

$$E_{\gamma_2} = 0$$

$$E_{\gamma_5} = -6\frac{\lambda^2}{\Delta}\left(1 + \sigma + \sigma^2\right)$$

$$E_{\gamma_3} = -12\frac{\lambda^2}{\Delta}\left(1 + \sigma - 11\sigma^2\right) \tag{2.4.4}$$

$$E_{\gamma_4} = -18\frac{\lambda^2}{\Delta}\left(1 - \sigma - 15\sigma^2\right)$$

$$E_{\gamma_1} = -24\frac{\lambda^2}{\Delta}\left(1 - 2\sigma - 20\sigma^2\right),$$

with $\Delta = 10Dq$, λ, and σ as parameters. Here, we have adopted the primed notation for repeated T_2 levels and the lowercase notation for labeling the E levels introduced by Rivera-Iratchet [40] to avoid ambiguity in the labeling of levels and transitions. From the expressions for the eigenvalues of the system we can generate the energy level diagram as seen in Figure 5.

Udo et al. give the selection rules as shown in Table 8 [41]. Note that we are specifically referring to transitions from $^5T_2 \rightarrow {}^5E$ and not to transitions within each level. So, we find that nineteen allowed transitions of the form $\gamma_n \rightarrow \Gamma_{n'}$ will be ob-
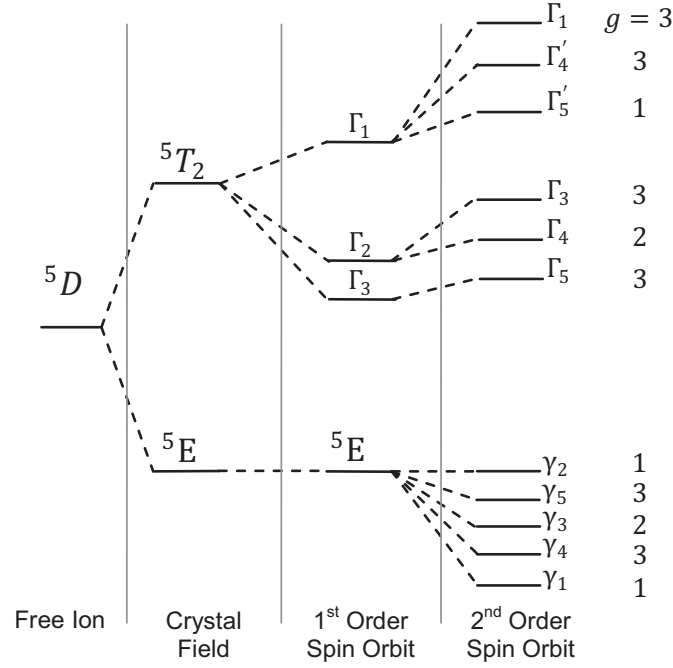
Figure 5. The energy level diagram of Fe^{2+} in a tetrahedral field with spin–orbit coupling.

served in absorption spectra. Similarly, we find that the nineteen allowed transitions of the form $\Gamma_n \to \gamma_{n'}$ will be observed in emission spectra. Figure 6 shows the allowed transitions in each case.

Table 8. The selection rules for Fe^{2+} ions from Udo et al. The state label Γ is used interchangeably with γ.

Initial State	Possible Final States
Γ_1	Γ_5
Γ_2	Γ_4
Γ_3	Γ_4, Γ_5
Γ_4	$\Gamma_2, \Gamma_3, \Gamma_4, \Gamma_5$
Γ_5	$\Gamma_1, \Gamma_3, \Gamma_4, \Gamma_5$

In summary, we have now parameterized the energy structure of the Fe^{2+} ion in a tetrahedral crystal field in terms of three parameters Δ, λ, and σ. We will later

|(a) Absorption | (b) Emission |
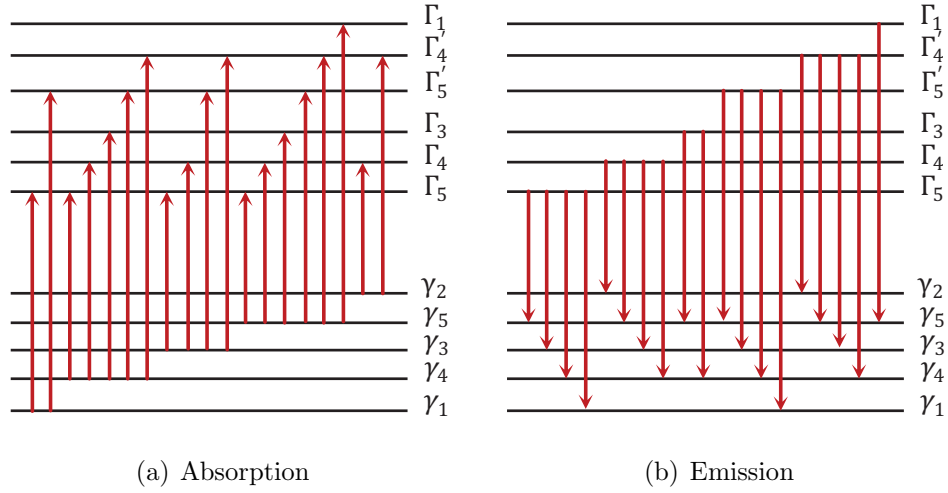
Figure 6. Predicted transitions between spin–orbit split levels of the Fe^{2+} ion in a tetrahedral crystal field.

combine this parameterization with the previously discussed degeneracies and thermal statistics to generate a temperature-dependent model of the absorption spectrum of Fe:ZnSe. In the next section, we will briefly consider coupling of the system to the vibrational normal modes of the host crystal.

2.5 The Jahn–Teller Term

An article by Ham explains why the Jahn–Teller effect, though completely general, is often not observed as expected in optical absorption spectra, even at low temperatures [42]. He also explains that the coupling implied by a Jahn–Teller term in the Hamiltonian affects the absorption spectrum in a different way than initially predicted by the casual reader. This has contributed to a perceived aura of mystery surrounding the Jahn–Teller effect among experimentalists. In this section, we attempt to demystify this effect in simple terms. We borrow heavily on Slack [43] and Ham [44] in the discussion which follows. We begin by considering the action of coupling the electronic wavefunctions to the motion of crystal lattice through the

Jahn–Teller term $\hat{H}_{JT}$. The system Hamiltonian becomes

$$\hat{H} = \hat{H}_0 + \hat{H}_{CF} + \hat{H}_{JT}. \qquad (2.5.1)$$

The form of the Jahn–Teller term will be discussed in more detail in the following subsections.

2.5.1 The Static Jahn–Teller Effect

The theorem of Jahn and Teller states that nonlinear molecules with orbital degeneracies are unstable [45]. In the context of crystals, this means that spatial configurations of ions which leave two or more electronic orbitals degenerate in energy are intrinsically unstable against distortions which lift the degeneracy. The shape of such distortions correspond to a displacement in the direction of one of the vibrational normal modes of the T_d point group. Such distortions act to reduce the overall symmetry of the problem. In this case, the tetrahedral symmetry T_d of the tetrahedron is reduced to tetragonal symmetry D_{4d}. The effect of this reduction in symmetry is to lift the energy degeneracy of electronic orbitals in both the ^5E and the $^5T_2$ terms.

Recall that we have used the terms E and T_2 to label the crystal field-split energy levels as well as the blocks of the irreducible matrix representation of the group operators. Now, if we consider the 2×2 E block, we can diagonalize it into two 1×1 blocks which we label A_1 and B_1. The 3×3 T_2 block can be block diagonalized into a 1×1 B_2 block and a 2×2 E block. One can imagine repeating the math of Subsection 2.3.3 to understand the splitting nomenclature in greater detail, but it will suffice to say that we could label the new energy levels with the labels of the new irreducible representations.

Now, one can easily imagine that the new ^5E level has orbital degeneracy which will induce another Jahn–Teller distortion. This will reduce the tetragonal symmetry

D_{4d} of the problem to dihedral symmetry D_{2d}. The effect will be to split the ^5E energy level into a $^5B_1$ and a $^5B_2$ energy level. At this point, all the orbital degeneracy has been removed and we are left with five distinct energy levels. This is the so-called *static* Jahn–Teller effect.

Our familiar approach of treating physical interactions as a small perturbation to system Hamiltonian breaks down somewhat at this point. We are constrained by the BOA to incorporate one of these effects at a time and in the order of greatest perturbation to least. We do not know at this point whether the static Jahn–Teller distortion or the spin–orbit coupling will correspond to the greatest splitting in energy, or even if these effects are truly separable as we have assumed, so we are left with some ambiguity in our description of the system. Low and Weger discuss this ambiguity in rigorous detail [39]. They explore the energy structure of divalent iron in a crystal field in three cases:

1. an axial distortion with a corresponding energy splitting greater than the first order spin–orbit splitting,

2. an axial distortion with a corresponding energy splitting less than the first order spin–orbit splitting but greater than the second order splitting,

3. no axial distortion of the crystal field.

In the decades since this study was published in 1960, spectroscopic investigators have concluded that static Jahn–Teller distortion is not observed in Fe:ZnSe (corresponding to Case 3 above). Thus, the energy structure derived in the absence of the Jahn–Teller effect (Section 2.4) is accepted as valid. Thus, we will later use the notation of that section to label the transitions observed experimentally in Fe:ZnSe. Note, however, that the static effect is not ruled out for transition-metal-doped II–VI materials in general. For example, the static effect is observed clearly in the Ti:AlO$_3$

system [46], and so may play a role in other Fe^{2+}-doped II–VI materials.

2.5.2   The Dynamic Jahn–Teller Effect

In the previous section, we concluded that the static Jahn–Teller effect is not observed in Fe:ZnSe. Yet, in this section, we will consider the effect of the Jahn–Teller term on the behavior of the Fe–Se system. This is a potential point of confusion for the reader and a common point of confusion for the experimentalist. Contributing to this confusion is that there is not one unique *Jahn–Teller effect.* However, there is exactly one unique Jahn–Teller theorem which motivates the addition of exactly one Jahn–Teller term to the electronic Hamiltonian. However, this term is responsible for multiple effects. Consider the original statement of the theorem:

> Except for linear molecules, only orbitally non-degenerate states…can correspond to stable configurations [47].

We expect the ground state of the active ion to be stable; thus, the natural conclusion is that (since the crystal is obviously not a linear molecule) the ^5E ground level is split in two such that the orbital degeneracy is lifted and stability is restored. Such a distortion reduces the overall symmetry of the problem and thus we expect that the $^5T_2$ state to also split (see Subsection 2.5.1). However, this view overlooks that the Jahn–Teller coupling between the ion and the normal modes of the solid must itself have tetrahedral symmetry. Thus, this term is also block diagonalized by the unitary transformation that block diagonalizes the preceding Hamiltonian. Thus the Jahn–Teller distortion(s) also belong to the irreducible representation of the tetrahedral point group. These terms then, do not couple the states of the irreducible representations ^5E and $^5T_2$ nor do they couple the degenerate states within these terms. Thus, the states belonging to each term may remain orbitally degenerate and the expected distortion(s) may not occur. If the degeneracy is not lifted, no static

(sometimes called *spontaneous*) Jahn–Teller effect will be observed in the optical spectra of the material.

Note, however, that the Jahn–Teller theorem is general and so the Jahn–Teller perturbation does indeed couple the electronic states to the motion of the nuclei even if the orbital degeneracy of an irreducible representation is not removed. That is, the wavefunctions corresponding to these states now contain a vibrational and an electronic component. The vibrational components modify the electronic wavefunctions such that the overlap integrals between them increase. Thus, even near $0\ K$, the configuration does not achieve a stationary state because that state can tunnel into a nearby *vibronic* state. Thus the motion of the electrons is not localized to small changes about a single static configuration. Thus, much structure is observed in the optical spectra of these ions, even at very cold temperatures. The structure is typically very broad due to the motion of the nuclei. The Jahn–Teller coupling also has the effect of modifying the spin–orbit splitting of the ionic terms. Thus, it is frequently observed that the degree of energy level splitting predicted by simulations utilizing the spin–orbit coupling theory is much greater than that which is observed experimentally. This simultaneous quenching of spin–orbit splitting and the appearance of broad spectral structure due to *phonon-assisted* transitions is referred to as the *dynamic* Jahn–Teller effect.

It can be shown, that the dynamic effect and static effect are in fact limiting cases of the same physics. Without proof, we present the result that the static case corresponds to the situation in which the Jahn–Teller energy (the energy reduction corresponding to a static distortion of the configuration of the nuclei away from the symmetric configuration) is much greater than the zero-point phonon energies of the host crystal. If this relationship does not hold, the coupling gives rise to the dynamic case [42]. Thus, we do not expect to observe the static and dynamic effects

simultaneously.

2.5.3   Phonon Effects

We have seen that the Jahn–Teller term couples the vibration of the host ions to the electronic motion of the active ion. The motion of the ions in a crystal lattice is frequently modeled as the motion of many masses connected by springs. The dynamics of such a system are defined by Newton's second law of motion and Hooks law for the force of a spring

$$|F\rangle = m\frac{d^2}{dt^2}|x\rangle = -\hat{k}|x\rangle , \tag{2.5.2}$$

where

$$|x\rangle = \begin{bmatrix} \langle E|\,x\rangle \\ \langle C_{3,1}|\,x\rangle \\ \vdots \\ \langle \sigma_{d,6}|\,x\rangle \end{bmatrix} . \tag{2.5.3}$$

The solution to this equation, like the solution to the Schrödinger equation, is an eigenvalue problem. Thus, it is not surprising that the method of solution is to transform to problem to the irreducible representation and block diagonalize the force matrix. We present the results without performing the calculation explicitly: The eigenvalues and eigenvectors of each block label the normal modes of vibration within the solid. The normal modes are the solutions to the system of equations represented by the force matrix equation. The result is the prediction of five normal modes of vibration which we can be labeled by their corresponding symmetries A_1, A_2, E, T_1, and T_2. As is turns out, states stemming from the E manifold couple only the E modes of vibration, and states stemming form the T_2 manifold couple only to T_2 modes of vibration. This insight allows us to express the Jahn–Teller term in

terms of the familiar Hamiltonian of two (for E) or three (for T_2) coupled harmonic oscillators.

For the E states, the vibrational Hamiltonian is then

$$\hat{H}_{v,E} = \hbar\omega_E \left(\hat{a}_u^\dagger \hat{a}_u + \hat{a}_v^\dagger \hat{a}_v + 1 \right), \tag{2.5.4}$$

where $\hat{a}_\gamma^\dagger$ and $\hat{a}_\gamma$ are the creation and annihilation operators for modes with energy $\hbar\omega_E$. The familiar solutions to the Schrödinger equation are

$$\hat{H}_{v,E} \left| n_E m_E \right\rangle = \hbar\omega_E \left(n_E + m_E + 1 \right) \left| n_E m_E \right\rangle. \tag{2.5.5}$$

The approch of Rivera-Iratchet [40] to describe the Jahn–Teller mechanism is to use coupling operators D_γ to couple these vibrational wavefunctions to the electronic ones. The form of the Hamiltonian is

$$\hat{H}_{JT,E} = K_E \left[\left(\hat{a}_u^\dagger + \hat{a}_u^\dagger \right) \hat{D}_u + \left(\hat{a}_v^\dagger + \hat{a}_v^\dagger \right) \hat{D}_v \right]. \tag{2.5.6}$$

Likewise, for T_2 states

$$\hat{H}_{v,T_2} = \hbar\omega_{T_2} \left(\hat{a}_\zeta^\dagger \hat{a}_\zeta + \hat{a}_\eta^\dagger \hat{a}_\eta + \hat{a}_\xi^\dagger \hat{a}_\xi + 3/2 \right), \tag{2.5.7}$$

$$\hat{H}_{v,T_2} \left| n_{T_2} m_{T_2} l_{T_2} \right\rangle = \hbar\omega_{T_2} \left(n_{T_2} + m_{T_2} + k_{T_2} + 3/2 \right) \left| n_{T_2} m_{T_2} l_{T_2} \right\rangle, \tag{2.5.8}$$

and

$$\hat{H}_{JT,T_2} = K_{T_2} \left[\left(\hat{a}_\zeta^\dagger + \hat{a}_\zeta^\dagger \right) \hat{D}_\zeta + \left(\hat{a}_\eta^\dagger + \hat{a}_\eta^\dagger \right) \hat{D}_\eta + \left(\hat{a}_\xi^\dagger + \hat{a}_\xi^\dagger \right) \hat{D}_\xi \right]. \tag{2.5.9}$$

Thus the final form of the system Hamiltonian is

$$\hat{H} = \hat{H}_0 + \hat{H}_{CF} + \hat{H}_{SO} + \hat{H}_{JT}, \tag{2.5.10}$$

where $\hat{H}_{JT} = \hat{H}_{JT,E} + \hat{H}_{JT,T_2}$. Thus we see that each of the electronic energy levels of Figure 6 is the ground level for a vibrational harmonic oscillator potential whose eigenvalues are like rungs of a ladder separated by one phonon of energy. Thus, transitions between states are observed to be modified by quanta of energy corresponding to the energy of an integer number of phonons.

The fractional populations occupying these states are described by Maxwell–Boltzmann statistics. Thus, the population distribution of these vibronic levels change with temperature. In the next subsection, we will discuss effects associated with the change of this population distribution with temperature.

Observationally, zincblende structures are seen to have six eigen-energies of vibration which correspond to specific vibrational frequencies. We label these phonons T (transverse) or L (longitudinal), and O (optical) or A (acoustic). The labels T and L distinguish the type of wave propagation apparent in the material. The labels A and O distinguish whether the motion of heterogeneous adjacent nuclei is aligned or anti-aligned respectively. Thus the literature refer to one LA, one LO, two TA, and two TO phonons. The exact relationship between these labels and the irreducible representation of the vibrational normal modes is unimportant. However, we take the eigenvalues of energy measured for these six phonons to be the eigenvalues associated with the harmonic oscillators described previously.

Now, in real materials, these six phonons do not simply assume a single value of energy. The energy of the phonons is seen to change with respect to the direction of wave propagation within the crystal. Figure 7 shows the phonon dispersion curves for ZnSe as calculated by Hennion et al. [48] from inelastic neutron scattering (INS)

data. The phonons occupy the allowed modes of vibration with a calculable density as shown in Figure 8. Clearly, the acoustic phonons experience a great deal of dispersion and are not as highly localized as the optical phonons.
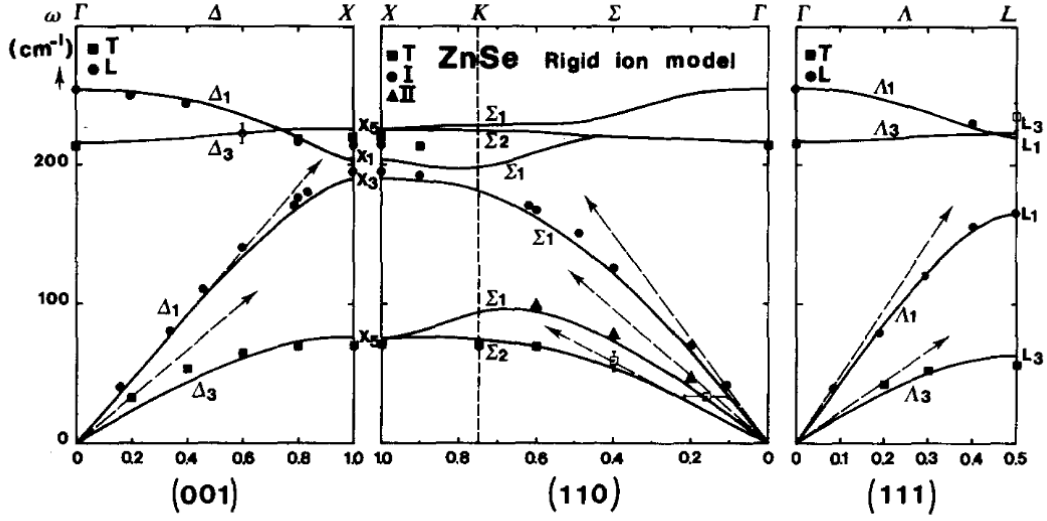
Figure 7. Phonon dispersion curves calculated from INS data for room-temperature ZnSe from Hennion et al. [48].
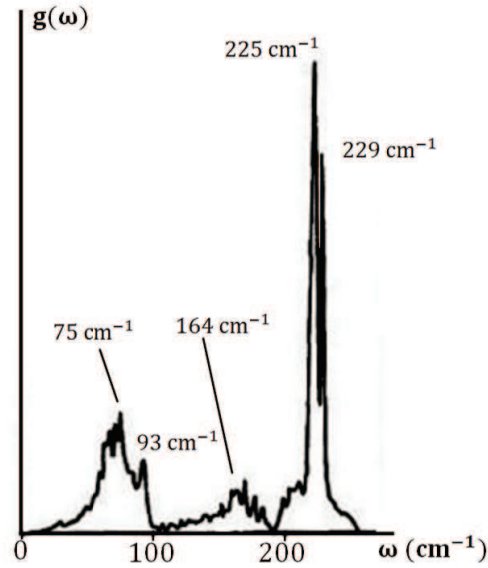
Figure 8. The calculated phonon density of states for room-temperature ZnSe. Modified from Hennion et al. [48].

40

2.5.4 Summary

We will see in the next section that the optical transitions between two electronic states can be assisted by one or more phonons. Thus, the photon energies involved this these phonon-assisted transitions will differ from the energy separation of the two electronic levels by an integer number of phonons. Phonon-assisted transitions, especially those involving many phonons, play a significant role in the room-temperature optical behavior of Fe^{2+} ions in ZnSe. Their role will be explored in more detail in the next section.

2.6 The Configuration Coordinate Model

Let us introduce the *configuration coordinate* Q, which will serve as a spatial index of the probability density function $\psi(Q)$ which describes the location of an electron in a vibrational potential. The Franck–Condon principle states that the probability P of a transition between a state ψ and a state ψ' is the integral

$$P = \langle \psi' | \, \hat{\mu} \, | \psi \rangle = \int \psi'(Q) \, \hat{\mu}(Q) \, \psi(Q) \, dQ, \qquad (2.6.1)$$

where $\hat{\mu}$ is the dipole moment operator. Here the wavefunctions correspond to the states of two harmonic oscillators as shown in Figure 9. Thus P effectively describes the probability that a photon of energy $E_\psi - E_{\psi'}$ is emitted. An illustration of the principle is shown in Figure 10.
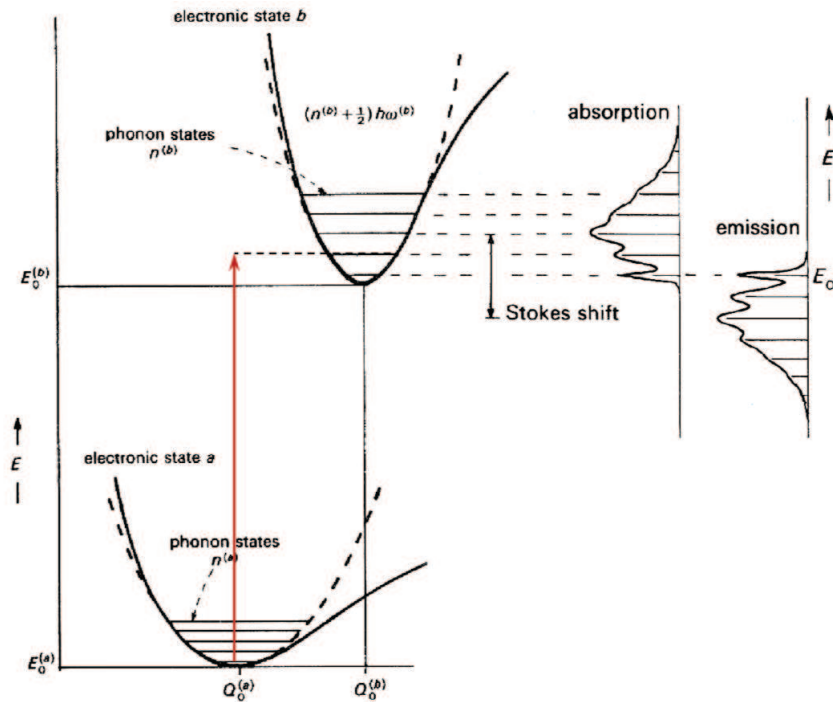
Figure 9. The configuration coordinate model of vibronic transitions between two states. Modified from Figures 5.5 and 5.12 of Henderson and Imbusch [34].

Figure 10. An illustration of the Franck–Condon principle. The Franck–Condon factor for transitions from $\chi_a(0) \to \chi_b(m')$ is large because their respective wavefunctions achieve their maxima at the same point in Q. Modified from Henderson and Imbusch Figure 5.9 [34].
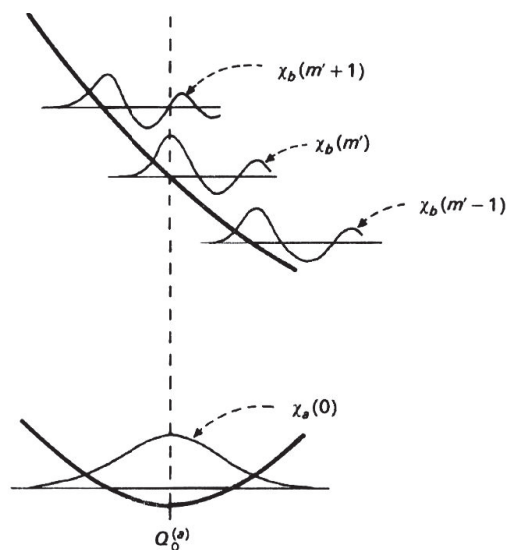
2.6.1   Thermal Statistics

Recall that electrons are fermions and will obey Maxwell–Boltzmann statistics. Thus, the population of each level is determined by its energy E realative to the ground state, and the temperature T of the sample. Thus the fractional occupancy of the ith level is

$$\frac{N_i}{N_0} = \frac{g_i}{g_0} \exp\left(-E/k_b T\right), \qquad (2.6.2)$$

where k_b is Boltzmann's constant and g_i is the degeneracy of the ith energy level.

As T approaches 0 K, only the γ_1 ground state will have non-zero population. Thus, in low-temperature absorption spectra, we expect only to see lines corresponding to transitions involving integer number of phonons associated with the T_2 upper state manifold. Transitions from the ground level to purely electronic levels in the upper state manifold will correspond to well defined *zero-phonon* lines in the optical absorption spectrum. Transitions involving one or more phonons will be greater in energy than the corresponding zero-phonon line (ZPL). These are the so-called *Stokes* lines of an optical absorption spectrum. Now, for $T > 0$ K, additional vibronic levels of the E bottom manifold will be populated. Thus, differences of integer numbers of phonons may now be negative and transition lines appear at energies lower than the zero-phonon line. These are the so-called *anti-Stokes* lines of an optical absorption spectrum.

When the T_2 upper state manifold is populated by laser-induced absorption from the ground state, the electron population will quickly (on the order of picoseconds) redistribute according to Maxwell–Boltzmann statistics. Thus, as T approaches 0 K, only the lowest level Γ_5 of the of the upper state manifold will have non-zero population. Thus, in emission, we expect only to see lines corresponding to transitions

involving integer number of phonons associated with the ground state manifold. Transitions from the Γ_5 level to purely electronic levels in the ground state manifold will correspond to well defined ZPLs in the optical fluorescence spectrum. Transitions involving one or more phonons will be lower in energy than the corresponding ZPL. These are the Stokes lines of an optical emission spectrum. Now, for $T > 0\ K$, additional vibronic levels of the upper manifold will be populated. Thus, differences of integer numbers of phonons may now be negative and transition lines appear at energies greater than the zero-phonon line. These are the anti-Stokes lines of an optical emission spectrum.

In both absorption and emission, phonon-assisted transitions will contribute to Stokes and anti-Stokes lines that are broader than the ZPLs due to phonon dispersion (see Figures 7 and 8). As the temperature T increases, phonon-assisted transitions will dominate the absorption and emission spectra. In Sections 3.1 and 3.2, we will see that such transitions blur together to create broad absorption and emission bands in Fe:ZnSe.

2.6.2   Multi-Phonon Transitions and Non-Radiative Quenching

Recall that the vibrational coupling between electronic states of the Fe^{2+} ion and the vibrational states of the ZnSe lattice is described by several harmonic oscillator potentials. These potentials are idealized as parabolic energy curves in the configuration coordinate Q. In general, these potentials achieve their minima at different values of Q and expand at different rates $\partial E / \partial Q$. For simplicity, we will assume that the electronic states are coupled by interactions involving only phonons of one specific frequency ω_{eff}. In this case, $\partial E / \partial Q$ will be the same for the upper and lower parabolae. Still, we see that the parabolae of the upper and lower harmonic oscillator potentials will intersect at some point X (see Figure 11).
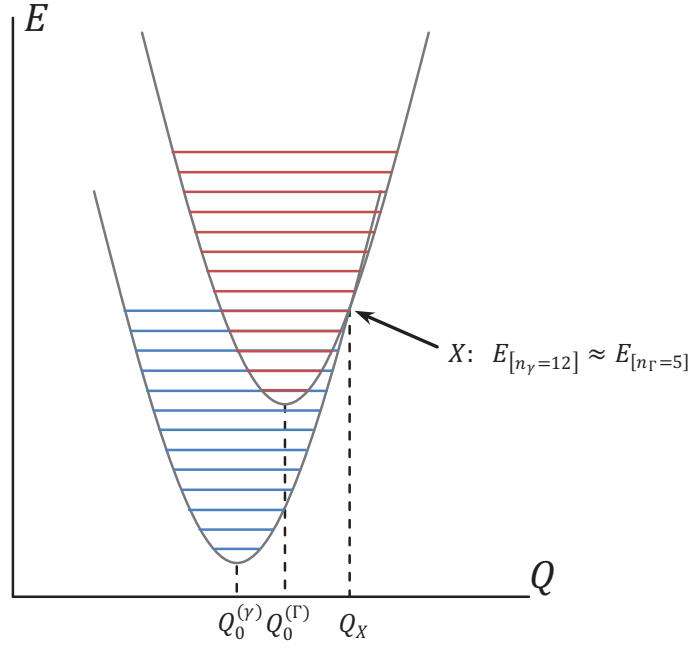
Figure 11. The quantum harmonic oscillator potentials overlap at some point X promoting tunneling between upper and lower vibrational states.

Consider the case that the upper-state manifold is populated by optical absorption from the ground state manifold. At T near 0 K, we expect the excited population to enhabit only the lowest energy level of the upper state. The wavefunction(s) corresponding to this energy level do not overlap substantially with wavefunctions belonging to the lower state manifold. However, as T increases, the upper vibrational levels of the upper state manifold will become increasingly populated. At some temperature, some of the population will enhabit T_2 states whose vibronic wavefunctions overlap significantly with the wavefunctions of E states. Some of these excited electrons will tunnel from an T_2 state to an E state. The population of the E manifold will re-distribute to achieve thermal equilibrium and the electron makes the transition from the T_2 manifold to the E manifold by near-simultaneous emission of many phonons, instead of a single photon. This process is non-radiative and competes with the radiative processes. The radiative and non-radiative processes occur in parallel;

so the upper-state lifetime of an ion can be written

$$\tau = (W_r + W_{nr})^{-1}. \tag{2.6.3}$$

Now, an ion's upper-state lifetime τ is the average time that an electron of that ion stays in an excited state. Thus τ is a measure of how readily the population in the material can be inverted (for lasing). The radiative rate is determined by the physics of the system and is not directly accessible to external control. The non-radiative rate depends directly on the temperature of the system, so we attempt to maximize τ by setting the non-radiative transition rate $W_{nr} = 0$.

The upper-state lifetime can be written in terms of the fluorescence efficiency

$$\eta = \frac{W_r}{W_r + W_{nr}}. \tag{2.6.4}$$

Specifically,

$$\tau = (W_r + W_{nr})^{-1} = \frac{\eta}{W_r} = \eta\tau_r. \tag{2.6.5}$$

Thus, we see the ion's total lifetime decreases as the fluorescence efficiency is reduced. This effect is referred to as *non-radiative quenching* of lifetime. Henderson and Imbusch discuss at length the role of multi-phonon transitions in a solid state laser material (Section 5.8.2 of [34]). They give the nonradiative decay probability as

$$W_{nr}^{(p)}(T) = W_{nr}^{(p)}(0)(1 + n_{eff})^p, \tag{2.6.6}$$

where T is the temperature in Kelvin and p is the number of phonons of energy

46

$E = \hbar\omega_{eff}$ required to bridge the gap between some pair of energy levels and

$$n_{eff} = \frac{1}{\exp\left(\hbar\omega_{eff}/k_b T\right) - 1} \qquad (2.6.7)$$

is the effective occupancy of the corresponding effective phonon mode. The expression for n_{eff} clearly contains the familiar Boltzmann distribution, thus we can see that $(1 + n_{eff})^p$ describes the effect on the probability of non-radiative decay due to a change in the population distribution induced by a change in temperature.

Henderson and Imbusch reprint Miyakawa and Dexter's [49] expression for W_{nr} at $T = 0\ K$. The rate of nonradiative transitions at $T = 0\ K$ is

$$W_{nr}^{(p)}(0) \approx \frac{R^2 e^2}{\sqrt{2\pi p}} \exp\left(-\beta\left(p - 2\right)\right), \qquad (2.6.8)$$

where $\beta = \log\left(\frac{p}{S}\right) - 1$ and R is a matrix element of the form

$$R_{ab}^{(k)} = -\frac{\hbar^2}{M} \left\langle \psi_a \left| \frac{\partial}{\partial Q_k} \right| \psi_b \right\rangle, \qquad (2.6.9)$$

and where S is the Huang-Rhys parameter[3] and k labels the mode of vibration of the lattice nuclei with effective mass M. Thus,

$$W_{nr}^{(ab)} \approx \left(-\frac{\hbar^2}{M} \left\langle \psi_a \left| \frac{\partial}{\partial Q_k} \right| \psi_b \right\rangle\right)^2 \frac{e^2}{\sqrt{2\pi p}} \exp\left(-\beta\left(p - 2\right)\right). \qquad (2.6.10)$$

We ignore the integral $\left\langle \psi_a \left| \frac{\partial}{\partial Q_k} \right| \psi_b \right\rangle$ because we do not have an expression for the

---

[3]S is also called the electron–phonon coupling parameter. Henderson and Imbusch give $S \approx 0.05$ for rare-earth ions (page 255 of [34]). They also indicate that the value of S varies from ion to ion among the transition metals. Thus transition metal ions can be much more sensitive to the vibration of the host in which they reside.

wavefunctions $|\psi\rangle$. Thus, we note

$$W_{nr} \propto \frac{1}{M^2\sqrt{2\pi p}} \exp\left(-\beta\left(p-2\right)\right) = \frac{1}{M^2\sqrt{2\pi p}} \left(\frac{Se}{p}\right)^{p-2}. \qquad (2.6.11)$$

We immediately note that, if T is small enough that $(1 + n_{eff})^p \approx 1$, the probability of non-radiative transitions will decrease as M and p become large.

Thus, we conclude that the non-radiative processes which quench the fluorescence of Fe^{2+} ions in II–VI materials are dependent on the mass of the host ions. Now, we cannot arbitrarily increase M, but suppose that Zn and Se could be replaced by more massive elements in their respective columns of the periodic table such as Cd or Hg for Zn or Te for Se. The resulting increase in the effective mass M will bring about a decrease in the phonon frequency ω_{eff} of the vibrational modes of the material. Thus, for some optical transition of energy E, the number of phonons $p = E/\omega_{eff}$ required to bridge the gap will also increase. Thus, we expect such materials to exhibit a reduced degree of NRQ when compared to Fe:ZnSe. However, we also see that the substitution of heavier host ions will also change the average inter-ionic spacing a of the host and lower the energy of the crystal field. Thus, p may not increase as expected and the spectral peak of absorption and fluorescence will be longer for such materials than for Fe:ZnSe (at the same temperature). This approach to mitigating NRQ could be useful for temperature scaling of CW Fe^{2+} lasers. This approach will be addressed briefly in Section 3.4.

2.6.3 Summary

In summary, we have discussed a wide range of physics that determine the optical behavior of Fe^{2+} ions in II–VI materials. In the following sections, we turn to experiments which demonstrate the behavior described in this chapter. Laser-induced fluorescence and absorption spectroscopy data are used to find approximate values

of Δ, λ, and σ. Thus, the eigen-energies of the Fe^{2+} ion in ZnSe are estimated. The upper-state lifetime of Fe^{2+} ions in ZnSe is measured with respect to changes in temperature. Insights from the theory developed to this point are used to explain the observed behavior.

III. Spectroscopy of Fe:ZnSe

3.1 Absorption Spectroscopy of Fe:ZnSe

An *ARS* cryostat was used to provide control of the temperature of a small sample of Fe:ZnSe. The cryostat used CaF_2 windows, which allowed transmission of mid-IR radiation. The cryostat was positioned in the sample compartment of a *Nicolet 6700* series Fourier transform infrared spectrometer (FTIR) as shown in Figure 12.
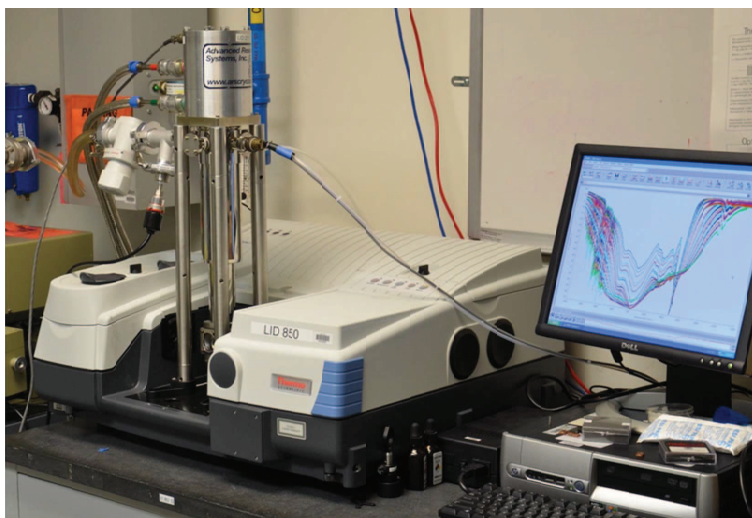
Figure 12. The ARS cryostat in the sample compartment of a Nicolet 6700 FTIR.

The FTIR was used to collect absorption spectra of Fe:ZnSe (see Figure 13) from $T = 10$ to $300\ K$. Note that as the temperature of the crystal increases, the population moves out of the ground state and the spectral absorption changes dramatically. Thus, there is a general trend of the sharp low-temperature absorption features blurring together at higher temperatures. Most noticeably, the zero-phonon transition lines, which absorb very strongly at low temperatures, decrease by an order of magnitude from $10\ K$ to $50\ K$.

The spectrum collected at $T \approx 10\ K$ exhibits a great deal of structure. From
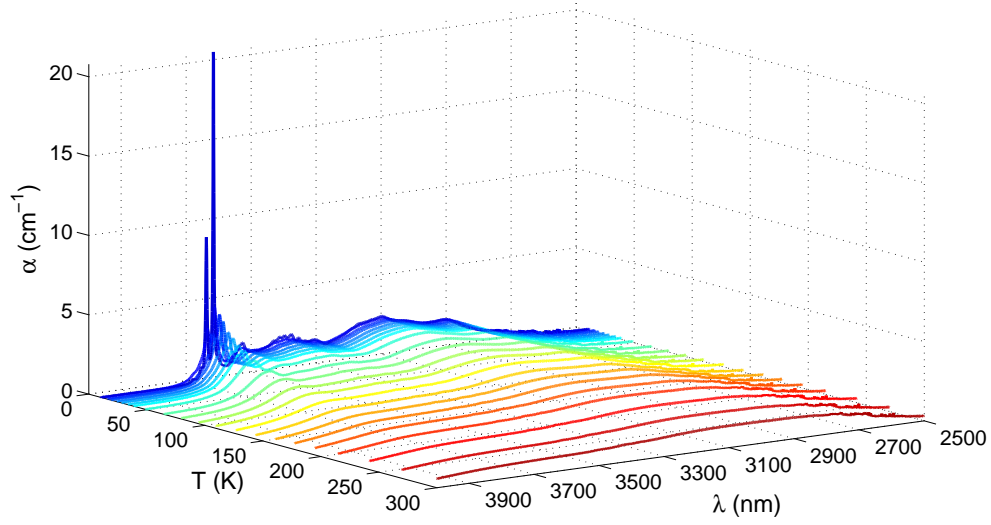
(a) Broad view
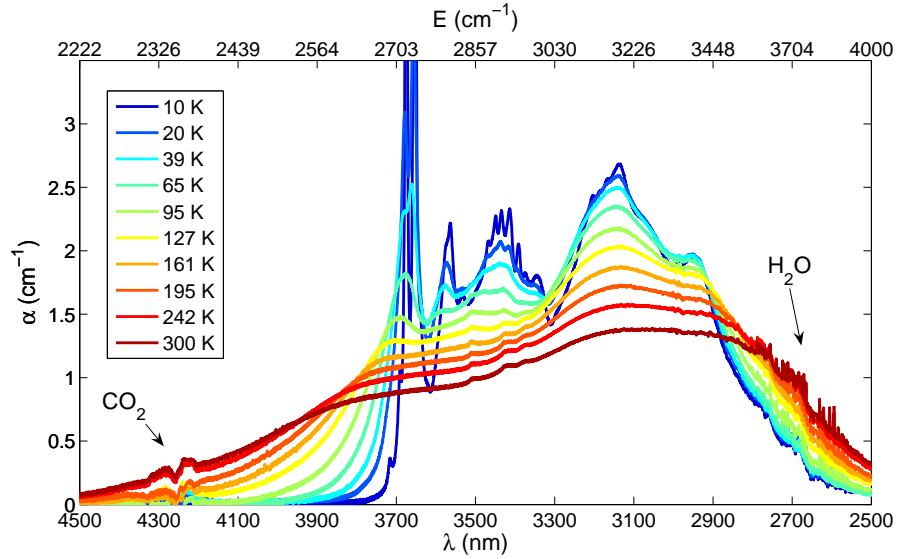
(b) Detail view

Figure 13. **The absorption spectrum of Fe:ZnSe plotted at a range of temperatures from 10 K to 300 K.**

the measured structure it is also possible to perform a fit to the observed absorption lines. Recall that Low and Weger parameterized the energy levels of the Fe^{2+} ion in terms of Δ, λ, and σ. Thus, it is possible to construct a system of three equations to solve for these parameters. For this purpose, it was assumed that the prominent

lines in the absorption spectrum at 2737, 2721, 2709 and 2691 cm^{-1} corresponded to $\gamma_n \rightarrow \Gamma_5$, transitions. Thus we obtain expressions for the transition energies:

$$E_{\Gamma_5} - E_{\gamma_1} = \Delta + 3\lambda + \frac{\lambda^2}{\Delta}\left(\frac{138}{5} - \frac{4866}{25}\sigma - \frac{1427946}{3125}\sigma^2\right) = 2737 \ cm^{-1}$$

$$E_{\Gamma_5} - E_{\gamma_4} = \Delta + 3\lambda + \frac{\lambda^2}{\Delta}\left(\frac{91}{5} - \frac{1737}{25}\sigma - \frac{828497}{625}\sigma^2\right) = 2721 \ cm^{-1} \qquad (3.1.1)$$

$$E_{\Gamma_5} - E_{\gamma_3} = \Delta + 3\lambda + \frac{\lambda^2}{\Delta}\left(\frac{78}{5} + \frac{2013}{25}\sigma - \frac{397247}{625}\sigma^2\right) = 2709 \ cm^{-1}$$

Each expression describes a three-dimensional surface, for which we treat Δ as dependent on λ and σ. The magnitude of the separation $\mathcal{R}$ between two surfaces Δ_{mn} and $\Delta_{m'n'}$ is $\|\Delta_{mn} - \Delta_{m'n'}\|$ so the combined distance between the surfaces of interest can be expressed

$$\mathcal{R}(\lambda, \sigma) = \sum_{nn'} \|\Delta_{5n} - \Delta_{5n'}\| = \|\Delta_{51} - \Delta_{53}\| + \|\Delta_{51} - \Delta_{54}\| + \|\Delta_{54} - \Delta_{53}\| \quad (3.1.2)$$

An inexact solution to the system of equations was found by finding the values of λ and σ which minimized $\mathcal{R}$. Two classes of solution exist, one with positive values of λ and another with negative values of λ, but the negative solution was chosen to make $E_{\gamma_n \rightarrow \Gamma_5} < E_{\gamma_n \rightarrow \Gamma'_5}$. We found that $\mathcal{R}$ was minimized at $\lambda = -82.31 \ cm^{-1}$ and $\sigma = -0.001150$, at which $\Delta_{51} = 2920 \ cm^{-1}$. These parameters then determine the spectral location of the 19 allowed transitions $\gamma_n \rightarrow \Gamma_m$ (see Equation 2.4.3). The relative heights of these spectral lines can be predicted from:

$$I_{\Gamma\gamma} = A_{FC} \cdot g_{\Gamma_m} g_{\gamma_n} \exp\left(-\frac{E_{\gamma_n} - E_{\gamma_1}}{k_B T}\right) \qquad (3.1.3)$$

where A_{FC} is the Franck–Condon overlap factor, g_{Γ_m} is the degeneracy of the upper state, g_{γ_n} is the degeneracy of the lower state, and the exponential term is the familiar Boltzmann expression which describes the thermal occupancy of the γ_n state relative

to the ground state γ_1. The stick spectrum generated by this model is shown in Figure 14. The Franck–Condon factor of each transition was assumed to be unity, but the degeneracy values of each state are supplied by the model of Low and Weger.
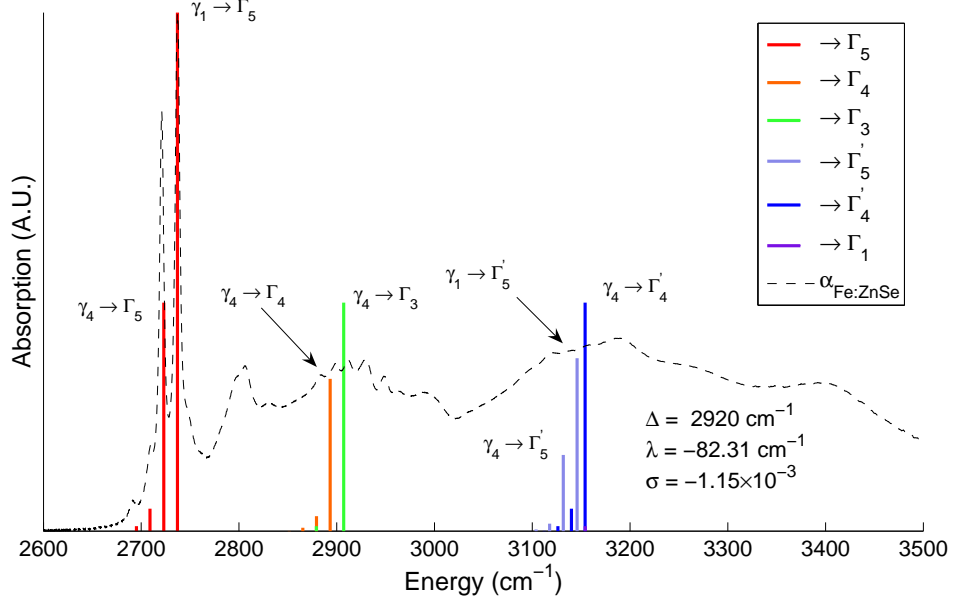
Figure 14. The fit of the eigenvalues of the electronic states of Fe^{2+} ions to the absorption spectrum of Fe:ZnSe at T = 10 K.

From Figure 14, we can assign some of the transitions predicted by the model to specific features in the absorption data. We assign the lines at 2691, 2709, 2721, and 2731 cm^{-1} to the $\gamma_5 \to \Gamma_5$, $\gamma_3 \to \Gamma_5$, $\gamma_4 \to \Gamma_5$, and $\gamma_1 \to \Gamma_5$ transitions respectively. We can say with some confidence that the lines observed from 2880 to 2960 cm^{-1} are due to transitions to the Γ_4 and Γ_3 levels and that the structure observed from 3120 to 3200 cm^{-1} are due to transitions to the Γ_5', Γ_4', and Γ_1 levels. From this we can also assign structure near 2800 cm^{-1}, 3000 cm^{-1}, and beyond 3200 cm^{-1} to phonon-assisted mechanisms in rough agreement with the phonon density of states shown in Figure 8.

The agreement of the fit of the model to the data is surprisingly good. However, the agreement of the model to the data is enhanced if we increase the modeled temper-

ature from 10 K to 15 K^1 (see Figure 15). The error of the temperature measurement is unknown and the thermistor used to measure the temperature was affixed to the cold finger of the cryostat, not in direct contact with the Fe:ZnSe sample. Thus, the 5 K disparity between the model and the measured temperature of the cold finger is believable.
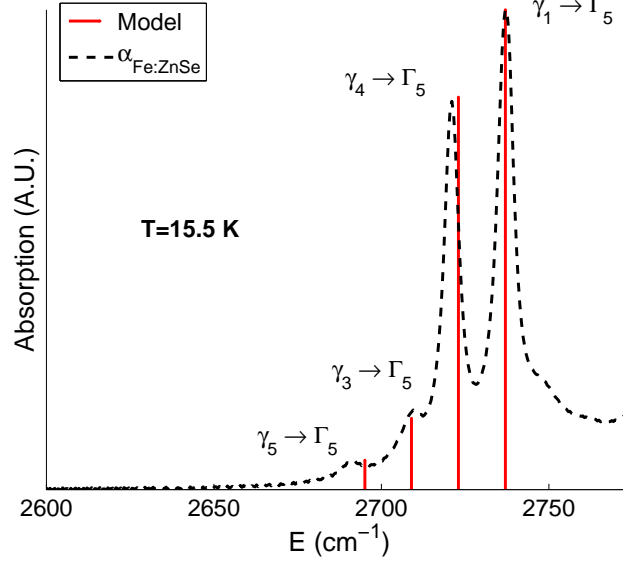
Figure 15. The predicted absorption spectrum of Fe:ZnSe at 15.5 K superimposed on the measured absorption spectrum. Slight displacements of the measured lines from modeled wavelength are consistent with the dynamic Jahn–Teller effect.

Note that we have constrained the $\gamma_1 \rightarrow \Gamma_5$ transition of the model to match the corresponding feature in the absorption data. From Figure 15 we see that the other $\gamma_n \rightarrow \Gamma_5$ transitions are slightly displaced from the corresponding features in the recorded spectrum. These slight deviations are consistent with the dynamic Jahn–Teller effect.

Furthermore, we observe the transitions which do not terminate in the Γ_5 level are predicted to be an order of magnitude stronger than observed. Since the relative heights of the $\gamma_n \rightarrow \Gamma_5$ transitions are accurately predicted by the model, we hypoth-

---

[1]If we compensate for the overlap of neighboring lines, the model is well-matched to the data at 12.5 K.

esize that the Franck–Condon factors of the $\gamma_n \to \Gamma_4$ and $\gamma_n \to \Gamma_3$ transitions are about an order of magnitude smaller than the corresponding factors for the $\gamma_n \to \Gamma_5$ transitions. Is seems reasonable to further hypothesize that the Franck–Condon factors of the $\gamma_n \to \Gamma'_5$, $\gamma_n \to \Gamma'_4$, and $\gamma_n \to \Gamma_1$ transitions are smaller still.

The absorption spectrum of Fe:ZnSe near 80 K is of particular interest because this is approximately the temperature of liquid nitrogen under lab conditions, which was used to cool the first Fe:ZnSe lasers. Figure 16 shows the absorption spectrum of Fe:ZnSe at 80 K. We note from this data that a pump laser in the $2700 - 3500\ nm$ range will be needed to efficiently pump the electron population into the upper state manifold of Fe:ZnSe
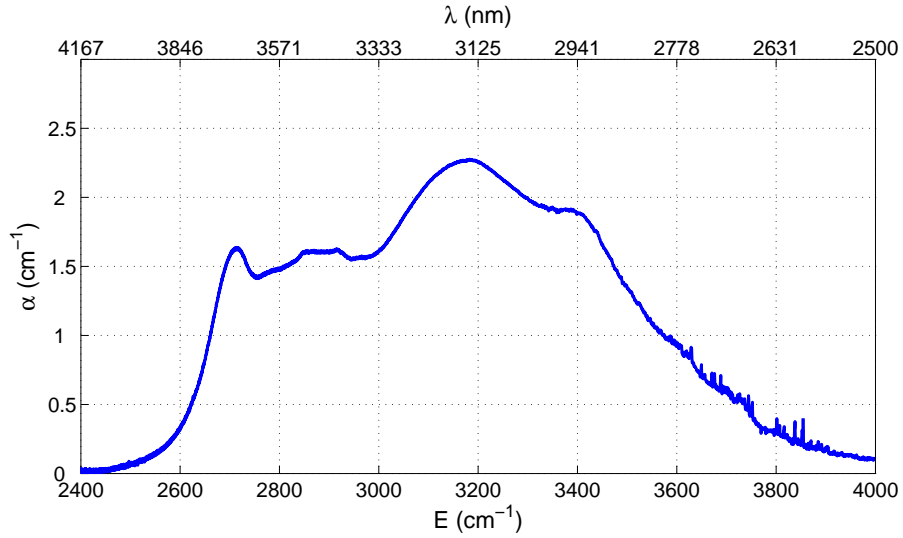
Figure 16. The absorption coefficient of Fe:ZnSe at 80 K.

In summary, we have shown that the physics considered in previous sections accurately describe the optical behavior of Fe^{2+} ions in ZnSe. We have seen that the absorption spectrum changes drastically with temperature and that pump laser sources with output wavelengths of approximately 3 μm are ideal for exciting the electron population to the T_2 upper state manifold of Fe:ZnSe. We turn now to consideration

of laser induced fluorescence studies of the upper state manifold of Fe:ZnSe.

3.2   Laser-Induced Fluorescence Spectroscoscopy of Fe:ZnSe

A *Cryo Industries of America (CIA)* cryostat was used to provide control of the temperature of a small sample of Fe:ZnSe. The CIA cryostat, like the ARS cryostat, used CaF_2 windows, which allowed transmission of mid-IR radiation. The cryostat was used in conjunction with a *Spectra-Pro 750* monochromator from *Acton Research Co.* to collect laser-induced fluorescence spectra from 5 K to 225 K. A photograph of the experimental setup is shown in Figure 17.
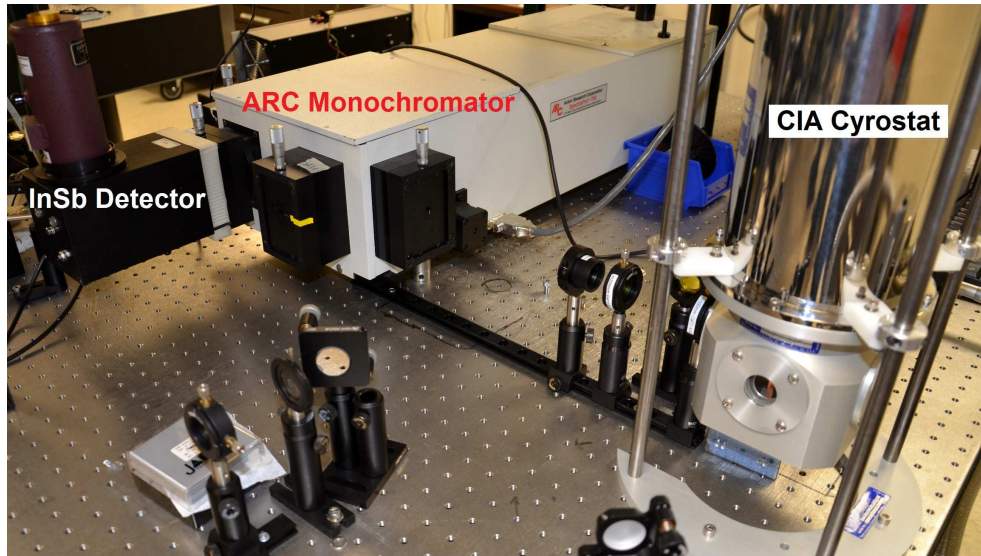
Figure 17. The *CIA* cryostat and the *ARC* monochromator.

The laser-induced fluorescence spectrum of Fe:ZnSe from 3600 to 4500 nm was recorded using the experimental setup shown in Figure 18. The pump laser operates on the 2937 nm transition of Er:YAG and was operated at approximately 200 mW. The lock-in amplifier provides a means of recovering only signals which are correlated with the pump beam chopping frequency. The Fe:ZnSe sample readily absorbs the pump light at 5 K and population pumped into the upper state manifold quickly redistributes. The Γ_4 level of the T_2 upper state manifold is separated from the Γ_5
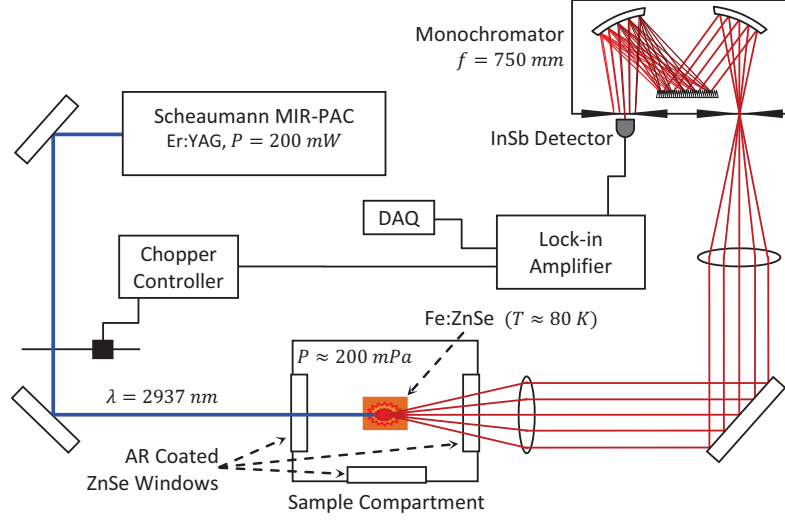
Figure 18. The experimental setup used to collect the LIF spectrum of Fe:ZnSe.

level by $2\lambda \approx 170\ cm^{-1}$. At $T = 5\ K$, $k_b T = 3.5\ cm^{-1}$. So, we see that $2\lambda \gg k_B T$, so the Γ_4 level will not be substantially populated. So, only transitions out of the Γ_5 level are expected in the emission spectrum. Figure 19 exhibits strong emission on the same line series observed in absorption: 2691, 2709, 2721, and 2931 cm^{-1}. Thus, our assignment of these transitions is seen to be self-consistent.
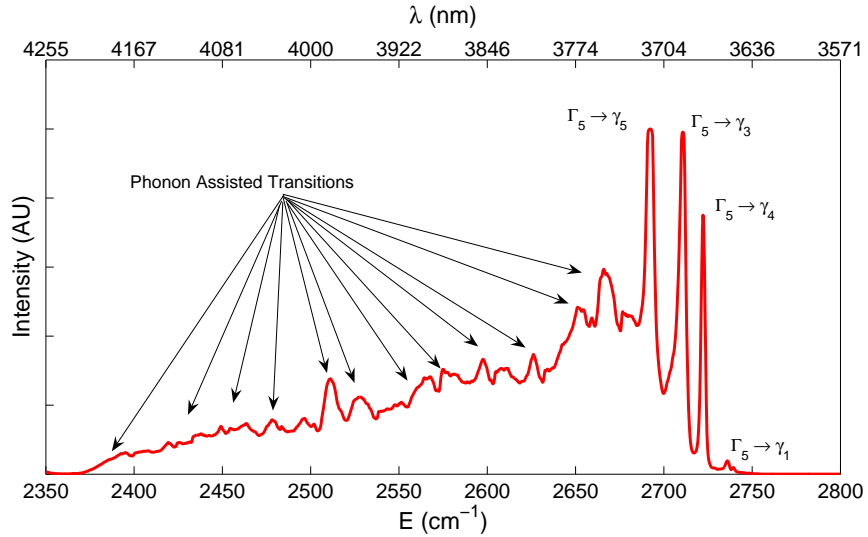
Figure 19. The laser-induced fluorescence spectrum of Fe:ZnSe at 5 K.

Historically, Fe:ZnSe lasers have been cooled by liquid nitrogen to approximately 80 K. The LIF spectrum at that temperature was recorded to provide a basis for calculation of the spectral distribution of gain. The recorded spectrum was black-body compensated to remove the effects from absorption due to atmospheric CO_2 and the spectral losses of the collecting optics. The black-body compensation technique was seen to recover the intrinsic shape of the spectral emission profile very well. The compensated spectrum was then transformed into an emission cross-section using the Füchtbauer–Ladenburg equation:

$$\sigma_{em}(\lambda) = \frac{\lambda^5 I(\lambda)}{8\pi cn^2 \tau_{rad} \int \lambda I(\lambda)\, d\lambda} \propto \frac{\lambda^5 I(\lambda)}{\int \lambda I(\lambda)\, d\lambda} \tag{3.2.1}$$

Figure 20 shows the recorded LIF spectrum and the calculated spectral gain. The observed emission spectrum resembles the familiar Pekarian envelope common to TM-doped crystals such as $Ti:Al_2O_3$ [34].
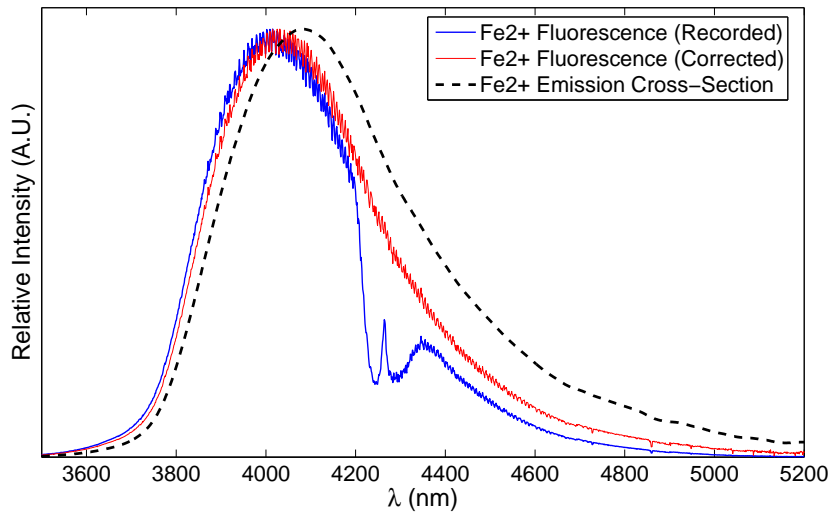
Figure 20. The recorded (blue) and corrected (red) LIF spectra of Fe:ZnSe near 80 K and its emission cross-section (black).

From the spectral gain profile, we see that laser gain will be greatest at approximately 4100 nm. This observation is consistent with the free-running CW

Fe:ZnSe laser reported by Voronov et al. [1] for which output was observed in the $4040 - 4080\ nm$ range. We also note that this fluorescence profile arises, not from emission from many optically-active velocity groups (as observed in gas lasers), but from Fe^{2+} ions occupying identical sites in the ZnSe crystal. Thus, we see that the broadening is, in some sense, homogeneous. Thus, if we suppose that the laser output can be tuned to any wavelength for which the gain is greater than half its maximum value, the laser should be capable of output from 3900 to $4400\ nm$. Indeed, in the gain switched pulse regime, lasing at $5000\ nm$ has been demonstrated [24].

Finally, temperature-dependent LIF spectra of Fe:ZnSe were recorded from $75\ K$ to $225\ K$ in increments of $25\ K$. The recorded spectra are shown in Figure 21 (without black-body compensation). The spectra recorded at $75\ K$ and $100\ K$ are very similar. However, for $T > 100\ K$, the effect of thermally activated non-radiative quenching can be clearly seen as a decrease in the fluorescence efficiency of the emitted light per solid angle. With every step increase in the temperature of the sample, the peak of the Pekarian envelope is red-shifted slightly and the intensity curve can be seen to decrease for all wavelengths.
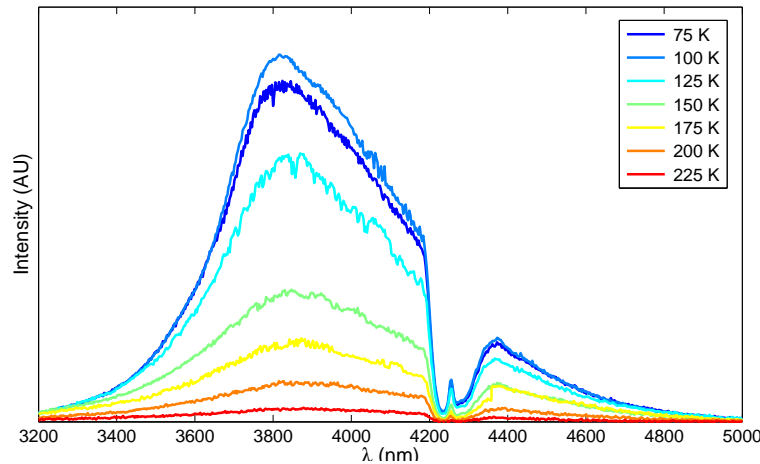
Figure 21. Temperature-dependent LIF spectra of Fe:ZnSe. The fluorescence efficiency is proportional to the integrated intensity of each curve, so we note again that the radiative efficiency drastically decreases with increasing temperature.

3.3 The Upper-State Lifetime of ZnSe

The upper-state lifetime of Fe^{2+} ions in ZnSe has been a topic of investigation for many years. However, the published literature do not agree on the value of the radiative lifetime τ of Fe^{2+} ions in ZnSe. Adams [20] reported the lifetime of this material to approach 105 μs near 100 K. This measurement is consistent with Deloach [51] and Jelínková [52] (see Figure 22). However, Myoung et al. have reported maximum values of no more than 65 μs at the same temperature [21]. Adams, Deloach, and Jelínková measured the lifetime of single-crystal samples of grown Fe:ZnSe, while Myoung reported the measurement of lifetimes of poly-crystalline ZnSe diffusion doped with Fe^{2+} ions. It is not clear, however, whether the difference in lifetime reported between these authors is attributable to this difference alone since concentration quenching is also known to affect the upper-state lifetime of TM-doped crystal gain media [53].

Figure 22. Some literature values of the upper-state lifetime of Fe^{2+} ions in ZnSe with respect to changes in temperature.

3.3.1 Measuring the Upper-State Lifetime

For the sake of comparison, we performed measurements of the upper-state lifetime of poly-crystalline Fe:ZnSe (single-crystal material was unavailable). These measurements were performed using a Q-switched Er:YAG laser from Naval Air Weapons Center (NAWC). The laser produces optical pulses at 2937 nm, which is readily absorbed by Fe:ZnSe. The accuracy of the measurement is limited by 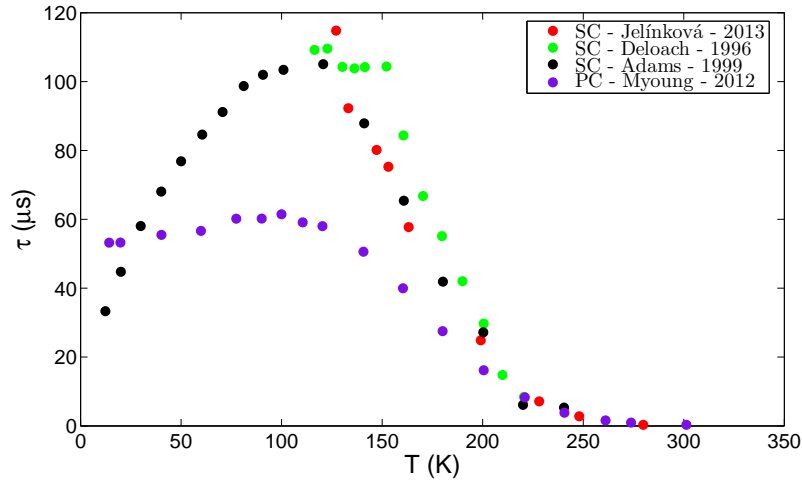the minimum pulse duration of this excitation laser. The average pulse width of the laser was approximately $200 - 300$ ns. The maximum upper-state lifetime of Fe^{2+} ions in ZnSe is on the order of tens of microseconds, so the pulse duration of this laser is more than short enough to allow us to determine the temperature at which non-radiative processes begin to reduce the upper-state lifetime.

The objective of this study was to extract the average upper-state lifetime τ of excited Fe^{2+} ions in ZnSe as a least-squares fit of $I\left(t\right) = A \exp\left(-\frac{t-t_0}{\tau}\right) + a_0$ to the pulse response of Fe:ZnSe. It should be clear that meticulous care must be taken when performing such fits since several authors have published values for τ which do not agree. In the discussion that follows, we attempt to develop algorithms that mitigate sources of systematic error in the measurement of the lifetime of excited Fe^{2+} ions in ZnSe.

Pulses from the Er:YAG laser were input to a sample of Fe:ZnSe (FE019) cooled by a pulse tube cryostat. The decay of the optical output was recorded by focusing radiative emission through an *Acton Spectra-Pro* monochromator ($f = 750$ mm) onto a liquid-nitrogen cooled InSb detector and the signal was recorded on an oscilloscope (see Figure 23). The reference signal from the Q-switch controller was used for triggering the oscilloscope.

Two-hundred data traces were collected in this way for a given sample temperature. Datasets were collected from 5 K to 300 K in this way. Figure 24 shows a

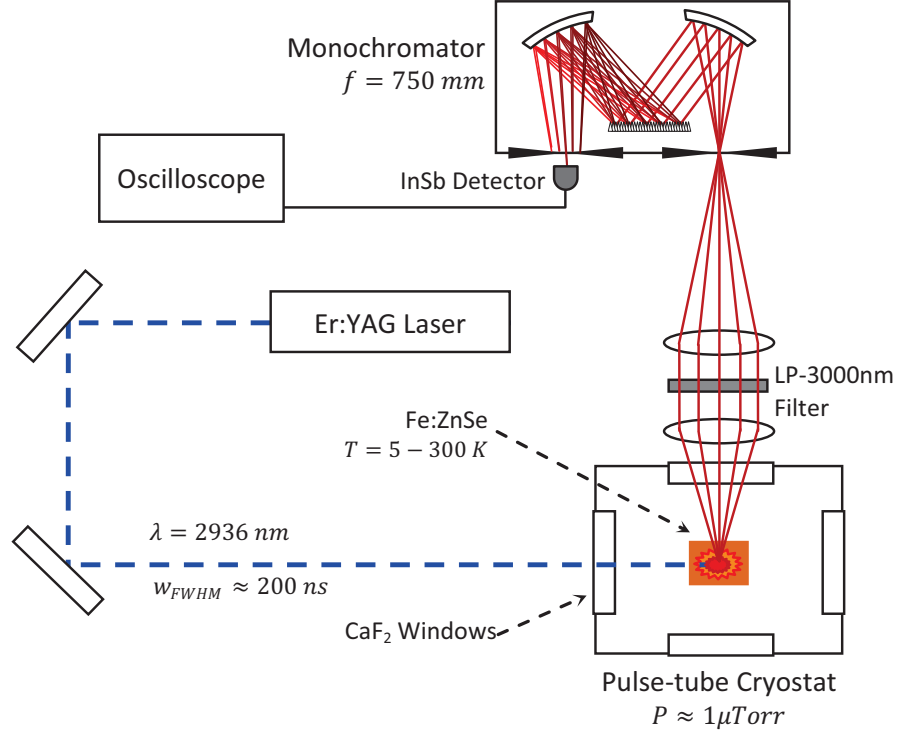**Figure 23.** **The experimental setup used to collect fluorescence decay traces.**

typical trace of the fluorescence decay of Fe:ZnSe at $5\ K$ corresponding to one shot from the Q-switched Er:YAG laser.
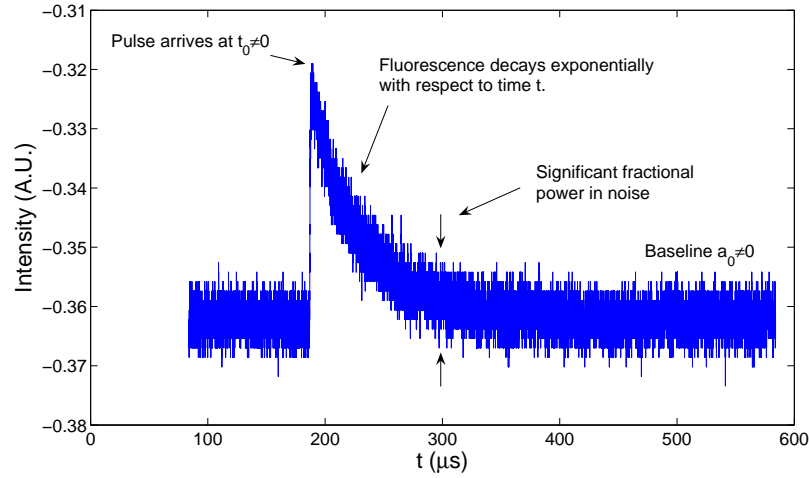
Figure 24. **The fluorescence decay response of Fe:ZnSe at 5 K to a short (FWHM = 200 ns) laser pulse at 2937 nm.**

Immediately we note some characteristics of the typical pulse response. We call

62

the pulse arrival time t_0, after which time the fluorescence signal $I(t)$ decays exponentially to the baseline voltage, which is nonzero. Note that this exponential decay is dominated by random noise.

The parallelism of the interrogated crystal presents a second source of error in this measurement of the upper-state lifetime. The Fresnel reflection of light from the polished facets of the Fe:ZnSe sample creates a small Fabry-Perot cavity (see Figure 25) with enough feedback to induce significant stimulated emission of radiation from the excited Fe^{2+} ions. The stimulated component of emission leads to an artificial shortening of the upper-state lifetime. Now, the Er:YAG excitation laser is pumped by a flashlamp and the output pulse energy exhibits a great deal of fluctuation. It should come as no surprise, then, that an increase in the energy of the excitation pulse induces a decrease in the measured lifetime.
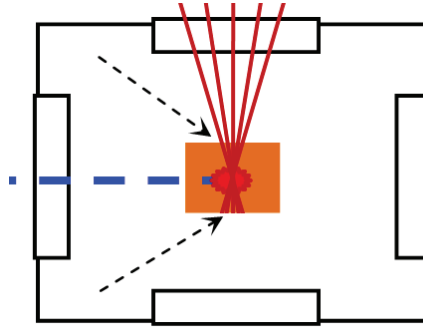
Figure 25. Fresnel reflection from the facets of the Fe:ZnSe (shown with arrows) induced stimulated emission in the sample.

Thus we see that, in the low pulse energy regime, the least-squares fit is corrupted by the effect of random noise. Consequently, the measurement was integrated over several data-traces to increase the signal-to-noise ratio (SNR), which increases proportionally to $\sqrt{n}$ where n is the number of traces accumulated. However, note that, in the high-pulse energy regime, the decay is accelerated by stimulated emission (the extracted value of τ fluctuated by more than 10% from trace to trace). Thus, the challenge of this experiment is to minimize the total error in measurement induced

by both noise and stimulated emission.

The fitting procedure begins with removing the baseline of each trace such that $a_0 \to 0$ and redefining the timescale of the trace such that t_0 becomes $t = 0$. The energy of the excitation pulse is inferred from the height A of the decay trace. The traces are then sorted by the value of A in ascending order. The traces are averaged by the addition of N traces in order from least A to greatest A. Figure 26 shows the addition of thirty traces integrated in this way [i.e $I = \Sigma_n I(N)$].
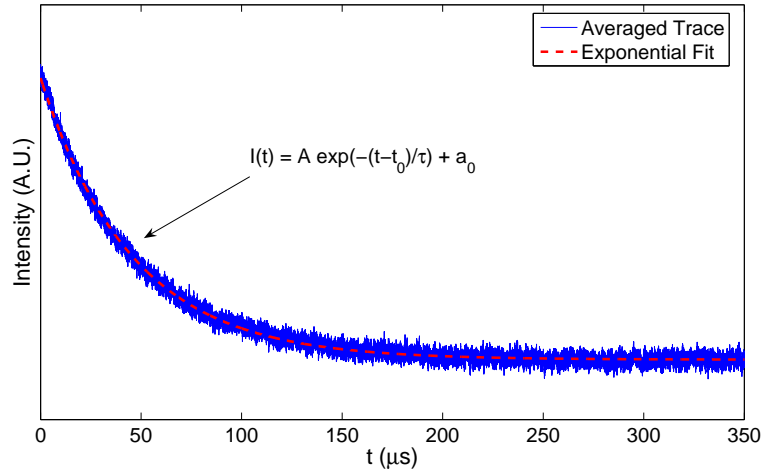
Figure 26. A summation of thirty traces of the type in Figure 24. Note the improvement in the SNR of the resulting trace.

We note the improvement in SNR (over Figure 24) that is gained from the accumulation of multiple traces. It should be clear that, for a dataset of two-hundred traces, that there is a trade-off between the improved SNR resulting from integration of additional traces and the increasingly corrupting influence of stimulated emission with the addition of traces with larger A. We note also that a single exponential fit describes the decay trace well and that a second exponential term in the fit equation is not necessary.

Figure 27 shows the estimated value of τ with respect to N. The horizontal axis corresponds to the total number of traces integrated (from least A to greatest A) and

the vertical axis corresponds to the measured lifetime τ of the combined traces. We see that for small N, the effect of noise is that τ cannot be reasonably extracted from the combined trace and the results exhibit a lot of variation. For large N, we see that the value of τ decreases due to stimulated emission effects.
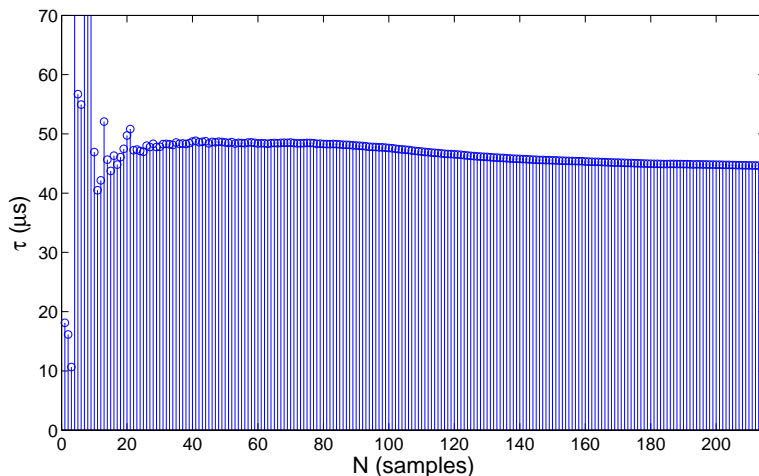
Figure 27. The fluorescence lifetime of Fe:ZnSe at 5 K as fit for summations over N traces. The horizontal axis corresponds to the total number of traces integrated and the vertical axis corresponds to the lifetime τ that best fits the combined traces.

We choose the minimum N for which the $SNR > 2$ as a metric by which to programmatically determine a value of N which provides a reasonable trade-off between noisy sources of error and systematic sources of error. The SNR is specified to be the ratio of the average power in the signal over the average power in the noise. The signal power is merely the integral of the fit function $I(t) = A \exp(-t/\tau)$. The noise power is determined as the integral over the combined trace after the fit function has been subtracted. Figure 28 shows the SNR with respect to N. For this example, the $SNR > 2$ for $N \geq 53$. Thus, by this metric, the optimal number of integrations is $N = 53$. Statistics are calculated over the window from $N - 5$ to $N + 5$ and this method returns $\tau = 48.5 \pm 0.1\,\mu s$ at $T = 5\,K$.

This algorithm was used to extract values of τ for temperatures from $5\,K$ to $305\,K$ in $15\,K$ increments. The extracted temperature-dependent behavior is consistent with
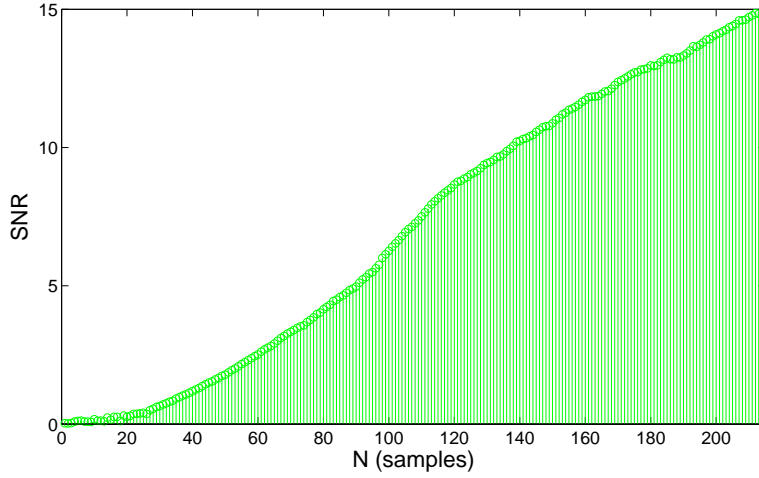
Figure 28. The SNR for an integration of the N traces with lowest A.

that observed by Myoung (see Figure 29), but not with that observed by others (see Figure 22). Thus, we hypothesize that upper-state lifetime of Fe^{2+} ions in ZnSe is determined, in part, by the choice of single-crystal or polycrystalline host material.
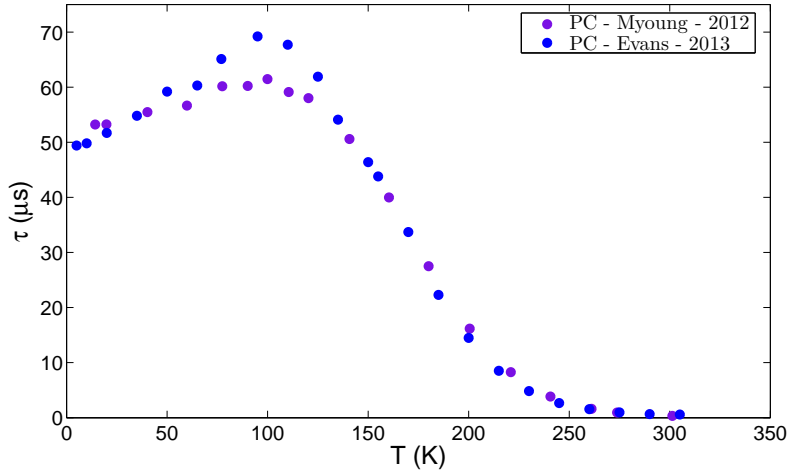
Figure 29. The measured upper-state lifetime of Fe^{2+} ions in polycrystalline ZnSe.

Additionally, the algorithm developed for extracting τ from decay traces was tested for self-consistency. Recall that, if there are not multiple groups of active ions in the sample which emit at different wavelengths, the value of the upper-state lifetime should be independent of the wavelength(s) used to measure it. So, the decay

trace of Fe:ZnSe at 5 K was recorded for the peaks of Figure 19. Table 9 shows the lifetime as measured at $\lambda = 3656, 3674, 3691, 3714, 3740, 3765, 3823, 3868, 3982,$ and $4074\ nm$.

Table 9. The measured lifetime of several transitions of Fe:ZnSe. The anomaly at 3714 nm is probably due to effects in the detector used to record the decay traces.

$\lambda\ (nm)$	$\tau\ (\mu s)$
3656	48.1 ± 0.1
3674	48.9 ± 0.1
3691	48.9 ± 0.1
3714	50.1 ± 0.1
3740	48.5 ± 0.1
3765	48.2 ± 0.2
3823	49.4 ± 0.4
3868	49.3 ± 0.2
3960	48.7 ± 0.1
3982	48.9 ± 0.2
4074	48.5 ± 0.1

From Table 9, we conclude that the metric developed for extraction of the value of τ from decay trace data is self-consistent. We also conclude that the data are consistent with a lack of multiple spectroscopic groups in the sample. Thus, we will assume the fluorescence of Fe:ZnSe is homogeneously broadened. In the next subsection, we turn from measurement of the upper-state lifetime of polycrystalline Fe:ZnSe to matching its temperature dependence with a mathematical model.

3.3.2 Modeling the Temperature-Dependent Lifetime

Myoung et al. performed a least-squares fit of their lifetime data for polycrystalline Fe:ZnSe to the standard Mott model:

$$\tau = (W_r + W_{nr})^{-1}, \tag{3.3.1}$$

where

$$W_{nr} = W_0 \exp\left(-\frac{\Delta E}{k_b T}\right). \qquad (3.3.2)$$

Their best fit for Fe:ZnSe was obtained for $W_0^{-1} = 0.1\ ns$ and $\Delta E = 2500\ cm^{-1}$. Their data is shown in Figure 30. The log scale of Figure 30 hides the fact that the dataset exhibits a gentle increase in lifetime from $\tau = 54\ \mu s$ at $T = 20\ K$ to $\tau = 62\ \mu s$ at $T = 100\ K$. The Mott expression for τ used to fit this data decreases monotonically in T, so the agreement in the region of increase from $20\ K$ to $100\ K$ is poor.
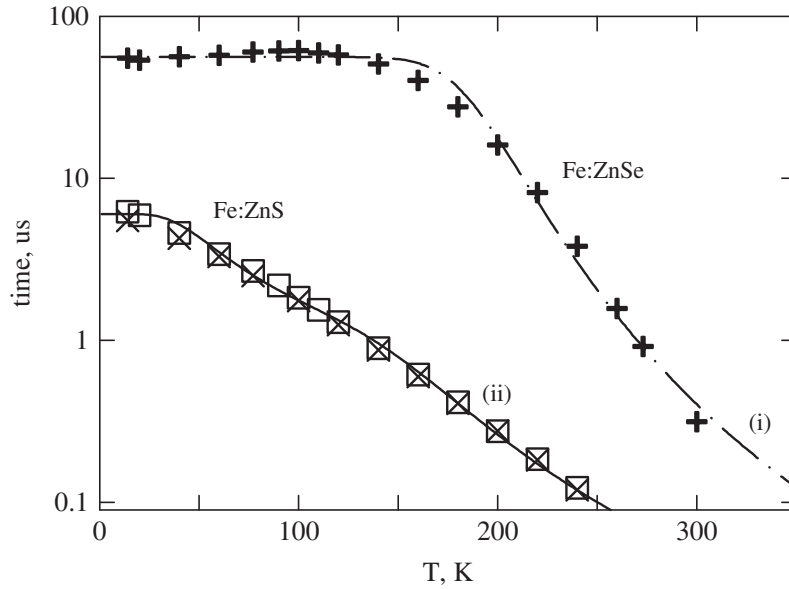
Figure 30. The fluorescence lifetime of Fe:ZnS and Fe:ZnSe from Myoung et al. [21].

The Mott model is typically used to describe the temperature dependence of the upper-state lifetime of rare-earth ions, which do not exhibit this increasing trend at low temperatures. Typically, the upper state manifolds of such ions consist of multiple energy-degenerate levels. The energy difference between these levels is small and thus thermal statistics can be neglected. However, for Fe^{2+} ions in II–VI semiconductors,

the energy levels of the T_2 manifold are split as described in Section 2.4. Thus the energy differences between such levels are not small compared to the energy separation Δ between the T_2 and E manifolds. Thus thermal statistics cannot be neglected.

We know that the upper state manifold of the Fe^{2+} ion in ZnSe contains fifteen such levels. The average lifetime of this manifold is related to the lifetime of each state

$$\tau_{rad} = \left(\sum_{i=1}^{15} \tau_i^{-1} \right)^{-1}. \qquad (3.3.3)$$

Alternatively, we can treat the T_2 manifold as consisting of two energy meta-levels for simplicity. The first meta-level includes the three Γ_5 levels, and the other meta-level includes the other twelve energy levels belonging to Γ_4, Γ_3, Γ_5', Γ_4', and Γ_1. Thus the expression for the radiative lifetime becomes

$$\tau_{rad} = \left(\tau_{\Gamma_5} + \sum_{i=4}^{15} \tau_i^{-1} \right)^{-1} = \left(\tau_{\Gamma_5}^{-1} + \tau_{\bigstar}^{-1} \right)^{-1}, \qquad (3.3.4)$$

where τ_{Γ_5} is the radiative lifetime of the lowest Γ_5 states and $\tau_{\bigstar}$ is the aggregate lifetime of the remaining twelve states. Now, we add the effect of nonradiative quenching to this expression; so,

$$\tau_{rad} = \left(\tau_{\Gamma_5}^{-1} + \tau_{\bigstar}^{-1} + W_{nr}^{(p)} \right)^{-1}, \qquad (3.3.5)$$

where

$$W_{nr}^{(p)} = \frac{A}{M^2 \sqrt{2\pi p}} \left(\frac{Se}{p} \right)^{p-2} \left(1 + \frac{1}{\exp\left(\frac{\hbar \omega_{eff}}{k_b T} \right) - 1} \right)^p, \qquad (3.3.6)$$

and where k_b is Boltzmann's constant, e is Euler's constant, A/M^2 is an effective

coupling constant for the nonradiative term, and $\hbar\omega_{eff} = E/p$ is the per phonon energy required for p phonons to bridge the energy gap E between the energy levels involved in the optical transition. We further note that

$$\frac{N}{\tau_{rad}} = \frac{n_{\Gamma_5}}{\tau_{\Gamma_5}} + \frac{n_{\bigstar}}{\tau_{\bigstar}}, \tag{3.3.7}$$

where the total population is $N = n_{\Gamma_5} + n_{\bigstar}$. We introduce thermal statistics by noting that the fractional population is

$$\frac{n_{\bigstar}}{n_{\Gamma_5}} = \frac{g_{\bigstar}}{g_{\Gamma_5}} \exp\left(-\frac{\Delta E_{T_2}}{k_b T}\right), \tag{3.3.8}$$

where $g_{\Gamma_5} = 3$ and $g_{\bigstar} = 12$ are the degeneracy factors, and where ΔE_{T_2} is the separation of the two meta-levels. Using this approach we can construct a model for the upper-state lifetime that includes nonradiative quenching and thermal statistics:

$$\tau_{total}^{-1} = \frac{\tau_{\Gamma_5}^{-1}}{1 + \frac{g_{\bigstar}}{g_{\Gamma_5}} \exp\left(\frac{-\Delta E_{T_2}}{k_b T}\right)} + \frac{\tau_{\bigstar}^{-1}}{1 + \frac{g_{\Gamma_5}}{g_{\bigstar}} \exp\left(\frac{\Delta E_{T_2}}{k_b T}\right)}$$
$$+ \frac{A}{M^2\sqrt{2\pi p}} \left(\frac{Se}{p}\right)^{p-2} \left(1 + \frac{1}{\exp\left(\frac{\hbar\omega_{eff}}{k_b T}\right) - 1}\right)^{p} \tag{3.3.9}$$

We eliminated ω_{eff} as a fit parameter by recasting it in terms of p and using the approximation that $E \approx \Delta = 10Dq$. Thus, $\omega_{eff} = \Delta/p$. Thus, this model includes six fit parameters: A/M^2, τ_{Γ_5}, $\tau_{\bigstar}$, ΔE_{T_2}, S, and p.

The fit of this model to the temperature-dependent lifetime data for Fe:ZnSe was performed using the NonlinearModelFit[] command in *Mathematica*. Experience has shown that this model will not converge to match the provided dataset unless the user also provides a good set of initial guess values for the fit parameters. From the low temperature limit of the dataset of Myoung et al., we chose 54 μs as the initial

value of τ_{Γ_5}. The data of Hennion et al. suggested a value of $E_{ph} = 225 \; cm^{-1}$ for the average energy of a longitudinal phonon, so we used $p = \Delta/E_{ph} \approx 13$ as an initial value. Henderson and Imbusch state that the Huang–Rhys parameter S of transition metals can vary by more than one order of magnitude about unity, so we chose $S \approx 5$ as an initial value. We used $\Delta E_{T_2} = |\lambda| = 82.3 \; cm^{-1}$ (where λ is the SO parameter, not wavelength) as an initial value of ΔE_{T_2}. We chose $\tau_\star = 100 \; \mu s$ as an initial value since $\tau_\star$ must be greater than τ_{Γ_5} to produce an increase in τ_{rad} with respect to T. We arbitrarily used $A/M^2 = .01 \; \mu s$ as an initial value as well.

The modeled values of these parameters as fit to the data of Myoung et al. and to the data collected in this work are shown in Table 10. We note that the uncertainty in each parameter is generally small with respect to the value of the parameter itself. We also note that most of the fit parameters take similar values in the fit of both datasets. However, the A/M^2 parameter varies by more than a factor of three and the $\tau_\star$ parameter varies by almost a factor of two between the two columns. It is not clear at this time what sources of error may have produced these variations.

Table 10. The returned values of the fit parameters for our model of the temperature-dependent fluorescence lifetime of Fe^{2+} ions in ZnSe.

Parameter	Myoung et al.	This Work
$A/M^2 \; (\mu s)$	0.017 ± 0.001	0.0047 ± 0.0004
$\tau_{\Gamma_5} \; (\mu s)$	54.7 ± 0.6	52 ± 1.0
$\tau_\star \; (\mu s)$	79 ± 3.5	132 ± 22.4
$\Delta E_{T_2} \; (cm^{-1})$	98 ± 10.8	91 ± 9.3
S	5.237	5.776
p	16.1 ± 0.25	15.5 ± 0.5

Figure 31 shows the fit of this model to these two datasets. The 90% confidence interval is narrow in both cases and the gradual increase of the radiative lifetime at low temperatures is accommodated. Thus it is reasonable to conclude that the increase in radiative lifetime with increasing temperatures for $T < 100 \; K$ is due to the splitting of the upper state manifold with $\tau_\star > \tau_{\Gamma_5}$. We also see that, for

polycrystalline Fe:ZnSe, non-radiative quenching counteracts this increase and leads to a decreasing trend in total lifetime with temperature above $100\ K$. Thus we see that NRQ is the chief relaxation mechanism prohibiting sustained room-temperature laser oscillation.
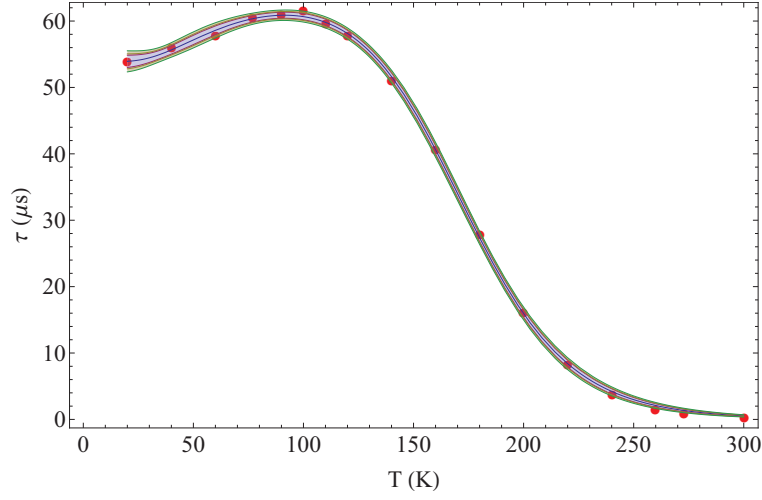
(a) Myoung et al.
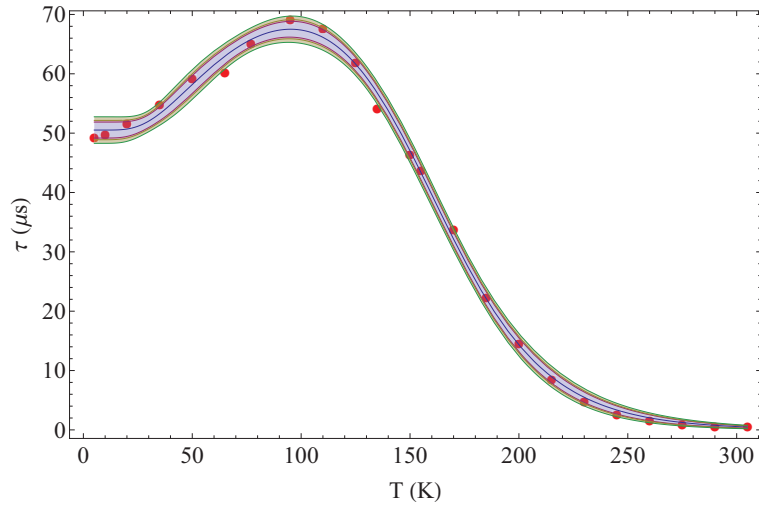
(b) This Work

Figure 31. A numerical fit of Equation 3.3.9 to the lifetime data for polycrystalline Fe:ZnSe. Colored bands show the 90% confidence interval(s).

3.4 Conclusions and Future Work

We have accomplished several notable objectives in the work discussed in Chapters I and II. We have

1. discussed the physical interactions governing the behavior of Fe^{2+} ions in ZnSe in detail,

2. presented approximate expressions for the 11 unique eigenvalues Fe^{2+} ions in ZnSe and the corresponding degeneracies,

3. constructed a model of the low-temperature absorption spectrum of Fe:ZnSe,

4. presented the measured absorption spectra of Fe:ZnSe from 10 K to 300 K and confirmed the utility of the previously mentioned model,

5. presented the measured laser-induced fluorescence spectra of Fe:ZnSe at 5 K and from 80 K to 225 K,

6. presented a temperature-dependent measurement of the upper-state lifetime and discussed its correlation to published work,

7. developed a model of the temperature dependence of the upper-state lifetime and fit it to measured values.

We have shown conclusively though spectroscopic experiments that the theory developed over the past five decades (with the inclusion of our own additions) describes the optical behavior of Fe^{2+} ions in ZnSe. We have directly observed and correctly modeled the temperature-dependence of the upper-state lifetime of Fe^{2+} ions in ZnSe. From our investigation, we can conclude that thermally activated multi-phonon transitions are the cause of NRQ in Fe:ZnSe. Our model, modified from the work of Henderson, Dexter, Miyakawa, and others, indicates that the most straightforward

way to mitigate these effects is to increase the mass of the atoms of the host crystal. Thus, we recommend careful spectroscopic investigation of Fe^{2+}-doped XxTe, CdXx, HgXx, and their alloys. We have begun that investigation, though the work is incomplete as of this writing. We also recommend the investigation of single crystal Fe:ZnSe along with polycrystalline material. It must be verified, whether others who have published values of the lifetime of Fe^{2+}-doped single crystal ZnSe have committed consistent systematic errors, or if the differences are intrinsic. We also propose spectroscopic investigation of concentration quenching of the fluorescence of Fe:ZnSe, which has not been discussed or explored in this work, but is a topic of great interest to those who study Fe^{2+}-doped II–VI lasers. We now turn from a broad overview of the optical physics governing the behavior of Fe^{2+} ions in ZnSe, to demonstrations of lasers using Fe:ZnSe as a gain medium.

IV. Continuous-Wave Fe:ZnSe Lasers

Solid-state infrared lasers are of interest for many applications including remote sensing, laser radar, IRCM, infrared laser spectroscopy, and for other military, scientific and commercial purposes. Yet few direct laser sources operate in the $3-5\ \mu m$ atmospheric transmission window. High-power lasing has been demonstrated in the $2-3\ \mu m$ waveband from Cr^{2+} ions doped into various II–VI crystal hosts [51], most notably ZnSe [54] and ZnS [55]. These lasers are capable of tens of watts of CW output power [15], are broadly tunable [54, 55], and can achieve high peak powers via Q-switched or modelocked operation [12]. Fe^{2+} and Cr^{2+} ions have complimentary electronic configurations and thus exhibit similar spectroscopic properties. However, Fe^{2+} ions experience a smaller crystal field splitting in II–VI hosts than Cr^{2+} ions do. Consequently, the optical emission of Fe:ZnSe is greatest from 3.5 to 5 μm making this material a promising candidate for a high-power tunable laser in the mid-IR region.

In this chapter, we report the demonstration of high-power (840 mW) continuous-wave (CW) laser oscillation from Fe^{2+} ions in zinc selenide in detail. The output spectrum of the Fe:ZnSe laser had a line-center near 4140 nm with a linewidth of 80 nm. The beam quality was measured to be $M^2 \leq 1.2$ with a maximum slope efficiency of 47%. Small shifts that were observed in output wavelength with increased input power were attributed to thermal effects. No thermal roll-off of slope-efficiency was observed at the maximum of output power. Broadband wavelength tuning of an Fe:ZnSe laser is demonstrated using spectrally selective intracavity optics. Additionally, several resonator configurations were briefly tested with the significant result that $> 1\ W$ power was achieved near 4100 nm.

4.1 Experimental Setup

For this work, we employed a poly-crystalline ZnSe sample which was diffusion-doped with Fe^{2+} ions to a concentration of approximately $9 \times 10^{18}\ cm^{-3}$ as reported by the vendor [56]. As discussed in detail in Section 3.1, Fe:ZnSe exhibits a broadband absorption feature with a local maximum at $\lambda \approx 3100\ nm$ from $T \approx 40\ K$ to $300\ K$ (see Figure 13). This absorption band can be pumped using the $\lambda = 2937\ nm$ Er^{3+}:YAG laser transition. We pumped the Fe:ZnSe laser cavity from each end with a *Sheaumann Laser MIR-PAC* DPSS laser. The maximum CW output power of each laser was $1.5\ W$; thus, a maximum of $3\ W$ of total pump power was available at $2937\ nm$.

As shown in Figure 32, we constructed a concentric laser cavity with an overall length of $100\ mm$ between end mirrors $M1$ and $M2$, each with a $50\ mm$ radius of curvatures. $M2$ also functioned as an outcoupler with $R \approx 70\%$ from 3000 to $5000\ nm$. The pump beams each exhibited $M^2 \leq 2$ and each beam was collimated using lenses $L1$ and $L2$ as shown. Each collimated pump beam was focused through a cavity mirror and into the center of the Fe:ZnSe sample. We used two $f = 150\ mm$ lenses $L3$ and $L4$ to obtain beamwaist diameters of $110\ \mu m$. The sample was $2\ mm \times 6\ mm \times 8\ mm$ and its two smallest facets were broadband AR coated from 2900 to $5000\ nm$. The sample was affixed to a copper mount cooled to $\sim 77\ K$ by liquid nitrogen (see Figure 33). The sample compartment was evacuated to $\sim 200\ mPa$ and the windows $W1$ and $W2$ were AR-coated from 2900 to $5000\ nm$. The linear geometry of the laser cavity made it necessary to separate the output beam from the pump beam using a dichroic mirror $M3$, which exhibited $R > 97\%$ from 3000 to $5000\ nm$.
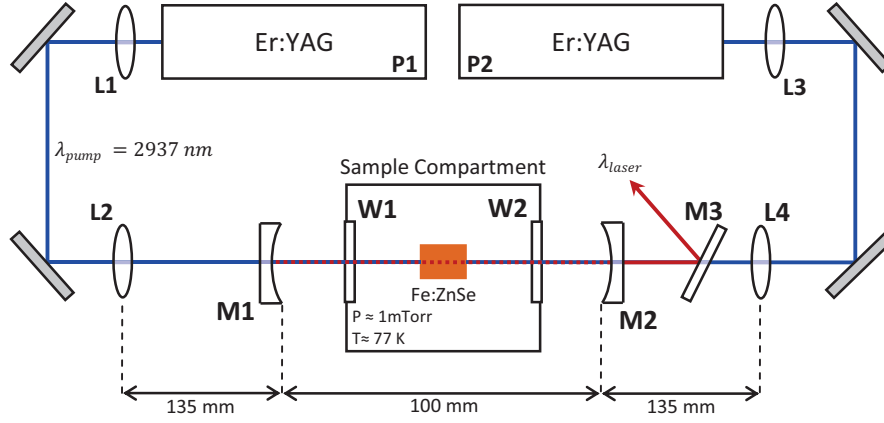
Figure 32. A schematic view of the Fe:ZnSe laser. All optics are made of CaF$_2$ and anti-reflection coated at 2937 nm unless otherwise noted.
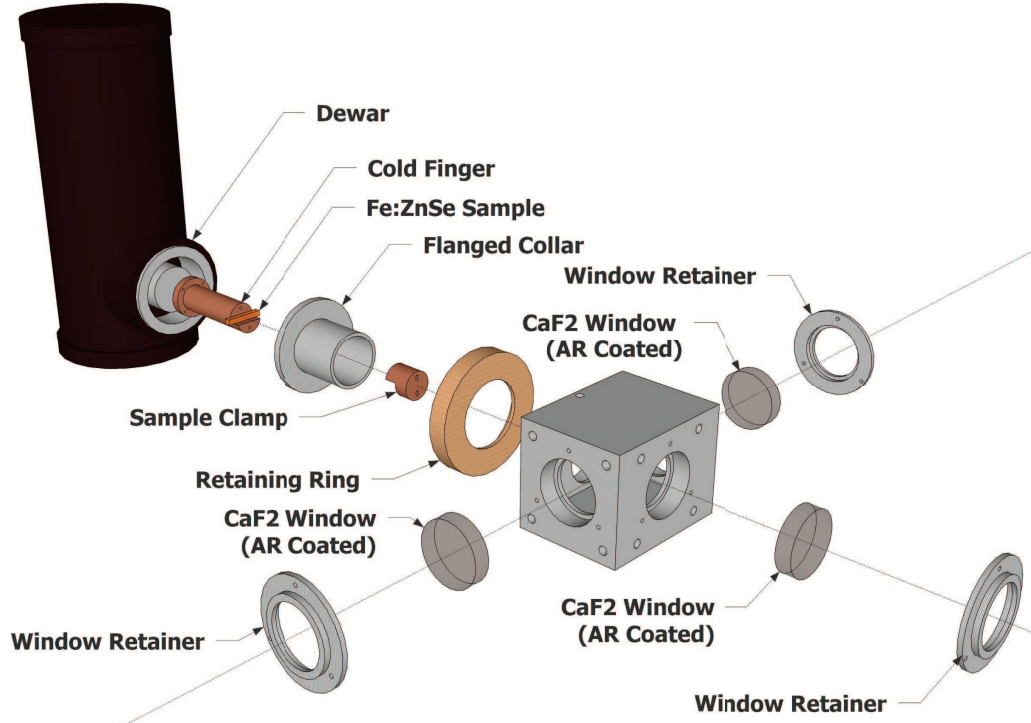
Figure 33. A breakout view of the sample compartment.

4.2   Power Scaling

Together, $L1$, $L2$, and $M1$ transmitted only 81% of the power from $P1$. The threshold of lasing was 150 mW and the ratio of transmitted power to output power showed 37% slope efficiency (see Figure 34). The combination of $L3$, $L4$, $M3$, and $M2$

transmitted only 64% of the power from $P2$. Thus, with both pump beams operating at full power, only 2.17 W of pump power was coupled into the cavity. The slope efficiency of the laser with respect to $P2$ was measured to be 47% with $P1$ operating at full power. With both pump lasers at full-power, the maximum output of the laser was $847 \pm 12 \ mW$.
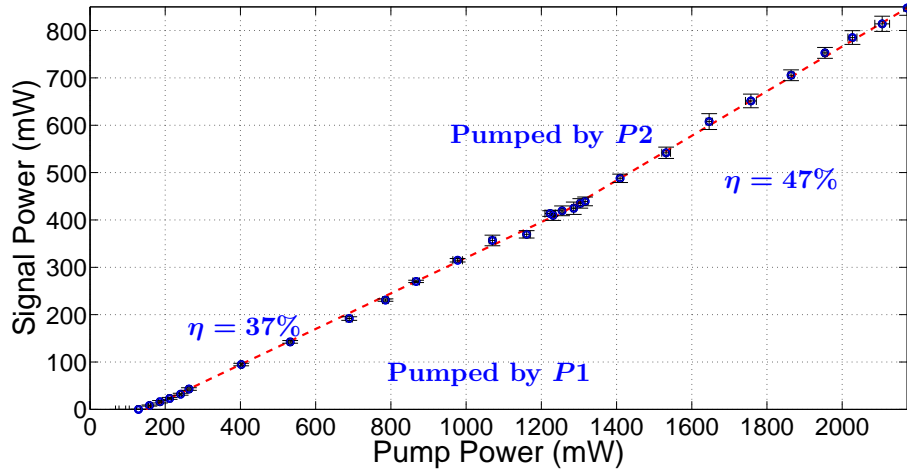
Figure 34. The slope efficiency plot of the Fe:ZnSe laser relative to incident power. Error bars correspond to $\pm \sigma/2$.

The values of input power shown on Figure 34 are direct measurements of the power incident on $W1$ or $W2$. From direct measurement of the transmission and reflection of $M3$ at the pump wavelength, we were able to determine that $< 1 \ mW$ of the power measured in reflection from $M3$ can be attributed to content at 2937 nm. We note that for all data points of Figure 34 this correction is less than the measurement uncertainty of the output power and so it has been neglected.

From Figure 34, we see that the slope efficiency of the laser relative to the $P2$ beam was significantly higher than that of the $P1$ pump beam. This is most likely due to non-optimal pump-mode overlap, which is difficult to control in this cavity configuration. $M1$ can be adjusted to control the mode volume, but this adjustment also changes the focal spot size and location of the pump beam. In Section 4.6, we

explore the use of folded cavity geometries to give independet control over the pump and mode volume. The laser increased with nearly-optimal slope efficiency relative to $P2$. Recall that the maximum efficiency of the laser is limited by the absorption efficiency $\eta_{abs} = (1 - \exp{(-\alpha l)})$ and the quantum efficiency $\eta_q = \lambda_{pump}/\lambda_{laser}$. For this laser

$$
\begin{aligned}
\eta_{limit} &= \eta_{abs} \cdot \eta_q \\
&= (1 - \exp{(-\alpha l)}) \frac{\lambda_{pump}}{\lambda_{laser}} \\
&= \left(1 - \exp{\left(-1.6 \ cm^{-1} \cdot 8 \ mm\right)}\right) \frac{2937 \ nm}{4140 \ nm} \\
&= 51.2\%.
\end{aligned}
\tag{4.2.1}
$$

So we see that a 47% slope efficiency value approaches the calculated limit of efficiency. The gap between the ideal limit and the recorded performance is likely due to additional losses such as surface scattering and parasitic processes in the laser, which we have not characterized.

The lack of thermal roll-off in Figure 34 suggests that thermal lensing in the crystal is weak. We used the method of Schepler et al. [57] to calculate a maximum thermal lens power of 16 m^{-1} at full power. We constructed a model of the laser cavity including all the beam parameters reported in this work. With this model, we calculated the $1/e^2$ beamwaist diameter of the resonant mode to be 265 μm at the center of the crystal in the absence of thermal lensing and to be $< 300 \ \mu m$ when thermal lensing effects were considered.

4.3   Beam Quality

To measure the beam quality of the Fe:ZnSe laser, the output beam was focused using a 100 mm lens. The $1/e^2$ radius $w(z)$ of the focused beam was measured at evenly spaced locations along the optic axis using a *Photon Inc. Nanoscan* scanning slit beam profiler. The beam quality M^2 and the beamwaist radius w_0 were

determined as parameters of a least squares fit of the beam width data to

$$w(z) = w_0 \cdot \sqrt{1 + M^2 \left(\frac{z}{z_R}\right)^2}, \qquad (4.3.1)$$

where z_R is the Rayleigh range of the beam, w_0 is the beamwaist radius and the zero of z is defined at the beamwaist. Figure 35 shows the profile of the output beam. When pumping with $P1$ at full power and $P2$ off we measured $M_T^2 = 1.14$ and $M_S^2 = 1.09$. When pumping with both $P1$ and $P2$ at full power we measured $M_T^2 = 1.08$ and $M_S^2 = 1.13$.
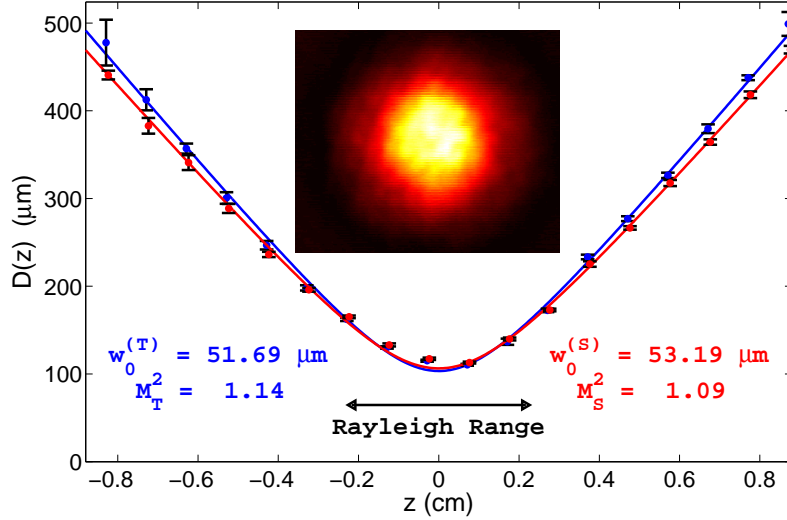
Figure 35. The beam profile of the Fe:ZnSe laser operating at full power. The inset is a picture of the beam as recorded by an *Electrophysics PV320* beamprofiling camera.

4.4 Spectral Content

The laser output at full power was spectrally resolved using an *Acton SpectraPro-750* monochromator. The instrument utilized a 300 *groove/mm* grating blazed at $3\,\mu m$. The real-time ($\sim 50\,Hz$) spectrum of the laser was recorded using a *CalSensors* PbSe linear detector array at the output port of the monochromator. The observed spectrum indicated that the laser operated on many longitudinal modes of the cavity

simultaneously. The relative amplitude of each line fluctuated rapidly, consistent with mode-hopping.

The PbSe array was replaced with a liquid nitrogen cooled InSb detector and the slit widths were set to 10 μm to give the instrument a spectral resolution of $< 0.5\ nm$. Datasets of 15 samples each were collected in 1 nm intervals using a lock-in amplifier with an integration time of 300 ms. The output spectrum of Figure 36 shows the average value of each interval.
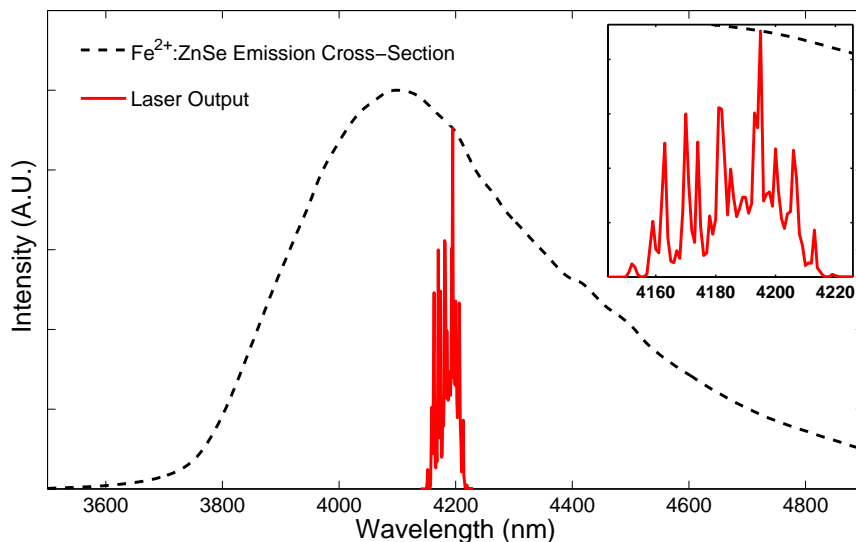
Figure 36. The normalized emission spectrum of the Fe:ZnSe laser operating at full power. The black dotted line is the normalized emission cross-section at $\sim$ 80 K as calculated from a system-compensated emission spectrum and the Füchtbauer–Ladenburg equation. The structure in the output is hypothesized to be due to mode-hopping. The inset shows the lasing region in greater detail.

We observed the output spectrum of the laser to be slightly dependent on the output power. The time-averaged spectral centroid of the laser output trends toward longer wavelengths with increasing output power as shown in Figure 37. The time-averaged spectral width of the laser output was $60 - 80\ nm$ and was observed to be independent of output power.

We attribute this shift in the spectral content of the laser output to an increase in temperature at the focus of the pump laser. This localized heating of the crystal
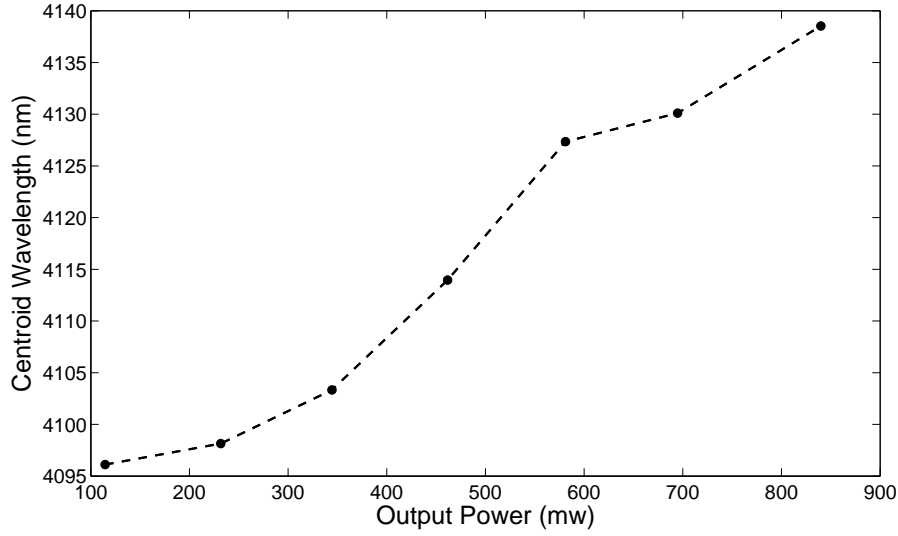
Figure 37. The spectral centroid position plotted against the output power of the Fe:ZnSe laser.

changes the distribution of population within the upper state manifold of the lasing ion. This change preferentially increases the probability of re-absorption of the shorter-wavelength photons emitted from the broad energy levels of the Fe^{2+} ion and shifts the peak gain of the material to longer wavelengths.

We support our claim that the red-shift is due to thermal effects by comparing the output spectrum of the free-running Fe:ZnSe laser to the output spectrum of the laser recorded when $P1$ was chopped at 200 Hz with a 50% duty-cycle. With $P2$ off, we observed that the time-averaged spectral centroid of the laser output decreased by ~ 12 nm when $P1$ was chopped. This observation is consistent with Figure 37, and suggests that the red-shifts follow changes in average pump power, not peak pump power. Thus, we conclude that the observed red-shifts are due to thermal effects within the crystal and not to intensity-dependent dynamics of the Fe^{2+} ions.

We observed that using a different ZnSe sample with a lower quoted concentration of Fe^{2+} ions resulted in a shift of the spectral centroid of the laser output toward the blue by tens of nanometers. This effect is due to a decrease in re-absorption of emitted

photons at shorter wavelengths. It is not clear whether the preferential decrease in re-absorption is a direct consequence of reducing the concentration or an indirect consequence of thermal effects due to decreased absorption of pump power.

4.5 Tuning the Output Wavelength

Tuning of the laser output was accomplished by inserting a tuning element T into the laser cavity to introduce losses at the peak of emission. This crude method of tuning was used because using dispersive techniques would have required significant reconfiguration of the cavity, which was undesirable. Because these elements tended to absorb the 2937 nm pump beam, the single-pump configuration of Figure 38 was used to compare the power output of the laser when it operated at several different output wavelengths. The pump $P1$ was operated at full-power. Each filter introduced a change to the optical path of the mode, so the alignment of cavity mirrors $M1$ and $M2$ was adjusted slightly to maximize the output of the laser before average power readings and emission spectra were recorded.
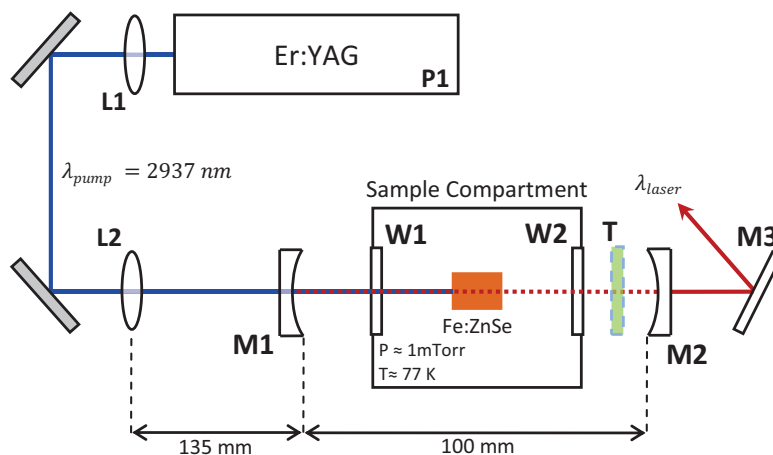

Figure 38. A schematic view of the Fe:ZnSe laser. All optics were made of CaF$_2$ and anti-reflection coated at 2937 nm unless otherwise noted. The dashed element T was inserted into the basic cavity to tune the output. The transmission spectra of M1 and M2 were essentially flat in the fluorescence band of Fe:ZnSe.

The output spectrum of the laser was recorded using a liquid nitrogen cooled InSb detector attached to an *Acton Spectra–Pro 750* monochromator with the slit widths set to 10 μm to give the instrument a spectral resolution of < 0.5 nm. Datasets of 15 samples each were collected in 1 nm intervals with an integration time of 300 ms. The output spectra reported in this work show the average value of each such interval.

The output of the laser was measured in reflection from $M3$. The reflection of the dichroic mirror $M3$ was measured to be $R > 97\%$ from 3000 to 5000 nm, so the losses due to $M3$ were not strongly spectrally dependent. Thus, measured output powers at different wavelengths can be directly compared and the recorded emission spectra are characteristic of the laser output. Not surprisingly, the free-running laser (with no tuning element) exhibited the greatest power output. Optimization of the geometry of the cavity yielded 460 mW of output at 4127 nm. Figure 39 shows the power output and emission spectra of the laser when operated with several tuning elements. Note that the laser emission is red-shifted slightly from the peak of the emission cross-section. We hypothesize that this is because the long-wavelength tail of the absorption band of Fe:ZnSe overlaps with the short-wavelength tail of its emission band. This overlap causes short-wavelength components of fluorescence to be reabsorbed and thus the spectral peak of gain is shifted toward longer wavelengths.

The shortest lasing wavelength achieved was 3843 nm and the longest was 4337 nm. Thus, we demonstrated that CW lasing is possible over a range of nearly 500 nm. In principle, the laser should be capable of continuous tuning between these wavelengths using a birefringent filter or a blazed grating as a tuning element. The fact that the laser output was only reduced to about 200 mW at these wavelengths suggests that tuning beyond these wavelengths is also possible. The center right cell of Figure 39 shows that insertion of the 3900 nm short pass filter produced simultaneous lasing of two lines. Content longer than 3900 nm was not expected due to the cutoff
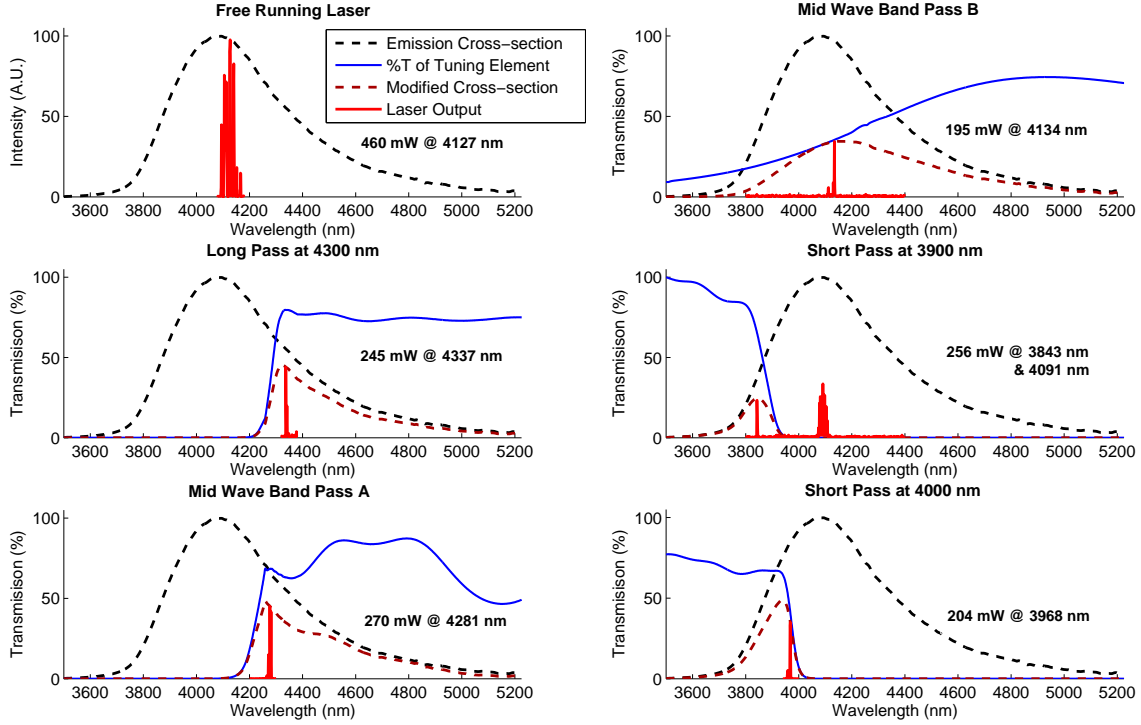
Figure 39. The lasing spectra and output powers as achieved using intracavity tuning elements. The vertical axes are arbitrary. The emission cross-section was calculated from a system-compensated fluorescence spectrum of Fe:ZnSe at ~ 80 K using the Füchtbauer–Ladenburg equation. The modified cross-sections were calculated as the product of this cross-section and the transmission spectrum of the tuning element. The transmission of the windows W1 and W2 and the reflection of mirrors M1, M2, and M3 were not included in the calculation of the modified cross-sections because each was spectral flat to within a few percent in this region.

of the short pass filter. Thus, the presence of output at 4091 *nm* requires further investigation.

We intend to demonstrate dispersive tuning of the CW Fe:ZnSe laser using a dispersive tuning element. This will require reconfiguration of the laser cavity to be compatible with the commonly used Littrow configuration. Success of this laser architecture with CW Cr:ZnSe lasers as well as the demonstration of widely tunable output from Fe:ZnSe compels us to believe that this technique will allow us to demonstrate continuous tuning of the output wavelength of a CW Fe:ZnSe laser.

4.6 Other Architectures

The linear geometry of the resonator shown in Figure 32 imposed the constraint that the cavity mode size could not be adjusted independently of the cavity focus. This constraint made the pump spot size difficult to control. We pursued a nonlinear cavity design with flat incouplers to decouple the pump focusing dynamics from the cavity mode adjustments. However, given the size of our sample compartment, it would have been necessary to change the radius of curvature (ROC) of the end mirrors to 100 mm, which would increase the cavity mode size, which was undesirable because of the low concentration of Fe^{2+} ions in our sample of Fe:ZnSe. Thus, the sample compartment was redesigned to be short enough to accommodate a folded cavity with an overall path length ~ 100 mm (see Figure 40). Thus, we constructed a U-shaped cavity as shown in Figure 41.
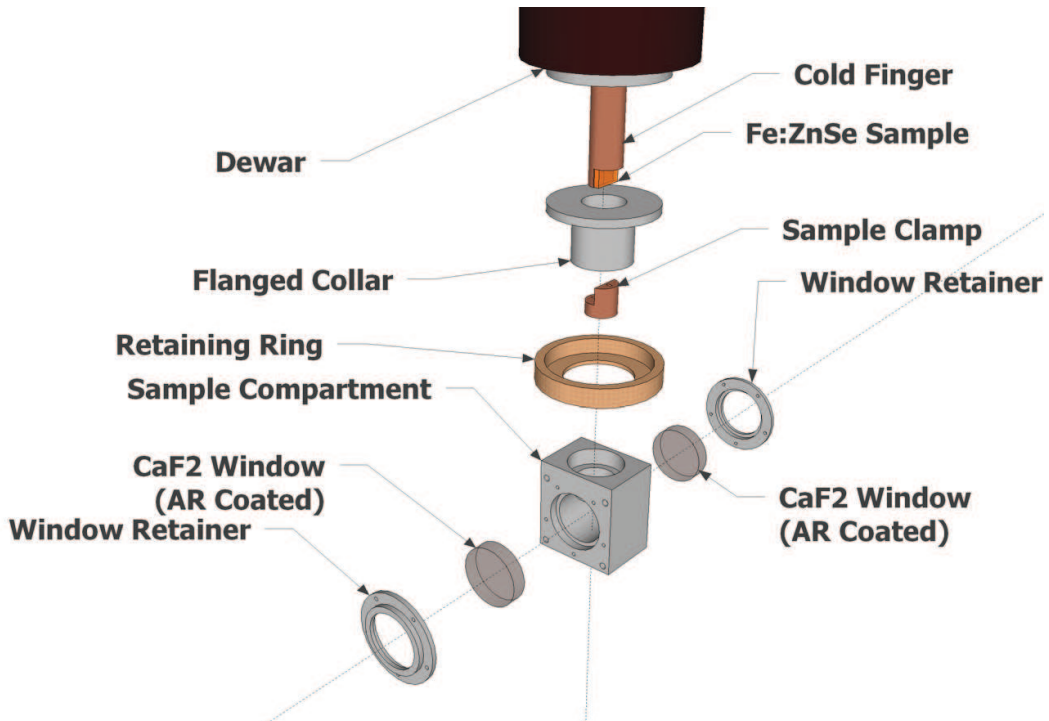
Figure 40. A breakout view of the revised sample compartment.
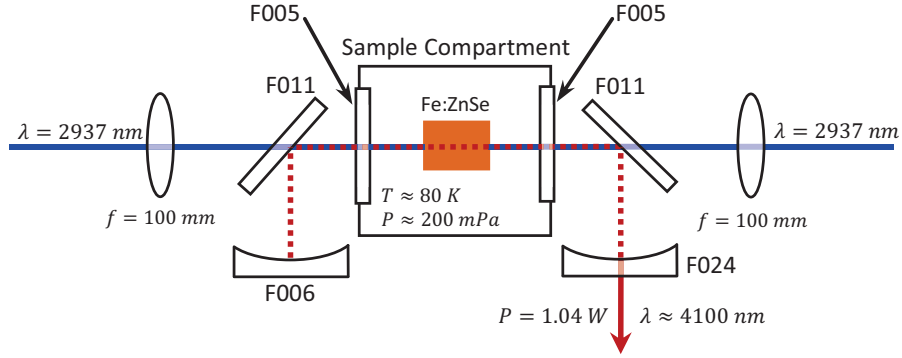
Figure 41. A U-cavity design for a CW Fe:ZnSe laser. Note that the smaller sample compartment permits the addition of turning mirrors.

The redesigned cavity configuration permitted the use of incoupling mirrors which did not have to function as outcoupling mirrors. Thus the coating for the incoupler coating design was redesigned and the incoupling efficiency was improved. Thus, in addition to finer control of the pump focal spot size, we also increased the overall available pump power. Once the cavity was optimized, the laser was shown to output 1.04 ± 0.02 W with both pump lasers operating at full power. This is the first demonstration of a watt-class, true CW laser based on Fe^{2+}-doped materials.

Using the newly redesigned sample holder, the cavity was reconfigured into a bow tie configuration as shown in Figure 42. The maximum power achieved was 980 mW and the beam quality was seen to be multi-mode at highest ouput power. However, the output of the cavity was seen to be effectively collimated, which makes this source a likely candidate for a pump laser for both spectroscopy and long wave laser oscillators.

4.7   Conclusions and Future Work

In summary, we achieved 840 mW of CW output power from a Fe:ZnSe laser at 4140 nm with $M^2 < 1.2$ beam quality using a doubly-pumped linear resonator. Neglecting coupling losses, the total optical efficiency of the laser was 39% at full
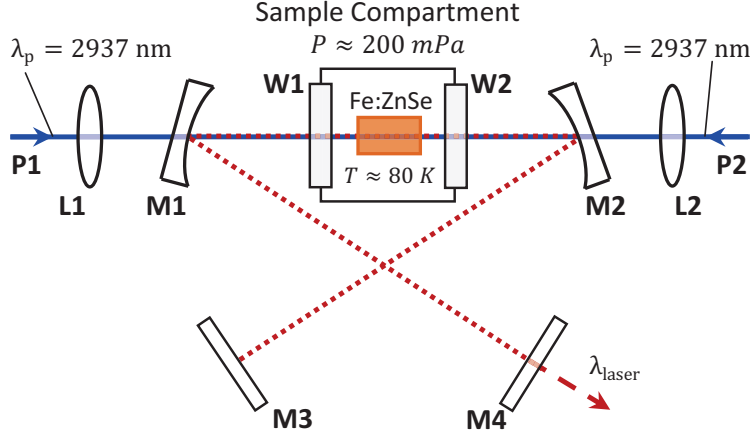
Figure 42. A bow-tie cavity design for a CW Fe:ZnSe laser.

power. The output power of the laser was limited by pump power with no indication of thermal roll-off. Discrete spectral tuning was demonstrated from ~ 3840 to ~ 4340 nm. Using a folded resonator, the maximum output power measured was increased to > 1 W. This is a $> 5\times$ increase over the maximum power achieved by Voronov in 2008 [1].

The most straightforward way of increasing the output of the Fe:ZnSe is to increase the pump power. Several experimental technologies are being developed which will increase the available pump power at ~ 3 μm. Researchers at NAWC are developing a high-power CW Er:YAG laser [58] emitting at 2937 nm. Researchers at Army Research Laboratory (ARL) are developing a high-power CW Er:Y$_2$O$_3$ laser [59], which has been shown to output 10 W of CW power at ~ 2740 nm. We are pursuing collaboration with these groups for demonstration of a multi-Watt CW Fe:ZnSe laser. If such technologies can be optimized, CW Fe:ZnSe lasers have the potential to scale to > 10 W of CW output power. Indeed, such performance seems reasonable given the performance of Cr:ZnSe.

No attempts were made to control the unstable spectral mode-hopping exhibited by this laser. Placing a spectrally narrow tuning element into the cavity may eliminate

this behavior. We recommend additional investigation into robust spectral tuning configurations such as the Littman–Metcalf cavity. This effect may be controlled using an etalon or the tuning methods mentioned previously. Ring cavity configurations should also be explored for completeness.

At the time of their demonstration, the lasers reported in this chapter exhibited the greatest CW output power reported from Fe:ZnSe. These results were published in Optics Letters [60]. Furthermore, we have demonstrated the first broadband spectral tuning of the wavelength of a CW Fe:ZnSe laser. These results were published in SPIE Conference Proceedings [61]. In the following chapter, we consider novel pulsed laser architectures based on Fe:ZnSe.

V. Pulsed Fe:ZnSe Lasers

Pulse-agile solid-state infrared lasers are of interest for military, scientific, and commercial purposes including remote sensing, laser radar, and point-to-point optical communication. Moving from a CW output format to a pulsed format enables spectroscopic techniques for which CW laser radiation is not useful. Typically, such pulses will also exhibit greater values of peak power than can be achieved in the CW case. These advantages drive development of pulsed mid-IR lasers for medical, military, and scientific applications. Both Q-switching and modelocking techniques have been used to demonstrate pulsed Cr:ZnSe lasers. In this chapter, we report the use of these pulsewidth modulation techniques to deliver short, high-peak-power pulses from an Fe:ZnSe laser.

5.1   Passive Q-switching

Q-switching is a pulse modulation technique commonly used to produce pulsed output from a continuously pumped laser cavity. The quality factor Q of the laser cavity is held low so that the gain medium can accumulate population in the upper-state. Then, Q is rapidly increased so that the energy is quickly released as an output pulse. The process can be repeated very rapidly to produce a series of short pulses.

Active Q-switching techniques involve the use of an active element such as an acousto-optic tunable filter to modulate the quality factor of the cavity. These techniques are costly and generally have low pulse repetition rates which are limited by the slew rate of the active element. An elegant alternative is to use passive Q-switching techniques. Typically, a saturable absorber is inserted into a CW laser cavity. The loss due to absorption keeps the quality factor of the cavity low and the threshold of lasing is kept high. Consequently, the intracavity intensity of the radiation emitted

from the gain medium builds over time. As the intensity builds, the saturable absorber begins to bleach and the quality factor of the cavity rapidly increases. Thus the threshold of lasing rapidly drops below the instantaneous intracavity intensity. The energy stored in the gain medium is then released as an optical pulse. As the energy is released the intracavity intensity drops below the saturation intensity of the saturable absorber and it begins to absorb again and lasing ceases. Typically the total absorption of the passive Q-switch is a few percent.

We report the demonstration of high-average-power passively Q-switched laser oscillation from Fe^{2+} ions in zinc selenide. A semiconductor saturable absorber mirror (SESAM) was used as a passive Q-switch element. Using a $60\%R$ outcoupler, the pump-limited output power was 515 mW. The spectral center of the laser was 4045 nm. The pulse repetition frequency (PRF) at maximum power was approximately 850 kHz with a corresponding minimum pulse width of 64 ns (FWHM). The pulse energy and peak power were $> 600\,nJ$ and $8.3\,W$ respectively. The average output power was limited only by available pump power and increased with a slope efficiency of 22%. No thermal roll-off of slope-efficiency was observed. The beam quality was measured to be $M^2 \leq 2.6$. The temporal stability of the pulsed output was characterized. Thermal effects were shown to play a significant role in determining the PRF of the output.

5.1.1 Experimental Setup

The Fe:ZnSe laser was operated at $\sim 80\,K$, below the activation temperature of the non-radiative processes which quench emission above 100 K [21]. As with our previous CW laser work [60], a diffusion-doped polycrystalline Fe:ZnSe sample from *IPG Photonics* with an Fe^{2+} concentration of approximately $9 \times 10^{18}\,cm^{-3}$ was used as the gain element. The Fe:ZnSe laser cavity was pumped from each end with a

pair of CW Er:YAG diode-pumped solid-state (DPSS) lasers [32] with a combined maximum pump power of 3 W at 2937 nm.

This work used an X-shaped cavity design with an overall length of 450 mm as shown in Figure 43. Mirrors $M1$ and $M2$ each had an ROC of 50 mm and were placed 100 mm from each other. This cavity geometry has the added advantage that the laser mode is roughly collimated in the crossed legs of the cavity. This collimation greatly facilitates the addition of other intracavity elements, such as a semiconductor saturable absorber mirror (SESAM). Additionally, the output of such a cavity is also nearly collimated. The beam quality of each pump beam was measured to be $M^2 \leq 2$ and each was focused through cavity mirrors into the center of the Fe:ZnSe sample. Two $f = 100$ mm lenses $L1$ and $L2$ were used to obtain beamwaist diameters of 210 μm. The calculated mode diameter in the cavity was 220 μm in the tangential plane and 270 μm in the sagittal plane. The Fe:ZnSe sample was $2 \times 6 \times 8$ mm^3 and its two smallest facets were broadband AR coated from 2900 to 5000 nm. This sample was wrapped in indium foil and mounted to a copper cold-finger cooled by liquid nitrogen to $\sim 80K$. The sample compartment was evacuated to thermally insulate the Fe:ZnSe sample and the windows $W1$ and $W2$ were AR-coated from 2900 to 5000 nm. Mirror $M3$ had an ROC of 50 mm and focused the roughly collimated cavity mode to a small diameter on the SESAM.

The SESAM was grown by researchers at Naval Research Laboratory (NRL), and is comprised of a Bragg mirror, an absorbing superlattice structure and a GaSb cap. The Bragg mirror consisted of 22.5 periods of alternating GaSb/AlAs$_{0.08}$Sb$_{0.92}$ layers grown on a GaSb substrate (with reflectivity $> 99\%$ at 4.5 μm). The absorbing superlattice was fabricated within a resonant cavity with length $2\lambda/n_{eff}$ so that the antinodes of resonance would be positioned within the absorbing region. The superlattice consisted of 129 periods of alternating InAs / Ga$_{0.92}$In$_{0.08}$Sb layers with
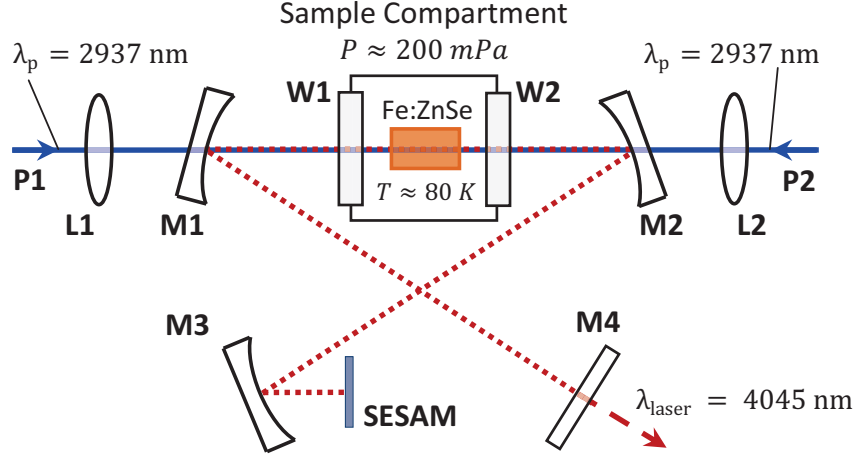
Figure 43. A schematic view of the Q-switched Fe:ZnSe laser design. All optics are made of CaF_2 and anti-reflection coated at 2937 nm unless otherwise noted.

thicknesses of 23.0 Å and 27.6 Å respectively. This superlattice had an energy gap of 275 meV ($\lambda = 4.5\ \mu m$) at room temperature and a 10 nm thick GaSb cap. The weak cavity is formed by the Bragg mirror and the interface between the air and the GaSb substrate and exhibits a fundamental mode at 4.5 μm. Simulations performed at NRL predicted that by saturating the optical absorption in the superlattice, the reflectivity from the entire structure can be modulated from $\sim 35\%$ to $> 99\%$. The SESAM was mounted on a linear stage so that the cavity mode size could be optimized for greatest average power. The cavity design accommodated a flat outcoupling mirror $M4$. Laser performance was evaluated for several outcouplers with different values of reflectivity.

5.1.2 Power Scaling

The operating parameters of the laser reported in this chapter correspond to operation with a 60% R outcoupling mirror unless otherwise indicated. In this configuration, the threshold of lasing was 376 mW and the output power increased with 22% slope efficiency with respect to coupled input power (see Figure 44). Note that the slope efficiency suddenly increases for input power $> 1800\ mW$; we hypothesize that this is most likely due to a change in the transverse mode profile.
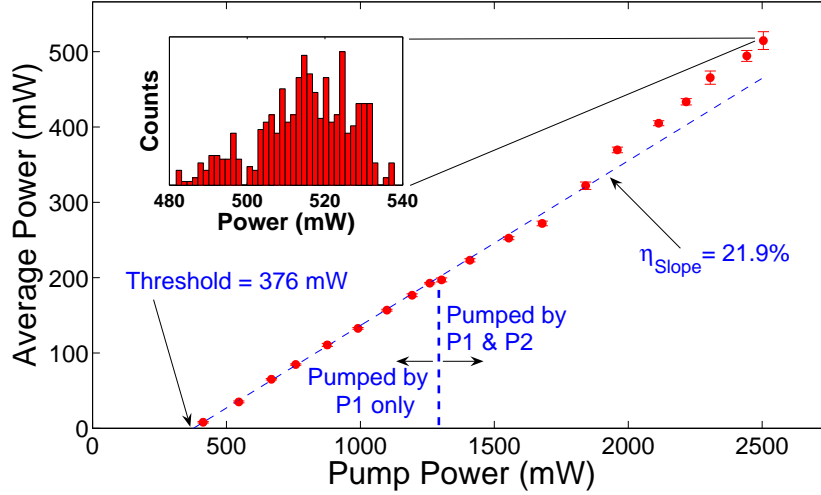
Figure 44. The average output power of the laser with respect to the input pump power. Error bars correspond to $\pm\sigma$, the standard deviation of 500 measurements of the average power. The inset shows a histogram of the measured average output power measured at maximum pump power.

With both pump lasers operating at full-power, the maximum output of the Fe:ZnSe laser was measured to be 515 ± 12 mW. The greatest average power observed from this laser was 627 mW and was achieved using a 44% R outcoupling mirror. However, the trends of Figure 44 and Figure 46 exhibited substantially more variation in this configuration.

The values of input power shown on Figure 44 are direct measurements of the power incident on the windows to the sample compartment. Spectral scans of the output with a monochromator show no content at the pump wavelength. The threshold and slope efficiency of the laser were extracted as fit parameters from a least-squares fit of a linear model to the average output power data plotted against input power. Table 11 shows the pump power at the threshold of lasing, the maximum average power, and the slope efficiency of the laser using 44%, 60%, 71%, 90% and 94% reflective output coupling mirrors. The slope efficiency of the laser clearly increased with respect to the transmission of the outcoupling mirror. The threshold of lasing was relatively insensitive to the transmission of the outcoupling mirror, with no more

than an 100 mW increase in the threshold power resulting from the change of the outcoupling mirror reflectivity from 90% to 44% .

Table 11. The input/output power characteristics of the Q-switched Fe:ZnSe laser with different outcoupler mirrors.

Outcoupler ($\% R$)	Threshold (mW)	Max. Power (mW)	η_{slope}
44	350	627 ± 12	29%
60	376	515 ± 12	22%
71	293	395 ± 6	18%
90	252	184 ± 3	8.0%
94	291	111 ± 2	5.0%

From the inset histogram of Figure 44 we see that the average power of the laser output exhibited some variation. The coefficient of variation of the laser power was $C_v(P) = \sigma_{Power}/\mu_{Power}$ where σ_{Power} is the standard deviation of the average power and μ_{Power} is its mean. Neither the addition of a 25 μm Si etalon nor an adjustable iris within the laser cavity significantly affected the power stability $C_v(P)$ of the laser output. The SESAM was replaced with an HR dielectric mirror to force the laser to operate in the continuous wave regime. The measured instability was not significantly affected, however, the threshold of the laser fell by 12% and the slope efficiency increased by a factor of 1.6. These observations confirm that passive losses of the SESAM are significant but that the use of the SESAM does not produce the observed variation in average power.

5.1.3   Temporal Characteristics

The first Q-switched Cr:ZnSe laser was demonstrated in 2003 by Alford et al. [10] using an RTP Pockels cell to actively modulate the quality factor Q of the laser cavity. In 2005, Pollock et al. [12] demonstrated a pulsed Cr:ZnSe laser using a SESAM as a passive Q-switch. Similarly the Fe:ZnSe laser demonstrated in this work used a

SESAM as a passive Q-switch to realize pulsed output (see Figure 45) using a CW pump.
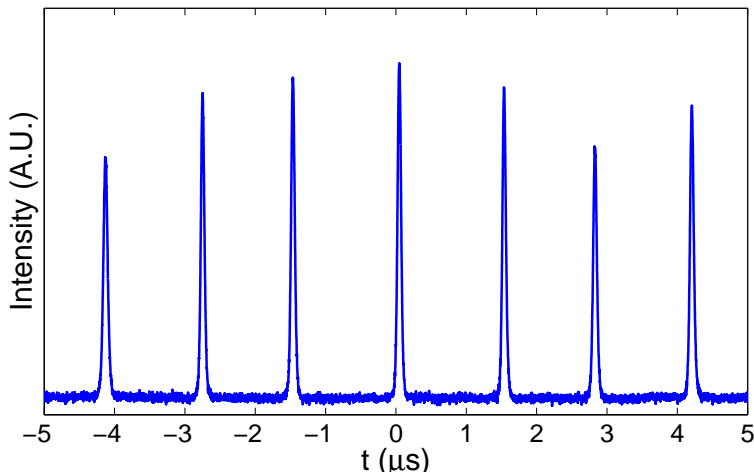
Figure 45. **The output of the laser using a 60% R outcoupling mirror and operating at maximum power. The trace was captured using a 2 GHz oscilloscope and a *VIGO PVM-10.6* photodiode with a 1.5 ns response time.**

The period T between output pulses is the time required for the intracavity radiation to grow to the saturation intensity of the SESAM. The rate of growth of the intracavity intensity is determined primarily by the outcoupler reflectivity and the input power from the pump laser(s). Thus the pulse repetition frequency $F = 1/T$ of the laser could be varied greatly by adjusting these parameters. T was measured as the average of 1000 time intervals between consecutive pulses as recorded by an oscilloscope with a fast photodiode. The PRF was observed to increase with pump power as shown in Figure 46. Note that the PRF trend exhibits a shift at 1800 mW of pump power; we hypothesize that this shift, like the jump in the output power at the same value of pump power, is due to a change in the transverse mode profile.

The increasing trend in PRF with respect to pump power was initially linear for all outcouplers. For each outcoupler, the trend rolled off with increasing pump power. Spühler et al. have shown that this trend should be strictly linear [62], so it was hypothesized that the deviation with increased power was due to thermal effects in
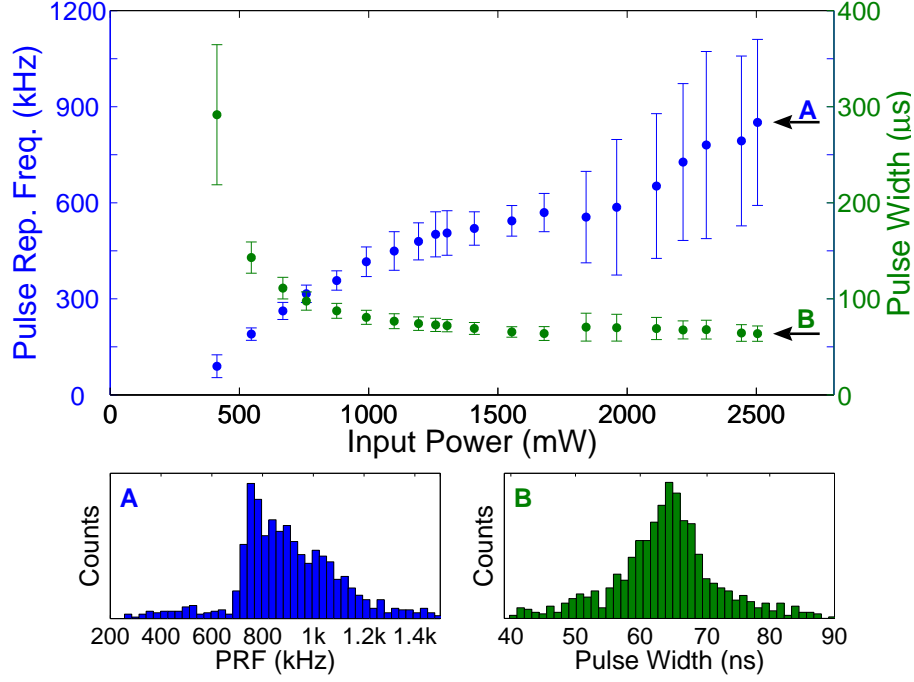
Figure 46. The temporal pulse characteristics of the laser with respect to the input pump power. Data points correspond to the mean of 1000 samples of the observed quantity and error bars correspond to $\pm\sigma$, the standard deviation of the observed quantity. The histograms show the statistical behavior of pulse characteristics at full power as indicated.

the Fe:ZnSe crystal.

The variation in the pulse-to-pulse arrival time was found to increase with the input pump power. The coefficient of variation for T can be calculated $C_v(T) = \sigma_T / \mu_T$ where σ_T is the standard deviation of the pulse-to-pulse arrival and μ_T is its mean. Both the addition of a 25 μm Si etalon and the addition of an adjustable iris within the laser cavity resulted in an increase in $C_v(T)$.

The pulse width of the output pulses was measured by recording the time average of 1000 pulses as shown in Figure 47. The width 2τ of the average pulse was extracted from a numerical fit of the hyperbolic secant squared pulse-shape

$$I(t) = A \cdot sech^2\left(\frac{t - t_0}{\tau}\right) + a \tag{5.1.1}$$

97

to the time-averaged pulse. It can be shown that the FWHM pulse width of a secant-squared shaped pulse can be calculated as $W_{FWHM} = 0.8814 \cdot 2\tau$. All pulse widths reported in this work are FWHM values determined in this manner.
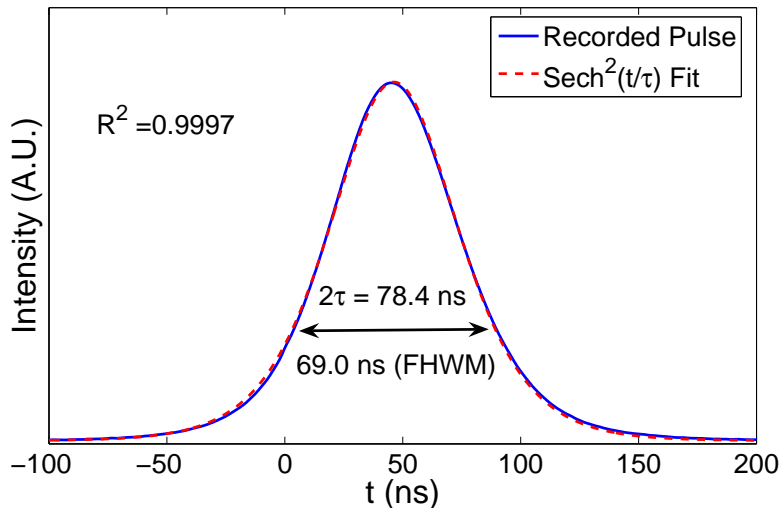
Figure 47. A time-average of 1000 pulses from the laser at maximum power. The numerical fit (dashed red line) of a hyperbolic secant distribution exhibits excellent agreement with the recorded average pulse (solid blue line).

For all outcouplers, the width of the average pulse decreased with respect to pump power and asymptotically approached some limiting value (see Figure 46). The pulse width was 64 ns at maximum pump power for the 60% R outcoupler. The minimum pulse width observed was 56 ns at maximum pump power using a 94% R outcoupling mirror. Spühler et al. have shown that the pulse width of a SESAM Q-switched laser should be insensitive to the pump power. However, they also demonstrated a Nd:YVO$_4$ SESAM Q-switched laser for which the pulse width is considerably larger than the limiting value near threshold. They ascribed this behavior to terms neglected in their theoretical analysis [62], though it is not clear that these terms were responsible for the similar behavior observed in this work.

It can be shown that, for a hyperbolic secant-squared shaped pulse, the pulse energy of the average pulse can be directly calculated $P_{peak} = PT/2\tau$ where P is

the average power, T is the average period between pulses, and 2τ is the average pulse width. Using the 60% R outcoupler, the maximum average power value was 515 mW at a PRF of 851 kHz. The pulse width $2\tau = 72.3$ ns implies a pulse energy of 605 nJ and a peak power of 8.3 W, substantially greater than the average value of power. Table 12 shows the operating characteristics of the output of the laser using 44%, 60%, 71%, 90% and 94% R reflective output coupling mirrors.

Table 12. The temporal characteristics of the laser pulses with varying outcoupler mirrors at maximum pump power.

Outcoupling Mirror (% R)	PRF (kHz)	Pulse Width (ns)	Peak Power (W)	Pulse Energy (nJ)
44	867 ± 266	64.5 ± 26.8	8.9 ± 3.5	651 ± 201
60	851 ± 260	63.7 ± 10.3	8.3 ± 2.7	605 ± 185
71	766 ± 159	63.5 ± 10.6	7.2 ± 2.6	521 ± 109
90	712 ± 174	62.6 ± 8.9	3.7 ± 1.3	261 ± 64
94	683 ± 127	56.1 ± 7.5	2.3 ± 0.7	147 ± 27

Figure 48 shows the increase of pulse energy and peak power with increased pump power. Note that the instability of the laser increases substantially with increasing pump power. Again we note an abrupt change in the behavior at 1800 mW of pump power. The variation in the peak power and pulse energy calculation are derived from the variation of the pulse-to-pulse period seen in Figure 46.

5.1.4 Thermal Effects

Recall that Figures 2, 4, and 6 exhibit behavior consistent with a sudden change of the transverse mode of the laser cavity at a pump power of 1800 mW. We have hypothesized that this is due to thermal effects induced in the gain medium by the pump laser. To test this hypothesis, the laser cavity was operated with pump laser $P1$ at full power and $P2$ off. The pulse width and repetition frequency were observed both with $P1$ free-running and with $P1$ chopped by a 50% duty-cycle chopper wheel
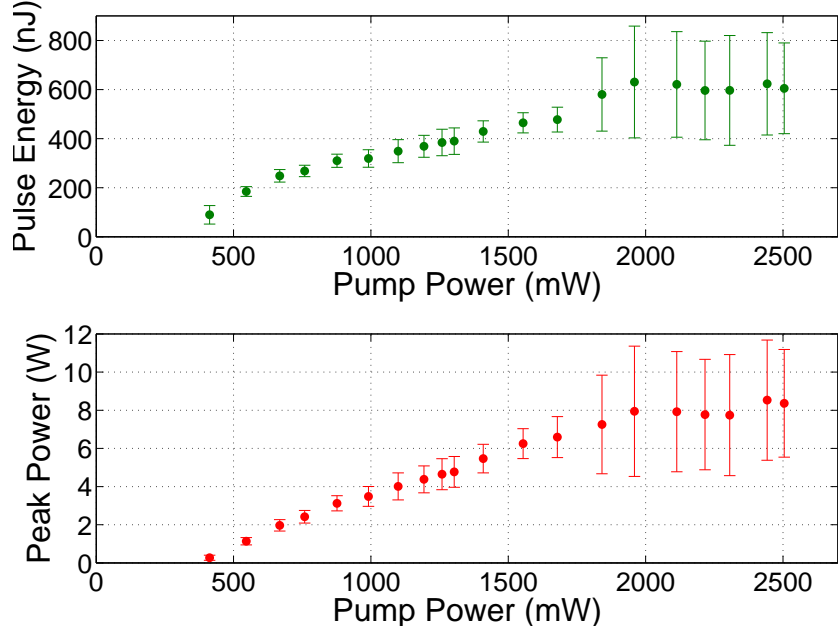
Figure 48. The average pulse energy and peak power of the laser with respect to pump power.

at $\sim 150 \ Hz$. The instantaneous pump power is identical in both cases, and the chopping time is much longer than the temporal pulse width of the laser, so the laser dynamics should be identical in both cases. However, the thermal load on the cooling system in the continuously illuminated case is twice that of the chopped case. Thus, thermal lensing is more severe. The result of this lensing is a change of the mode size of the cavity mode on the SESAM, and thus a change in the amount of time it takes for the absorption to saturate. Thus, these two configurations exhibit different pulse behavior as seen in Figure 49.

5.1.5   Beam Quality

To measure the beam quality of the laser, the output of the Fe:ZnSe laser was focused using a 75 mm lens. The beamwidth $w(z)$ of the focused beam was measured using the second moments definition. Measurements were taken at evenly spaced locations along the optic axis using a *Photon Inc. Nanoscan* scanning slit beam

100
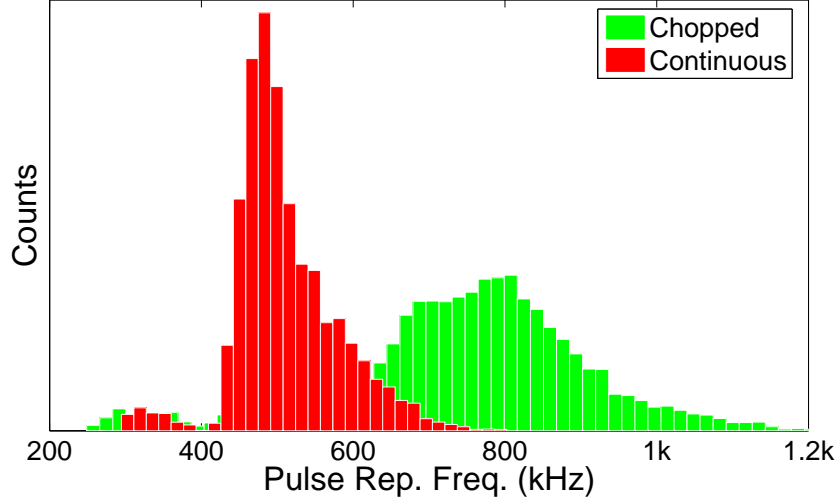
Figure 49. The histograms of pulse repetition frequency of the laser output with P2 off and with (green) and without (red) P1 chopped at a 50% duty cycle.

profiling tool. The beam quality M^2 and the beamwaist radius w_0 were determined as parameters of a least-squares fit to the beam width data of the Gaussian beam propagation formula

$$w(z) = w_0 \cdot \sqrt{1 + M^2 \left(\frac{z}{z_R}\right)^2} \qquad (5.1.2)$$

where z_R is the Rayleigh range of the beam, w_0 is the beamwaist and the zero of z is defined at the beamwaist. Figure 50 shows the profile of the output beam. When pumping with both $P1$ and $P2$ at full power the beam quality was measured to be $M_S^2 = 1.27$ and $M_T^2 = 2.60$. This astigmatism was expected as a consequence of a non-zero angle of incidence of the cavity mode on the curved mirrors $M1$ and $M2$.

5.1.6   Spectral Content

The output of the laser, both at threshold and at full power, was spectrally resolved using an *Acton SpectraPro-300* monochromator with a liquid nitrogen cooled InSb detector. The instrument used a 1.5" effective grating diameter with 300 gr/mm
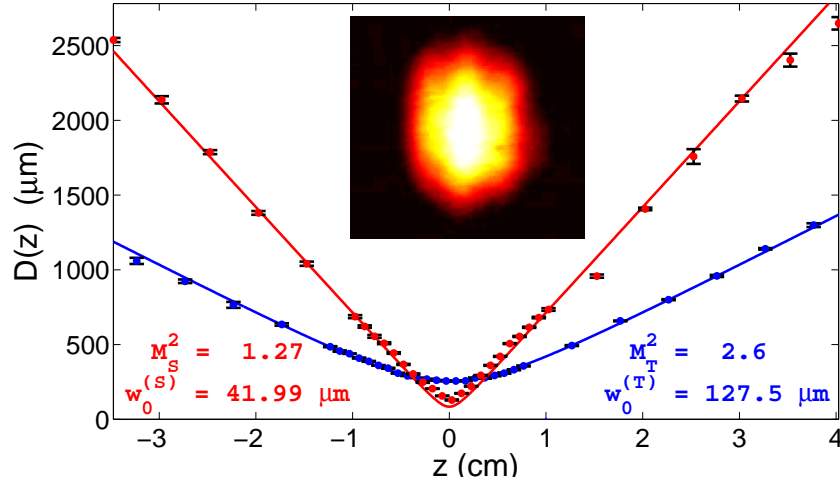
Figure 50. Beam profile of the Fe:ZnSe laser operating at maximum power. The inset is a picture of the beam as recorded by an *Electrophysics PV320* beamprofiling camera.

blazed at 2 μm. The slits were set to 100 μm, so that the wavelength resolution was < 2 nm. Figure 51 shows the time average emission spectra of the laser at threshold and maximum power. The threshold output wavelength of 4045 nm varies substantially from the 4140 nm reported in our CW Fe:ZnSe laser work [60], but is consistent with other free-running Fe:ZnSe lasers [1].This change is due to spectral
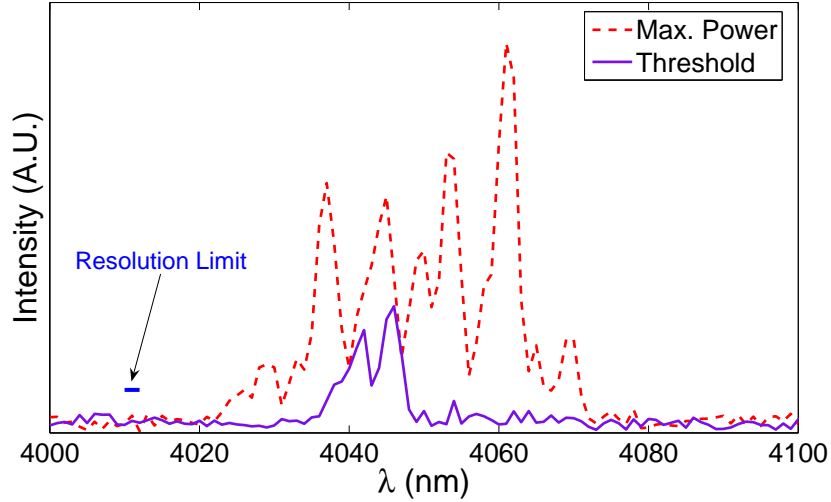
Figure 51. The emission spectra of the Fe:ZnSe laser operating at threshold (solid) and at maximum average power (dashed). The structure in the output is consistent with behavior observed in our CW Fe:ZnSe laser work (see [60]) that was theorized to be evidence of mode-hopping.

102

differences in the reflectivity of the coatings of the mirrors used as well as the spectral losses introduced by the SESAM. Clearly, the spectral width of the output increases with pump power. The structure observed in the output spectrum was also observed in our CW work and was found to be a consequence of time averaging. The individual peaks were not simultaneously present in the output. A linear array on the output of a monochromator allowed real-time monitoring of the output spectrum and the laser was observed to rapidly switch between operation at each wavelength. Time-resolved spectroscopic monitoring of the output of the Q-switched laser was not attempted, though the structure in the time-averaged output spectrum is consistent with mode-hopping.

5.2   Passive Modelocking

Passive modelocking operates on a similar principle to passive Q-switching. A saturable absorbing mirror used in the laser cavity will behave like a passive Q-switch, establishing pulsed output. A portion of this pulse is reflected back into the laser cavity and resonates. If the recovery time of the saturable absorbing mirror is short enough, the mirror can be forced to saturate upon every round trip of of the circulating pulse, periodically lowering the cavity loss. If the gain of the laser material is such that the gain only exceeds the cavity losses when the absorber saturates, then fields whose intensities do not exceed the saturation intensity of the absorber do not experience gain. Thus the leading edge of the circulating pulse is not amplified and is suppressed by competition. The circulating pulse quickly becomes shorter as it resonates. The steady state result is an ultrashort pulse (or pulses) resonating in the cavity whose round trip losses equal its round trip gain. A portion of this pulse is coupled out of the cavity and the emission is seen to be ultrashort.

Using a semiconductor saturable absorbing mirror (SESAM), Cr:ZnSe has been

shown to operate modelocked with pulses shorter than 5 ps [11, 63]. Kerr-lens mode-locking (KLM) of Cr:ZnSe has also been demonstrated [64]. Modelocking of Fe:ZnSe has not been reported in the literature. We report what is most likely demonstration of ultrashort pulsed output from a KLM Fe:ZnSe laser. To the knowledge of the author, this is the first demonstration of modelocking in Fe:ZnSe.

5.2.1 Experimental Setup

The cavity configuration of the modelocked cavity was almost identical to the configuration used in the Q-switched work. The primary differences are the replacement of M3 with a simple protected silver mirror, and the addition of a variable aperture just inside the $95\%R$ output coupler M4. Figure 52 shows the experimental setup used to generate these pulses.
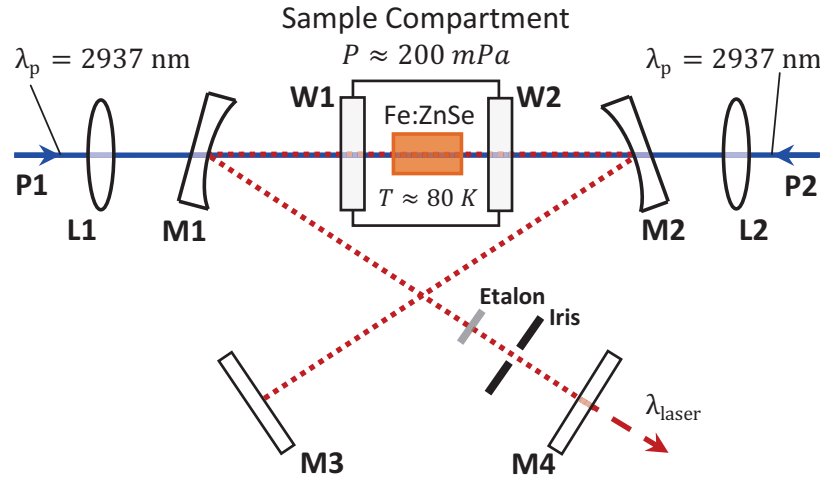
Figure 52. A diagram of the experimental setup used to generate ultrashort KLM pulses from Fe:ZnSe.

Modes propagating in the Fe:ZnSe gain medium induce a nonlinear index change n_2 via the Kerr effect. The effect is greater for pulsed modes (seeded from noise) than for CW modes, and thus they experience greater focusing. Thus, the aperture introduces selective losses to CW modes and the pulsed modes dominate.

5.2.2   Performance

The trace of Figure 53 was captured using a 2 *GHz* oscilloscope and a *VIGO PVM-10.6* photodiode with a 1.5 *ns* response time. Due to measurement limitations on available photo-diodes, the measured temporal pulse width of these lasers pulses is the impulse response of the photodiode. The pulse repetition frequency (PRF)of the laser corresponded to the round-trip time of an optical pulse within the cavity. Thus, it seems that so called *fundamental* modelocking was occurring, with only one pulse traveling in the cavity at a time. The pulsewidth of the output pulses could not be measured directly due to the response time of the photodiode.
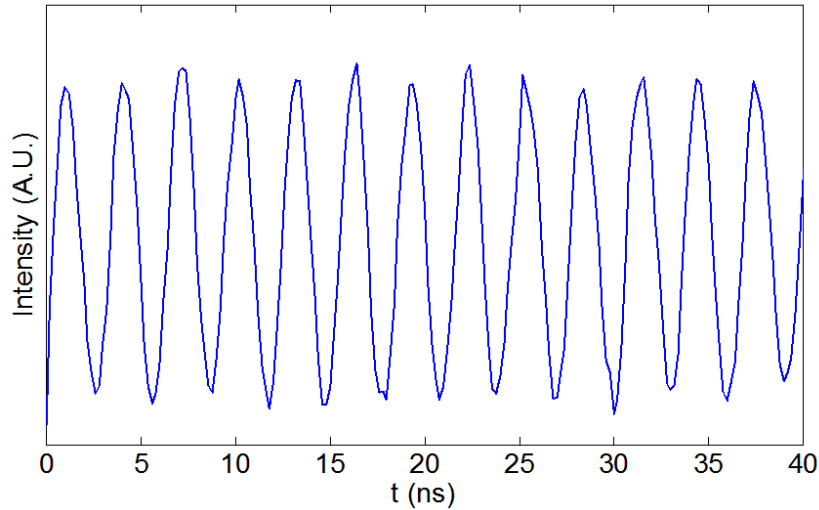
Figure 53. The output of the KLM laser at maximum pump power.

With the variable aperture fully opened, the resonator seemed to tend toward (inefficient) CW operation. As the aperture was gradually closed, the cavity could be induced to hard-aperture modelocked behavior. Closing the aperture too tightly resulted in Q-switched output. With the aperture closed such that the output appeared to be modelocked pulses, the rear HR mirror M3 could be adjusted to stabilize the modelocking somewhat. This stabilization introduced a soft aperture (analogous to gain-guiding) to the nonlinear ZnSe medium. In this configuration, the variable

aperture could be opened without loss of modelocked operation.

The addition of a 50 μm Si etalon increased the average power of the output by $\sim 25\%$. This result is surprising and has not been fully explained. The maximum output power observed was 205 mW with power pump lasers at full power. In this configuration, the output exhibited a tendency to restart modelocking on the order of microseconds. Adjustment to the alignment of M3 could induce clear Q-switched modelocked output. Thus, we theorize that Q-switching instabilities are periodically disrupting and resetting the modelocking even though the output appears more like CW modelocking than classic Q-switched modelocking.

5.2.3   Stability

Several techniques exist for stabilizing SESAM modelocked oscillators. A review of some literature [65, 66] suggests that one approach to stabilizing the cavity is to increase the pulse energy of the short pulses. For SESAM modelocked lasers, the oscillator will operate in CW modelocked regime if and only if the average energy of the short pulses exceeds the Q-Switched modelocking (QML)parameter of the laser. This parameter contains all the parameters relevant to the laser dynamics of the oscillator. However, the QML parameter explicitly includes design parameters of the SESAM used to produce the modelocking. Thus, the analysis is, strictly speaking, applicable only to SESAM modelocked lasers.

The variable aperture can be thought of in terms of an equivalent SESAM, but it is not clear how the parameters of the aperture could be translated to the parameters included in the QML factor. Nonetheless, we have proceeded by attempting to increase the energy of the short pulses. The most straightforward way of achieving this goal is to increase the length the resonator. Recall that, for a pulsed laser, the pulse energy can be determined as $E = P/f_{rep}$ where P is the average output power

of the laser and f_{rep} is the pulse repetition frequency of the laser. For fundamental KLM, the PRF of the laser is the inverse of the round trip time of an optical pulse in the cavity $f_{rep} = c/L$ where L is the total length of the cavity. Thus we find that, for a given average power, the pulse energy can be calculated as $E_{pulse} = P \cdot L/c$. The cavity was lengthened from 450 mm to ~ 1000 mm to double the short pulse energy. We found that the average power dropped from ~ 200 mW to ~ 60 mW and so the energy per pulse was actually reduced. Not surprisingly, the stability of laser did not appear to have improved.

Stabilization of the modelocking could also be attempted using dispersion compensation. The operating principle behind this approach is that reduction in the round-trip dispersion in the cavity will result in shorter pulses. If the energy of these pulses is maintained, the shorter pulses will exhibit greater field intensities and will induce a greater Kerr nonlinearity in the ZnSe and allow for greater pulse selectively by the aperture.

5.2.4 Dispersion Compensation

Two quantities of interest for dispersion compensation are the group velocity dispersion (GVD)and the group delay dispersion (GDD.) These quantities are directly related as $GDD = GVD \cdot l$ where l is the length of the dispersing element. The group velocity dispersion is defined

$$GVD = \frac{\partial^2 k}{\partial \omega^2},$$

(5.2.1)

which we can convert to an expression for wavelength. Recall that $k = 2\pi n\left(\lambda\right)/\lambda$ and that $\lambda = 2\pi c/\omega$. Substitution yields

$$GVD = \frac{\partial^2}{\partial\omega^2}\frac{2\pi n\left(\lambda\right)}{2\pi c/\omega} \tag{5.2.2}$$

$$= \frac{1}{c}\frac{\partial}{\partial\omega}\left[\frac{\partial}{\partial\omega}\left[\omega n\left(\lambda\right)\right]\right]. \tag{5.2.3}$$

Applying the product rule

$$\frac{\partial}{\partial\omega}\left[\omega n\left(\lambda\right)\right] = \frac{\partial}{\partial\omega}\left[\omega\right]\cdot n\left(\lambda\right) + \omega\cdot\frac{\partial}{\partial\omega}\left[n\left(\lambda\right)\right], \tag{5.2.4}$$

and the chain rule

$$\frac{\partial}{\partial\omega}\left[n\left(\lambda\right)\right] = \frac{\partial}{\partial\lambda}\left[n\left(\lambda\right)\right]\cdot\frac{\partial\lambda}{\partial\omega}, \tag{5.2.5}$$

we note that

$$\frac{\partial\lambda}{\partial\omega} = -\frac{2\pi c}{\omega^2}, \tag{5.2.6}$$

and we find that

$$GVD = \frac{1}{c}\frac{\partial}{\partial\omega}\left[\frac{\partial}{\partial\omega}\left[\omega\right]\cdot n\left(\lambda\right) + \omega\cdot\frac{\partial}{\partial\omega}\left[n\left(\lambda\right)\right]\right] \tag{5.2.7}$$

$$= \frac{1}{c}\frac{\partial}{\partial\omega}\left[n\left(\lambda\right) + \omega\cdot\frac{\partial}{\partial\lambda}\left[n\left(\lambda\right)\right]\cdot\frac{\partial\lambda}{\partial\omega}\right] \tag{5.2.8}$$

$$= \frac{1}{c}\frac{\partial}{\partial\omega}\left[n\left(\lambda\right) - \frac{2\pi c}{\omega}\cdot n'\left(\lambda\right)\right] \tag{5.2.9}$$

$$= \frac{1}{c}\left[-\frac{2\pi c}{\omega^2}n'\left(\lambda\right) - 2\pi c\frac{\partial}{\partial\omega}\frac{n'\left(\lambda\right)}{\omega}\right]. \tag{5.2.10}$$

To evaluate the derivatives, we again apply the product rule

$$\frac{\partial}{\partial \omega} \frac{n'(\lambda)}{\omega} = \frac{\partial}{\partial \omega} \left[\frac{1}{\omega}\right] \cdot n'(\lambda) + \frac{1}{\omega} \frac{\partial}{\partial \omega} \left[n'(\lambda)\right], \tag{5.2.11}$$

and then the chain rule

$$\frac{\partial}{\partial \omega} \left[n'(\lambda)\right] = -\frac{2\pi c}{\omega^2} n''(\lambda). \tag{5.2.12}$$

So,

$$GVD = \frac{1}{c} \left[-\frac{2\pi c}{\omega^2} n'(\lambda) - 2\pi c \left(\frac{\partial}{\partial \omega} \left[\frac{1}{\omega}\right] \cdot n'(\lambda) + \frac{1}{\omega} \frac{\partial}{\partial \omega} \left[n'(\lambda)\right] \right) \right] \tag{5.2.13}$$

$$= \frac{1}{c} \left[-\frac{2\pi c}{\omega^2} n'(\lambda) + \frac{2\pi c}{\omega^2} \cdot n'(\lambda) + \frac{1}{\omega} \frac{4\pi^2 c}{\omega^2} n''(\lambda) \right] \tag{5.2.14}$$

$$= \frac{1}{c} \left[\frac{4\pi^2 c}{\omega^3} n''(\lambda) \right] \tag{5.2.15}$$

$$= \frac{\lambda^3}{2\pi c^3} n''(\lambda). \tag{5.2.16}$$

We simulate the addition of a Si Brewster plate to the resonator of Figure 52 for dispersion compensation. The round-trip group delay dispersion is then

$$GDD = 2 \sum_i \left(\frac{\lambda^3}{2\pi c^3} n_i''(\lambda) \cdot l_i \right) \tag{5.2.17}$$

$$= 2 \frac{\lambda^3}{\pi c^3} \left(n_{ZnSe}''(\lambda) \cdot l_{ZnSe} + 2 \cdot n_{CaF_2}''(\lambda) \cdot l_{CaF_2} + n_{Si}''(\lambda) \cdot l_{Si} \right). \tag{5.2.18}$$

with $l_{ZnSe} = 8.15\ mm$, $l_{CaF_2} = 3.15\ mm$, and $l_{Si} = 3\ mm/\cos(\theta_B(\lambda))$ and the refractive indices given by Sellmeier formulae from Hawkins [67], Tropf [68], and Frey [69] respectively. Figure 54 shows the spectral GDD in the laser cavity. Note that, with the addition of the Si Brewster plate, the group delay dispersion is $GDD \approx -1100\ fs^2$ at $4050\ nm$. Thus the laser will operate in the negative dispersion regime,

which is recommended by literature. The value is similar to the value used by Sorokina et al. in a SESAM modelocked Cr:ZnSe laser [63] .
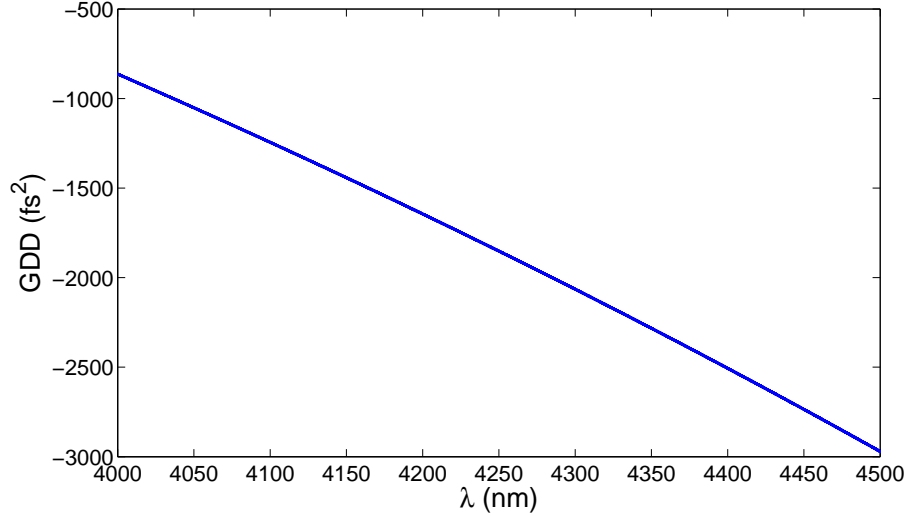
Figure 54. The round-trip GDD of the resonator shown in Figure 52 with the addition of a 3 mm Si Brewster plate for dispersion compensation.

One additional source of instability is the observed tendency for Fe:ZnSe to exhibit spectral mode-hopping [60]. The etalon provides spectral selectivity in this cavity, though additional spectral selectivity may improve the stability of the laser. For example, Cizmeciyan et al. used two intracavity prisms to provide dispersion compensation in a KLM Cr:ZnSe laser [64].

It is hoped that the combination of spectral selectivity, dispersion compensation, and increased energy/pulse will stabilize the KLM Fe:ZnSe laser against Q-switching instabilities. Stable CW KLM operation will be required to so that pulse width measurement can be performed via auto-correlation techniques. Such techniques measure the width over the duration of many pulses and so stable output is the key to achieving repeatable pulse width measurements. We attempted to make an auto-correlation measurement of pulse width of the laser, but were unsuccessful do the pulse-instability of the output.

5.3 Conclusions and Future Work

In conclusion, we have demonstrated > 0.6 W of Q-switched output power at PRFs > 850 kHz from a CW-pumped Fe:ZnSe laser. The temporal characteristics of the output pulse train were demonstrated to vary greatly with respect to the average output power. The minimum pulse width measured from the laser was 56 ns. The output wavelength of the laser exhibited some variation but was centered at 4045 nm and the beam quality was $M^2 < 2.60$. Neglecting coupling losses, the maximum achieved optical efficiency of the laser was 25% at full power. The average output power of the laser was only limited by the available pump power. The pulsewidth and the PRF of the output were observed to depend directly on the input power. Significant deviations from the trends predicted by Spühler et al. for a passively Q-switched laser were observed for these quantities and evidence was presented that thermal effects significantly affect the pulse repetition frequency of the laser.

We have also demonstrated the first evidence of KLM in Fe:ZnSe. Power-scaling efforts will require more pump power than the currently available 3 W. We recommend attempts to stabilize of the modelocking of the laser using dispersion compensation and spectrally selective intracavity elements such as a prism pair. Moreover, it cannot be said with certainty that the observed behavior is modelocking until auto-correlation methods of measuring the pulse width have confirmed that the pulse widths are significantly less than the combined bandwidth of the photo-detector and oscilloscope.

VI. Conclusion

Three research objectives were outlined at the start of this work:

1. Thorough spectroscopic characterization of Fe:ZnSe

2. CW power scaling of Fe:ZnSe Lasers beyond 1 W

3. Novel pulse modulation of a Fe:ZnSe laser

Spectroscopic studies of Fe:ZnSe were conducted per Objective 1. Absorption spectroscopy studies were performed on Fe:ZnSe at 10 K and were successful in resolving lines corresponding to zero-phonon transition from the lower state manifold to the upper state manifold. Laser-induced fluorescence studies were performed on Fe:ZnSe at 5 K and were also successful in resolving zero-phonon lines. Lines in the spectra were assigned to specific transitions as described by a theoretical model. Temperature-dependent absorption and LIF studies were conducted from 10 K to 300 K and 5 K to 225 K respectively. The effects of non-radiative quenching were directly observed in the LIF spectra. Temperature-dependent measurements of the upper state lifetime of polycrystalline Fe:ZnSe were taken. The data were consistent with previous measurements by Myoung et al. A nonlinear model was developed that fits these data very well. These insights contribute substantially to the body of knowledge concerning Fe:ZnSe. This work will be submitted for publication in a peer-reviewed journal.

CW Fe:ZnSe lasers were built per Objective 2. Laser oscillation from Fe:ZnSe was shown to scale beyond 1 W. Discrete wavelength tuning of the CW Fe:ZnSe laser was also demonstrated. Several resonator architectures were explored. The output of these lasers was seen to have high beam quality and showed no thermal roll-off at maximum pump power. Power-scaling efforts were limited by the available pump

power and multi-watt operation of this system is feasible. The work was published in Optics Letters [60] and SPIE Conference Proceedings [61].

CW-pumped, pulsed Fe:ZnSe lasers were built in accordance with Objective 3. The first passively Q-switched Fe:ZnSe laser was successfully demonstrated with average power > 600 mW and with pulse widths < 60 ns. The output of the laser was thoroughly characterized. This work has been accepted for publication in IEEE Journal of Quantum Electronics [70]. Additionally, the first modelocked Fe:ZnSe laser was successfully demonstrated with average power of ~ 200 mW. Characterization is ongoing, and submission to a peer-reviewed journal is expected.

In conclusion, substantial gains in understanding the optical behavior of Fe:ZnSe have been made and substantial development of Fe:ZnSe lasers has been realized. A strong foundation for additional research has been built. Both CW and pulsed Fe:ZnSe lasers have been built which can seed optical amplifiers or pump long-wave lasers and nonlinear optical frequency converters for generation of longwave mid-IR radiation. Certainly, no small amount of future work remains to be done.

References

[1] A. A. Voronov, V. I. Kozlovskii, Y. V. Korostelin, A. I. Landman, Y. P. Podmar'kov, Y. K. Skasyrskii, and M. P. Frolov, "A continuous-wave Fe^{2+}:ZnSe laser," *Quantum Electronics*, vol. 38, no. 12, p. 1113, 2008. [Online]. Available: http://stacks.iop.org/1063-7818/38/i=12/a=A06

[2] J. J. Adams, C. Bibeau, R. H. Page, and S. A. Payne, "Tunable laser action at 4.0 microns from Fe:ZnSe," in *Advanced Solid State Lasers*. Optical Society of America, 1999, p. WD3. [Online]. Available: http://www.opticsinfobase.org/abstract.cfm?URI=ASSL-1999-WD3

[3] A. A. Voronov, V. I. Kozlovskii, Y. V. Korostelin, A. I. Landman, Y. P. Podmar'kov, and M. P. Frolov, "Laser parameters of a Fe:ZnSe crystal in the 85-255 K temperature range," *Quantum Electronics*, vol. 35, no. 9, p. 809, 2005. [Online]. Available: http://stacks.iop.org/1063-7818/35/i=9/a=A08

[4] V. A. Akimov, A. A. Voronov, V. I. Kozlovskii, Y. V. Korostelin, A. I. Landman, Y. P. Podmar'kov, and M. P. Frolov, "Efficient IR Fe:ZnSe laser continusouly tunable in the spectral range from 3.77 to 4.40 microns," *Quantum Electronics*, vol. 34, no. 10, pp. 912–914, 2004. [Online]. Available: http://stacks.iop.org/1063-7818/34/i=10/a=A06

[5] J. Kernal, V. V. Fedorov, A. Gallian, S. B. Mirov, and V. V. Badikov, "3.9-4.8 μm gain-switched lasing of Fe:ZnSe at room temperature," *Opt. Express*, vol. 13, no. 26, pp. 10608–10615, Dec 2005. [Online]. Available: http://www.opticsexpress.org/abstract.cfm?URI=oe-13-26-10608

[6] P. A. Berry and K. Schepler, "High-Power, Widely Tunable Cr^{2+}:ZnSe Laser," in *Conference on Lasers and Electro-Optics*. Optical Society of America, 2010, p. CMDD5. [Online]. Available: http://www.opticsinfobase.org/abstract.cfm?URI=CLEO-2010-CMDD5

[7] J. T. Seo, U. Hömmerich, H. Zong, S. B. Trivedi, S. W. Kutcher, C. C. Wang, and R. J. Chen, "Mid-Infrared Lasing from a Novel Optical Material: Chromium-Doped $Cd_{0.55}Mn_{0.45}Te$," *Physica Status Solidi (a)*, vol. 175, no. 1, pp. R3–R4, 1999. [Online]. Available: http://dx.doi.org/10.1002/(SICI)1521-396X(199909)175:1⟨R3::AID-PSSA99993⟩3.0.CO;2-W

[8] J. McKay, K. L. Schepler, and G. C. Catella, "Efficient grating-tuned mid-infrared Cr^{2+}:CdSe laser," *Opt. Lett.*, vol. 24, no. 22, pp. 1575–1577, Nov 1999. [Online]. Available: http://ol.osa.org/abstract.cfm?URI=ol-24-22-1575

[9] R. Page, K. Schaffers, L. DeLoach, G. Wilke, F. Patel, J. Tassano, J.B., S. Payne, W. Krupke, K.-T. Chen, and A. Burger, "Cr^{2+}-doped zinc chalcogenides as efficient, widely tunable mid-infrared lasers," *Quantum Electronics, IEEE Journal of*, vol. 33, no. 4, pp. 609–619, Apr 1997.

[10] W. J. Alford, G. J. Wagner, A. C. Sullivan, J. A. Keene, and T. J. Carrig, "High-Power and Q-Switched Cr:ZnSe Lasers," in *Advanced Solid-State Photonics*. Optical Society of America, 2003, p. 13. [Online]. Available: http://www.opticsinfobase.org/abstract.cfm?URI=ASSP-2003-13

[11] T. J. Carrig, G. J. Wagner, A. Sennaroglu, J. Y. Jeong, and C. R. Pollock, "Mode-locked Cr^{2+}:ZnSe laser," *Opt. Lett.*, vol. 25, no. 3, pp. 168–170, Feb 2000. [Online]. Available: http://ol.osa.org/abstract.cfm?URI=ol-25-3-168

[12] C. R. Pollock, N. A. Brilliant, D. Gwin, T. J. Carrig, W. J. Alford, J. B. Heroux, W. I. Wang, I. Vurgaftman, and J. R. Meyer, "Mode locked and Q-switched Cr:ZnSe laser using a Semiconductor Saturable Absorbing Mirror (SESAM)," in *Advanced Solid-State Photonics (TOPS)*. Optical Society of America, 2005, p. 252. [Online]. Available: http://www.opticsinfobase.org/abstract.cfm?URI=ASSP-2005-252

[13] A. Sennaroglu, U. Demirbas, N. Vermeulen, H. Ottevaere, and H. Thienpont, "Continuous-wave broadly tunable Cr^{2+}:ZnSe laser pumped by a thulium fiber laser," *Optics Communications*, vol. 268, no. 1, pp. 115 – 120, 2006. [Online]. Available: http://www.sciencedirect.com/science/article/pii/S003040180600681X

[14] P. A. Berry, "Versatile Chromium-Doped Zinc Selenide Infrared Laser Sources," no. AFRL-RY-WP-TR-2010-1107, 2010. [Online]. Available: http://oai.dtic.mil/oai/oai?verb=getRecord&metadataPrefix=html&identifier=ADA526209

[15] I. S. Moskalev, V. V. Fedorov, S. B. Mirov, P. A. Berry, and K. L. Schepler, "12-Watt CW Polycrystalline Cr^{2+}:ZnSe Laser Pumped by Tm-Fiber Laser," in *Advanced Solid-State Photonics*. Optical Society of America, 2009, p. WB30. [Online]. Available: http://www.opticsinfobase.org/abstract.cfm?URI=ASSP-2009-WB30

[16] T. Carrig, A. Zakel, G. Wagner, and W. Alford, "Chromium–doped chalcogenide lasers," in *Lasers and Electro-Optics Society, 2005. LEOS 2005. The 18th Annual Meeting of the IEEE*, Oct. 2005, pp. 260 – 261.

[17] G. J. Wagner, B. G. Tiemann, W. J. Alford, and T. J. Carrig, "Single–Frequency Cr:ZnSe Laser," in *Advanced Solid-State Photonics (TOPS)*. Optical Society of America, 2004, p. 371. [Online]. Available: http://www.opticsinfobase.org/abstract.cfm?URI=ASSP-2004-371

[18] H. Cankaya, M. N. Cizmeciyan, E. Beyatli, A. T. Gorgulu, A. Kurt, and A. Sennaroglu, "Injection-seeded, gain-switched tunable Cr:ZnSe laser," *Opt. Lett.*, vol. 37, no. 2, pp. 136–138, Jan 2012. [Online]. Available: http://ol.osa.org/abstract.cfm?URI=ol-37-2-136

[19] P. A. Berry and K. L. Schepler, "Cr^{2+}:ZnSe master oscillator/power amplifier for improved power scaling," pp. 75 781L–75 781L–11, 2010. [Online]. Available: http://dx.doi.org/10.1117/12.858798

[20] J. J. Adams, C. Bibeau, R. H. Page, D. M. Krol, L. H. Furu, and S. A. Payne, "4.0–4.5-μm lasing of Fe:ZnSe below 180 K, a new mid-infrared laser material," *Opt. Lett.*, vol. 24, no. 23, pp. 1720–1722, Dec 1999. [Online]. Available: http://ol.osa.org/abstract.cfm?URI=ol-24-23-1720

[21] N. Myoung, V. V. Fedorov, S. B. Mirov, and L. E. Wenger, "Temperature and concentration quenching of mid–IR photoluminescence in iron doped ZnSe and ZnS laser crystals," *Journal of Luminescence*, vol. 132, no. 3, pp. 600 – 606, 2012. [Online]. Available: http://www.sciencedirect.com/science/article/pii/S0022231311005758

[22] V. Fedorov, S. Mirov, A. Gallian, D. Badikov, M. Frolov, Y. Korostelin, V. Kozlovsky, A. Landman, Y. Podmar'kov, V. Akimov, and A. Voronov, "3.77–5.05 μm tunable solid-state lasers based on Fe^{2+}-doped ZnSe crystals operating at low and room temperatures," *Quantum Electronics, IEEE Journal of*, vol. 42, no. 9, pp. 907 –917, Sept. 2006.

[23] V. I. Kozlovsky, V. A. Akimov, M. P. Frolov, Y. V. Korostelin, A. I. Landman, V. P. Martovitsky, V. V. Mislavskii, Y. P. Podmar'kov, Y. K. Skasyrsky, and A. A. Voronov, "Room-temperature tunable mid-infrared lasers on transition-metal doped II-VI compound crystals grown from vapor phase," *physica status solidi (b)*, vol. 247, no. 6, pp. 1553–1556, 2010. [Online]. Available: http://dx.doi.org/10.1002/pssb.200983165

[24] V. A. Akimov, A. A. Voronov, V. I. Kozlovskii, Y. V. Korostelin, A. I. Landman, Y. P. Podmar'kov, and M. P. Frolov, "Efficient lasing in a Fe^{2+}:ZnSe crystal at room temperature," *Quantum Electronics*, vol. 36, no. 4, p. 299, 2006. [Online]. Available: http://stacks.iop.org/1063-7818/36/i=4/a=A01

[25] A. Gallian, I. Moskalev, V. Fedorov, S. Mirov, and K. Vodopyanov, "Parametrically Amplified Room Temperature 4.3-4.7 μm Gain-Switched Fe:ZnSe Laser," in *Conference on Lasers and Electro-Optics/Quantum Electronics and Laser Science Conference and Photonic Applications Systems Technologies*. Optical Society of America, 2006, p. CTuR4. [Online]. Available: http://www.opticsinfobase.org/abstract.cfm?URI=CLEO-2006-CTuR4

[26] N. N. Il'ichev, V. P. Danilov, V. P. Kalinushkin, M. I. Studenikin, P. V. Shapkin, and A. S. Nasibov, "Superluminescent room-temperature Fe^{2+}:ZnSe IR radiation source," *Quantum Electronics*, vol. 38, no. 2, p. 95, 2008. [Online]. Available: http://stacks.iop.org/1063-7818/38/i=2/a=L01

[27] M. Doroshenko, H. Jelínková, P. Koranda, J. Šulc, T. Basiev, V. Osiko, V. Komar, A. Gerasimenko, V. Puzikov, V. Badikov, and D. Badikov, "Tunable mid-infrared laser properties of Cr^{2+}:ZnMgSe and Fe^{2+}:ZnSe crystals," *Laser Physics Letters*, vol. 7, no. 1, pp. 38–45, 2010. [Online]. Available: http://dx.doi.org/10.1002/lapl.200910111

[28] H. Jelínková, P. Koranda, M. E. Doroshenko, J. Šulc, M. Jelínek, M. Cech, T. T. Basiev, V. V. Badikov, and D. V. Badikov, "Room-temperature lasing, gain-switched bulk, tunable Fe:ZnSe laser," pp. 772 111–772 111–6, 2010. [Online]. Available: +http://dx.doi.org/10.1117/12.854304

[29] M. E. Doroshenko, H. Jelínková, T. T. Basiev, M. Jelínek, P. Koranda, M. Němec, V. K. Komar, A. S. Gerasimenko, V. V. Badikov, D. V. Badikov, D. Vyhlídal, and J. Stoklasa, "Fe:ZnSe laser - comparison of active materials grown by two different methods," pp. 79 122D–79 122D–6, 2011. [Online]. Available: +http://dx.doi.org/10.1117/12.876082

[30] N. Myoung, D. V. Martyshkin, V. V. Fedorov, and S. B. Mirov, "Energy scaling of 4.3 μm room temperature Fe:ZnSe laser," *Opt. Lett.*, vol. 36, no. 1, pp. 94–96, Jan 2011. [Online]. Available: http://ol.osa.org/abstract.cfm?URI=ol-36-1-94

[31] V. I. Kozlovskii, Y. V. Korostelin, A. I. Landman, V. V. Mislavskii, Y. P. Podmar'kov, Y. K. Skasyrsky, and M. P. Frolov, "Pulsed Fe^{2+}:ZnS laser continuously tunable in the wavelength range of 3.49 – 4.65 μm," *Quantum Electronics*, vol. 41, no. 1, p. 1, 2011. [Online]. Available: http://stacks.iop.org/1063-7818/41/i=1/a=A01

[32] J. G. Sousa, D. Welford, and J. Foster, "Efficient 1.5 W CW and 9 mJ quasi-CW TEM_{00} mode operation of a compact diode-laser-pumped 2.94-μm Er:YAG laser," *SPIE, Proceedings of*, Feb 2010. [Online]. Available: http://sheaumann.com/wp-content/uploads/2012/07/Photonics-West-2010-Er-YAG-paper.pdf

[33] Benjah-bmm27, "Zinc-selenide-unit-cell-3D-balls," 2007. [Online]. Available: http://commons.wikimedia.org/wiki/File:Zinc-selenide-unit-cell-3D-balls.png

[34] B. Henderson and G. F. Imbusch, *Optical Spectroscopy of Inorganic Solids*, ser. Monographs on the Physics And Chemistry of Materials. Clarendon Press, Oxford, 1989.

[35] W. G. Harter, *Principles of Symmetry, Dynamics, and Spectroscopy*. Johns Hopkins University, Baltimore Maryland, Oct. 1994.

[36] B. S. Tsukerblat, *Group Theory in Chemistry and Spectroscopy*. Academic Press, London, 1994.

[37] Y. Tanabe and S. Sugano, "On the Absorption Spectra of Complex Ions II," *Journal of the Physical Society of Japan*, vol. 9, no. 5, pp. 766–779, 1954. [Online]. Available: http://jpsj.ipap.jp/link?JPSJ/9/766/

[38] G. Racah, "Theory of Complex Spectra. II," *Phys. Rev.*, vol. 62, pp. 438–462, Nov 1942. [Online]. Available: http://link.aps.org/doi/10.1103/PhysRev.62.438

[39] W. Low and M. Weger, "Paramagnetic Resonance and Optical Spectra of Divalent Iron in Cubic Fields. I. Theory," *Phys. Rev.*, vol. 118, pp. 1119–1130, Jun 1960. [Online]. Available: http://link.aps.org/doi/10.1103/PhysRev.118.1119

[40] J. Rivera-Iratchet, M. A. de Orúe, and E. E. Vogel, "Vibronic coupling and the near-infrared spectrum of Fe^{2+} in CdTe and ZnS," *Phys. Rev. B*, vol. 34, pp. 3992–4001, Sep 1986. [Online]. Available: http://link.aps.org/doi/10.1103/PhysRevB.34.3992

[41] M. K. Udo, M. Villeret, I. Miotkowski, A. J. Mayur, A. K. Ramdas, and S. Rodriguez, "Electronic excitations of substitutional transition-metal ions in II-VI semiconductors: $CdTe:Fe^{2+}$ and $CdSe:Fe^{2+}$," *Phys. Rev. B*, vol. 46, pp. 7459–7468, Sep 1992. [Online]. Available: http://link.aps.org/doi/10.1103/PhysRevB.46.7459

[42] F. S. Ham, "The Jahn–Teller effect: a retrospective view," *Journal of luminescence*, vol. 85, no. 4, pp. 193–197, 2000.

[43] G. A. Slack, F. S. Ham, and R. M. Chrenko, "Optical Absorption of Tetrahedral Fe^{2+} ($3d^6$) in Cubic ZnS, CdTe, and $MgAl_2O_4$," *Phys. Rev.*, vol. 152, pp. 376–402, Dec 1966. [Online]. Available: http://link.aps.org/doi/10.1103/PhysRev.152.376

[44] F. S. Ham and G. A. Slack, "Infrared Absorption and Luminescence Spectra of Fe^{2+} in Cubic ZnS: Role of the Jahn-Teller Coupling," *Phys. Rev. B*, vol. 4, pp. 777–798, Aug 1971. [Online]. Available: http://link.aps.org/doi/10.1103/PhysRevB.4.777

[45] H. Jahn and E. Teller, "Stability of degenerate electronic states in polyatomic molecules," *Phys. Rev. A*, vol. 49, p. 874, 1936.

[46] M. Yamaga, B. Henderson, and K. O'Donnell, "Polarization of emission spectra from Ti^{3+}-Doped oxide crystals," *Applied Physics B*, vol. 52, pp. 122–131, 1991. [Online]. Available: http://dx.doi.org/10.1007/BF00357666

[47] H. Jahn and E. Teller, "Stability of Polyatomic Molecules in Degenerate Electronic States. I. Orbital Degeneracy," *Proceedings of the Royal Society of London*, vol. 161, pp. 200–235, 1937, series A.

[48] B. Hennion, F. Moussa, G. Pepy, and K. Kunc, "Normal modes of vibrations in ZnSe," *Physics Letters A*, vol. 36, no. 5, pp. 376 – 378, 1971. [Online]. Available: http://www.sciencedirect.com/science/article/pii/0375960171902672

[49] T. Miyakawa and D. L. Dexter, "Phonon Sidebands, Multiphonon Relaxation of Excited States, and Phonon-Assisted Energy Transfer between Ions in

Solids," *Phys. Rev. B*, vol. 1, pp. 2961–2969, Apr 1970. [Online]. Available: http://link.aps.org/doi/10.1103/PhysRevB.1.2961

[50] V. A. Akimov, A. A. Voronov, V. I. Kozlovskii, Y. V. Korostelin, A. I. Landman, Y. P. Podmar'kov, and M. P. Frolov, "Intracavity laser spectroscopy by using a Fe^{2+}:ZnSe laser," *Quantum Electronics*, vol. 37, no. 11, p. 1071, 2007. [Online]. Available: http://stacks.iop.org/1063-7818/37/i=11/a=A19

[51] L. DeLoach, R. Page, G. Wilke, S. Payne, and W. Krupke, "Transition metal-doped zinc chalcogenides: spectroscopy and laser demonstration of a new class of gain media," *Quantum Electronics, IEEE Journal of*, vol. 32, no. 6, pp. 885–895, Jun 1996.

[52] H. Jelínková, M. E. Doroshenko, M. Jelínek, D. Vyhlídal, J. Šulc, M. Němec, V. Kubeček, Y. A. Zagoruiko, N. O. Kovalenko, A. S. Gerasimenko, V. M. Puzikov, and V. K. Komar, "Fe:ZnSe laser oscillation under cryogenic and room temperature," vol. 8599, 2013, pp. 85 990E–85 990E–7. [Online]. Available: http://dx.doi.org/10.1117/12.2003840

[53] A. Sennaroglu, U. Demirbas, A. Kurt, and M. Somer, "Concentration dependence of fluorescence and lasing efficiency in Cr^{2+}:ZnSe lasers," *Optical Materials*, vol. 29, no. 6, pp. 703 – 708, 2007. [Online]. Available: http://www.sciencedirect.com/science/article/pii/S092534670500515X

[54] J. McKay, W. Roh, and K. Schepler, "4.2 W Cr^{2+}:ZnSe face cooled disk laser," in *Lasers and Electro-Optics, 2002. CLEO '02. Technical Digest. Summaries of Papers Presented at the*, 2002, pp. 119 – 120 vol.1.

[55] I. T. Sorokina, E. Sorokin, S. Mirov, V. Fedorov, V. Badikov, V. Panyutin, and K. I. Schaffers, "Broadly tunable compact continuous-wave Cr^{2+}:ZnS laser," *Opt. Lett.*, vol. 27, no. 12, pp. 1040–1042, Jun 2002. [Online]. Available: http://ol.osa.org/abstract.cfm?URI=ol-27-12-1040

[56] IPG Photonics, *personal communication*, 2010.

[57] K. Schepler, R. Peterson, P. Berry, and J. McKay, "Thermal effects in Cr^{2+}:ZnSe thin disk lasers," *Selected Topics in Quantum Electronics, IEEE Journal of*, vol. 11, no. 3, pp. 713–720, May 2005.

[58] R. Shori, "personal communication," 2012.

[59] M. Dubinskiy and T. Sanamyan, "personal communication," 2013.

[60] J. W. Evans, P. A. Berry, and K. L. Schepler, "840 mW continuous-wave Fe:ZnSe laser operating at 4140 nm," *Opt. Lett.*, vol. 37, no. 23, pp. 5021–5023, Dec 2012. [Online]. Available: http://ol.osa.org/abstract.cfm?URI=ol-37-23-5021

[61] ——, "A broadly tunable continuous-wave Fe:ZnSe laser." *Proceedings of SPIE*, vol. 8599, no. 11, 2013.

[62] G. J. Spühler, R. Paschotta, R. Fluck, B. Braun, M. Moser, G. Zhang, E. Gini, and U. Keller, "Experimentally confirmed design guidelines for passively Q-switched microchip lasers using semiconductor saturable absorbers," *J. Opt. Soc. Am. B*, vol. 16, no. 3, pp. 376–388, Mar 1999. [Online]. Available: http://josab.osa.org/abstract.cfm?URI=josab-16-3-376

[63] I. T. Sorokina, E. Sorokin, and T. Carrig, "Femtosecond Pulse Generation from a SESAM Mode-Locked Cr:ZnSe Laser," in *Conference on Lasers and Electro-Optics/Quantum Electronics and Laser Science Conference and Photonic Applications Systems Technologies*. Optical Society of America, 2006, p. CMQ2. [Online]. Available: http://www.opticsinfobase.org/abstract.cfm?URI=CLEO-2006-CMQ2

[64] M. N. Cizmeciyan, H. Cankaya, A. Kurt, and A. Sennaroglu, "Kerr-lens mode-locked femtosecond Cr^{2+}:ZnSe laser at 2420 nm," *Opt. Lett.*, vol. 34, no. 20, pp. 3056–3058, Oct 2009. [Online]. Available: http://ol.osa.org/abstract.cfm?URI=ol-34-20-3056

[65] H. Haus, J. Fujimoto, and E. Ippen, "Analytic theory of additive pulse and Kerr lens mode locking," *Quantum Electronics, IEEE Journal of*, vol. 28, no. 10, pp. 2086–2096, 1992.

[66] C. Hönninger, R. Paschotta, F. Morier-Genoud, M. Moser, and U. Keller, "Q-switching stability limits of continuous-wave passive mode locking," *J. Opt. Soc. Am. B*, vol. 16, no. 1, pp. 46–56, Jan 1999. [Online]. Available: http://josab.osa.org/abstract.cfm?URI=josab-16-1-46

[67] G. Hawkins and R. Sherwood, "Cooled infrared filters and dichroics for the James Webb Space Telescope Mid-Infrared Instrument," *Appl. Opt.*, vol. 47, no. 13, pp. C25–C34, May 2008. [Online]. Available: http://ao.osa.org/abstract.cfm?URI=ao-47-13-C25

[68] W. J. Tropf, "Temperature-dependent refractive index models for BaF_2, CaF_2, MgF_2, SrF_2, LiF, NaF, KCl, ZnS, and ZnSe," *Optical Engineering*, vol. 34, no. 5, pp. 1369–1373, 1995. [Online]. Available: http://dx.doi.org/10.1117/12.201666

[69] B. J. Frey, D. B. Leviton, and T. J. Madison, "Temperature-dependent refractive index of silicon and germanium," *Proc. SPIE*, vol. 6273, pp. 62 732J–62 732J–10, 2006. [Online]. Available: http://dx.doi.org/10.1117/12.672850

[70] J. Evans, P. Berry, and K. Schepler, "A Passively Q-switched, CW-pumped Fe:ZnSe Laser," *Quantum Electronics, IEEE Journal of*, vol. Pre-publication, 2014.

REPORT DOCUMENTATION PAGE

Form Approved
OMB No. 0704–0188

The public reporting burden for this collection of information is estimated to average 1 hour per response, including the time for reviewing instructions, searching existing data sources, gathering and maintaining the data needed, and completing and reviewing the collection of information. Send comments regarding this burden estimate or any other aspect of this collection of information, including suggestions for reducing this burden to Department of Defense, Washington Headquarters Services, Directorate for Information Operations and Reports (0704–0188), 1215 Jefferson Davis Highway, Suite 1204, Arlington, VA 22202–4302. Respondents should be aware that notwithstanding any other provision of law, no person shall be subject to any penalty for failing to comply with a collection of information if it does not display a currently valid OMB control number. PLEASE DO NOT RETURN YOUR FORM TO THE ABOVE ADDRESS.

1. REPORT DATE (DD–MM–YYYY)	2. REPORT TYPE	3. DATES COVERED (From — To)
27-03-2014	Dissertation	Sep 2010 – Mar 2014

4. TITLE AND SUBTITLE	5a. CONTRACT NUMBER
Iron-Doped Zinc Selenide: Spectroscopy and Laser Development	
	5b. GRANT NUMBER
	5c. PROGRAM ELEMENT NUMBER

6. AUTHOR(S)	5d. PROJECT NUMBER
Evans, Jonathan W.	
	5e. TASK NUMBER
	5f. WORK UNIT NUMBER

7. PERFORMING ORGANIZATION NAME(S) AND ADDRESS(ES)	8. PERFORMING ORGANIZATION REPORT NUMBER
Air Force Institute of Technology Graduate School of Engineering and Management 2950 Hobson Way WPAFB OH 45433-7765	AFIT-ENP-DS-14-M-01

9. SPONSORING / MONITORING AGENCY NAME(S) AND ADDRESS(ES)	10. SPONSOR/MONITOR'S ACRONYM(S)
Optoelectronic Technology Branch (AFRL/RYDH) Air Force Research Laboratory | AF Off of Scientific Research 2241 Avionics Circle, Bldg 62 | 875 N. Randolph St Wright-Patterson Air Force Base, OH | Arlington, VA 22203 45433 | POC: howard.schossberg@afosr.af.mil	AFRL/RYDH
	11. SPONSOR/MONITOR'S REPORT NUMBER(S)

12. DISTRIBUTION / AVAILABILITY STATEMENT

Distribution Statement A: Approved for Public Release; Distribution Unlimited

13. SUPPLEMENTARY NOTES

This material is declared of work of the U.S. Government and is not subject to copyright protection in the United States.

14. ABSTRACT

We examine the quantum mechanics of optically active ions in crystals. Insight is developed which qualitatively explains the shape of the optical absorption and emission spectra of Fe^{2+} ions in II–VI materials. In addition to a discussion of the relevant theory, this work explores experimental techniques for absorption spectroscopy, laser-induced fluorescence spectroscopy, and upper-state lifetime measurements in detail. The data collected from these experiments are interpreted in the context of the theories developed herein. The theory and data are used to develop a simple model of the temperature dependence of the upper-state lifetime of Fe^{2+} ions in ZnSe.

We report the demonstration of high-power continuous wave (CW) laser oscillation from Fe^{2+} ions in zinc selenide in detail. Broadband wavelength tuning of an Fe:ZnSe laser is demonstrated using spectrally selective intracavity optics. Additionally, several resonator configurations were briefly tested with the significant result that > 1 W power was achieved near 4100 nm.

We report the use of pulsewidth modulation techniques to deliver short, high-peak-power pulses from an Fe:ZnSe laser. The first passively Q-switched Fe:ZnSe laser was successfully demonstrated with average power > 600 mW and with pulse widths < 60 ns. Additionally, the first modelocked Fe:ZnSe laser was successfully demonstrated with average power of ~200 mW.

15. SUBJECT TERMS

Mid-IR, Laser Sources, Fe:ZnSe, Transition-Metals, Infrared Spectroscopy

16. SECURITY CLASSIFICATION OF:			17. LIMITATION OF ABSTRACT	18. NUMBER OF PAGES	19a. NAME OF RESPONSIBLE PERSON
a. REPORT	b. ABSTRACT	c. THIS PAGE	UU	113	Dr. Nancy C. Giles, AFIT/ENP
U	U	U			19b. TELEPHONE NUMBER (Include Area Code) (937) 255-3636, x4601